

Production of High-Pt Multi-Lepton Events at HERA

Diplomarbeit

am Institut für Experimentalphysik
der Universität Hamburg



vorgelegt von

Florian Rothmaier

Hamburg, Mai 2005

Zusammenfassung

Die Produktion von Lepton-Paaren in der ep-Streuung erfolgt im Standardmodell in erster Linie über Zwei-Photonen-Prozesse. Im Bereich großer invarianter Di-Lepton-Massen M_{12} werden kleine Wirkungsquerschnitte für Lepton-Paar-Erzeugung erwartet. In dieser Diplomarbeit werden Endzustände untersucht, die Elektronen und Myonen mit großen Transversalimpulsen enthalten. Die Daten wurden in den Jahren 1994-2000 und 2003-2004 am H1 Detektor genommen und entsprechen einer integrierten Luminosität von 172 pb^{-1} .

Die P_T - und Massenspektren werden den Vorhersagen des Standardmodells gegenübergestellt. Mit acht Ereignissen im Bereich großer invarianter Massen $M_{12} > 100 \text{ GeV}$ wird die Vorhersage dort leicht übertroffen. Eine signifikante Abweichung wird jedoch nicht gefunden.

In der Arbeit werden zudem Methoden vorgestellt, mit denen sich die Massenauflösung verbessern lässt.

Abstract

Lepton pair production in ep scattering in the Standard Model is mainly provided by the two-photon process. Small cross-sections are predicted at high invariant di-lepton masses M_{12} . Multi-lepton production is studied in this diploma thesis searching for topologies with electrons and muons in the final state. Data were taken at the H1 detector during 1994-2000 and 2003-2004 and correspond to an integrated luminosity of 172 pb^{-1} .

The P_T and mass spectra are compared to the Standard Model predictions. Eight events with invariant masses $M_{12} > 100 \text{ GeV}$ correspond to a slight excess of data compared to the theoretical prediction. However, no significant deviation is found in the analysis.

Additionally, the diploma thesis presents methods allowing an improvement of mass resolution.

Contents

Introduction	6
1 Lepton Pair Production	8
1.1 Overview	8
1.2 Electroweak Lepton Pair Production	8
1.2.1 Two-Photon Process	9
1.2.2 Cabibbo-Parisi and Drell-Yan Process	11
1.2.3 Z^0 -Production	14
1.2.4 Comparison Between the Electroweak Processes	14
1.2.5 Monte Carlo Samples	16
1.3 Vector Meson Resonances	18
1.4 Background Processes	20
1.4.1 Misidentification of Electrons	20
1.4.2 Misidentification of Muons	21
1.4.3 Simulation of the Background	21
1.5 Goals of the Analysis	22
1.5.1 Multi-Electron Analysis of HERA-I Data	22
1.6 Lepton Production Beyond the Standard Model	24
1.6.1 Supersymmetry and Doubly Charged Higgs	24
2 Experimental Setup	27
2.1 The HERA Collider	27
2.2 The H1 Detector	28
2.2.1 Tracking System	30
2.2.2 Calorimeters	31
2.2.3 Muon System	32
2.2.4 Triggers	33
3 Particle Identification	36
3.1 Track Selection	36
3.2 Electron Identification	37

3.2.1	Electron Finder	37
3.2.2	Additional Criteria	38
3.2.3	Electron Identification Efficiencies	40
3.3	Muon Identification	43
3.3.1	Muon Finder	43
3.3.2	Additional Criteria	46
3.3.3	Triggers for the Muon Selection	48
3.3.4	Muon Identification Efficiencies	51
3.4	Systematic Errors	52
3.4.1	Experimental Uncertainties	52
3.4.2	Theoretical Uncertainties	53
4	Multi-Lepton Analysis	54
4.1	Lepton Selection Criteria	54
4.1.1	Phase-space for Electrons and Muons	54
4.1.2	Anti-cosmics Rejection	56
4.1.3	P_T Correction by the “ P_T -Balance Method”	58
4.2	Results of the Analysis	60
4.3	Sub-Classes of Di-Lepton Channels HERA-I and -II	62
4.3.1	e - e Channel	63
4.3.2	e - μ Channel	65
4.3.3	μ - μ Channel	66
4.4	Sub-Classes of Tri-Lepton Channels HERA-I and -II	68
4.4.1	e - e - e Channel	68
4.4.2	e - μ - μ Channel	71
4.4.3	Radiative Events	72
4.5	Events in the High Mass Range	74
5	Kinematical Fit for High Mass Events	76
5.1	Motivation	76
5.2	Description of the Fit Programme APLCON	79
5.2.1	Quality of the Kinematical Fit	82
5.3	Choice of Parameters	83
5.3.1	Fitting Electrons	83
5.3.2	Fitting Muons	84
5.4	Tests of the Fit Method for Muons	88
5.4.1	MC Event Sample	89
5.4.2	Conclusion	101
5.5	Fit Results	101
5.5.1	Run 367354, Event 22364	101
5.5.2	Run 383168, Event 78379	104

5.5.3 Summary	108
6 Conclusion and Outlook	109
Bibliography	111
Appendix	115
Danksagung – Remerciements	120

Introduction

The Standard Model (SM) is a very successful theory which describes almost all experiments in modern particle physics with high accuracy. This theory is based on the concept of local gauge symmetry, consisting of a $SU(2)_L \otimes U(1)_Y$ symmetry for electroweak interactions and a $SU(3)_C$ symmetry for strong interactions.

In spite of the good agreement with the experiments, there are many indications that the SM will not be the final theory of particle physics. The Standard Model contains at least 19 arbitrary parameters, among them three gauge couplings, parameters associated with the nine charged fermion masses and the four mixing angles in the CKM matrix. These values are chosen to fit the data. Consequently, the SM is not able to explain the origin of particle masses, or to improve our understanding of the hierarchy of quark mixing angles. Many other questions like the origin of CP violation or the asymmetry between matter and antimatter still remain unanswered.

For this reason, many different theories beyond the Standard Model (BSM) have been developed in the recent years by theoretical physicists. One possible approach to the BSM are the supersymmetric (SUSY) models which introduce a symmetry between bosons and fermions associating partners with spin 1 to fermions. This method unifies the electroweak and the strong interaction describing particles and their interactions in one gauge group. In the high energy range there is only one coupling constant characterising the unified interaction, whereas in lower regions broken symmetry leads to the behaviour predicted by the SM.

Some supersymmetric models already expect BSM-phenomena in regions accessible for current particle colliders like HERA with a center of mass energy of $\sqrt{s} = 320$ GeV. Despite the big effort in looking for new event topologies and resonances in mass spectra, no SUSY-Particle has been identified so far.

Physics beyond the Standard Model is also subject of this diploma thesis, and for experimentalists there are two different starting points to approach this aspect of particle physics, the model-dependent and the “generic”, model-

independent search.

The model-dependent search is based on a theory beyond the Standard Model. It is looked for signals that correspond to a process suggested by a BSM-model e.g. a SUSY model. If the SM can also contribute to the signature, its expectation has to be subtracted from the total expectation (SM+BSM) for the process. If no indications for new physics are found, the method makes it possible to deduce limits on the process parameters, for instance on particle masses.

In contrast to the first method, the idea of the model-independent search is to define a common phase-space for several types of particles – e.g. electrons, muons, jets or neutrinos – identified in the final state. The events are assigned to classes by their particle content. This method performs a test of the Standard Model.

Kinematical quantities like the invariant mass or the transverse momentum are defined. Regions where the SM-predictions are small are of particular interest because of their sensitivity to new physics. The data content of a class is compared to the SM-expectation. Possible deviations between experiment and theory highlight in which regions a more detailed search for new physics could be worthwhile.

In the analysis presented here we have chosen the second approach focussing on electron and muon topologies. The combination of HERA-I (118 pb^{-1}) and HERA-II Data (54 pb^{-1}) has been utilised.

In the first chapter, the theoretical background to the subject is presented. We will discuss the main sources leading to lepton-production, principally in QED. In addition, an example for a BSM-process is given including some results of the work by our group on this topic. In Chapter 1.5, we will provide an overview of the previous analysis which has been done by the H1-Marseille group, which gave the motivation for the multi-lepton analysis presented here. The next chapter describes the HERA accelerator and the H1-Detector. Then we will focus on multi-lepton analysis, explaining selection criteria for the particles and the methods of background rejection. Next, in Chapter 4 the results of the multi-lepton analysis are presented. The high-mass events raise further questions leading to a more detailed check. This is presented in the fifth chapter.

Chapter 1

Lepton Pair Production

1.1 Overview

In this chapter we will describe the processes contributing to lepton pair production which can either be elastic ($ep \rightarrow epl^+l^-$) or inelastic ($ep \rightarrow eXl^+l^-$). X defines the hadronic final state and l^+l^- corresponds to an electron-, muon-, (or tau-)pair. Our considerations will mainly be concentrated on the validity range of the Standard Model. We will discuss by which effects the analysis is dominated, and which background processes can be taken for a lepton pair signal. A description of the MC generators used to compare data to the theory is also provided.

1.2 Electroweak Lepton Pair Production

Lepton pair production in the Standard Model occurs either by the electroweak production processes or by the decay of the vector meson resonances J/ψ and Υ . In the electroweak sector, the main sources are processes mediated by two uncharged gauge bosons, in particular the photon-photon collisions $\gamma\gamma \rightarrow l^+l^-$. Furthermore, lepton pairs can be produced by the conversion of a Bremsstrahlung-photon or by the decay of a Z^0 .

A certain amount of lepton pairs found in the region around the J/ψ - and the Υ -mass stems from the decay of these resonances. Due to its mass, the decay of the J/ψ can only lead to electron or muon pairs whereas the disintegration of the Υ gives rise to e - μ - or τ -pairs. The processes are summarised in table 1.1.

Electroweak Muon Pair Production:			
Two-boson		ep	\longrightarrow ep l^+l^-
	via	$\gamma\gamma$	\longrightarrow l^+l^- ,
		γZ^0	\longrightarrow l^+l^-
	or	$Z^0 Z^0$	\longrightarrow l^+l^-
Bremsstrahlung	ep	\longrightarrow ep γ	\longrightarrow ep l^+l^-
Z^0 -production	ep	\longrightarrow ep Z^0	\longrightarrow ep l^+l^-
Decay of Vector Meson Resonances:			
J/ψ decay		J/ψ	\longrightarrow l^+l^-
Υ decay		Υ	\longrightarrow l^+l^-

Table 1.1: Lepton pair production in the Standard Model

1.2.1 Two-Photon Process

This section concerns the so-called ‘‘Two-Photon-’’ or ‘‘Bethe-Heitler Process’’ which is the main source of lepton pair production in the analysis. In its Feynman diagram, presented in figure 1.1, it is shown that one photon coming from the proton or quark side interacts with another photon emitted by the electron. Resulting from the $\gamma\gamma$ -interaction a lepton pair – $e-e$, $\mu-\mu$ or $\tau-\tau$ – is produced. This process is referred to as ‘‘elastic’’ if the proton does not decay, and denoted as ‘‘inelastic’’ if the photon is emitted by one of the proton constituents.

The cross-section can then be calculated by the formula

$$\left[\frac{d\sigma}{dP_T}(s, P_T) \right]_{ep \rightarrow eXl^+l^-} = \int_{x_{min}}^1 dx \int_{x_{min}^*}^1 dx^* f_{\gamma/p}(x) f_{\gamma/e}(x^*) \left[\frac{d\sigma}{dP_T}(\hat{s}, P_T) \right]_{\gamma\gamma \rightarrow l^+l^-} \quad (1.1)$$

according to [Art91].

The calculation is based on the idea of reducing the $2 \rightarrow 4$ reaction to the simpler $2 \rightarrow 2$ process. This technique has been applied for the first time by Weizsäcker and Williams and has become a common method to handle multi-particle reactions. Consequently it can be noted that equation (1.1) consists of three parts, the photon flux from the proton side $f_{\gamma/p}(x)$, the photon flux from the electron side $f_{\gamma/e}(x^*)$ and the cross-section of the sub-process $\gamma\gamma \rightarrow l^+l^-$.

P_T in (1.1) indicates the transverse momentum of the lepton-pair. The vari-

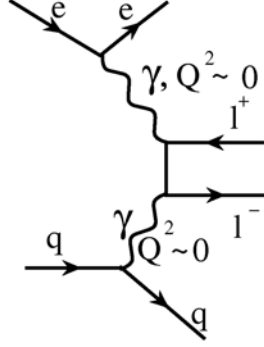


Figure 1.1: Bethe-Heitler or two-photon process: main source of lepton pair production in the Standard Model

able x^* denotes the relative energy loss of the electron which is equivalent to the photon energy: $E_\gamma = z_e \cdot E$.

The quantity x is the counterpart on the proton side. s indicates the overall center of mass energy squared while \hat{s} is the invariant mass squared of the lepton pair. The lower limits of the integral are given by $x_{min}^* = 4P_T^2/(xs)$ and $x_{min} = 4P_T^2/s$. These variables are correlated by

$$\hat{s} = xx^*s \quad (1.2)$$

While the $e\text{-}\gamma$ -flux is represented by

$$f_{\gamma/e}(x^*) = \frac{\alpha}{\pi x^*} \left[(1 - x^* - \frac{x^{*2}}{2} \ln \frac{P_T^2}{m_e^2 x^{*2}} - (1 - x^*)) \right] \quad (1.3)$$

the calculation of the $p\text{-}\gamma$ term is more complicated due to the complex structure of the proton. In this case the flux has to be evaluated as the sum of an elastic and an inelastic contribution:

$$f_{\gamma/p}(x) = f_{\gamma/p}^{el}(x) + f_{\gamma/p}^{inel}(x) \quad (1.4)$$

The elastic term makes use of the electric and magnetic form factors G_E and G_M

$$f_{\gamma/p}^{el}(x) = \frac{\alpha}{\pi x} \int_{Q_{min}^2}^{Q_{max}^2} \frac{dQ^2}{Q^2} \left((1 - x) \left(\frac{G_E^2}{Q^2} + \frac{G_M^2}{M_p^2} \right) (Q^2 - Q_{min}^2) + \frac{x}{2} G_M^2 \right) \quad (1.5)$$

The lower and upper limits of the integral are $Q_{min}^2 = M_p^2 x^2 / (1 - x)$ and $Q_{max}^2 \simeq P_T^2 / (1 - x)$.

The inelastic part is given by the convolution of the photon flux from a quark $f_{\gamma/q}^{QPM}$ provided by the quark-parton model (lowest order QCD) with the probability to find a quark in the proton, being $F_2^p(u) \frac{e_q^{-2}}{u^2}$:

$$f_{\gamma/p}^{inel}(x) = \int_x^1 F_2^p(u) \frac{du}{u^2} e_q^{-2} f_{\gamma/q}^{QPM} \left(\frac{x}{u} \right) \quad (1.6)$$

The explicit calculation of this expression can be seen in [Art91].

Finally, the cross section of the sub-process is given by:

$$\left[\frac{d\sigma}{dP_T}(\hat{s}, P_T) \right]_{\gamma\gamma \rightarrow l+l^-} = \frac{8\pi\alpha^2}{P_T \hat{s}} \frac{1 - 2\frac{P_T^2}{\hat{s}}}{\sqrt{1 - 4\frac{P_T^2}{\hat{s}}}} \quad (1.7)$$

The total cross-section of the Bethe-Heitler process decreases fast with the transverse momentum, $\sigma \propto P_T^{-8}$. In the P_T region above 20 GeV the total cross-section is roughly 0.09 pb.

1.2.2 Cabibbo-Parisi and Drell-Yan Process

The second group of electroweak particle interactions mentioned above is formed by the Bremsstrahlungs processes, which are displayed in figure 1.2. They are characterised by an electron-proton or electron-quark-interaction via γ - or Z^0 -exchange. The particle reactions in b) and c) are known as ‘‘Cabibbo-Parisi’’ and ‘‘Drell-Yan process’’, respectively. In the diagrams a) through d) it can be seen that either the proton (quark) or the electron radiates a photon (Z^0) that will disintegrate into a lepton pair. The photon can be emitted before or after the ep -interaction.

The differential cross-sections of the Cabibbo-Parisi and the Drell-Yan effect increase slightly at higher transverse momenta. However the contributions of both processes are small in the kinematic region covered by the analysis.

In contrast to the other electroweak pair production processes, the Cabibbo-Parisi effect produces much more electron pairs than muon pairs. This can easily be understood when the cross section is written as a function of the Mandelstam variables s , t , and u . The contribution of the sub-process $e^- e^+ \rightarrow \mu^- \mu^+$ in the muon case is given by

$$\frac{d\sigma}{dt} = \frac{2\pi\alpha^2}{\hat{s}^2} \left(\frac{t^2 + u^2}{\hat{s}^2} \right). \quad (1.8)$$

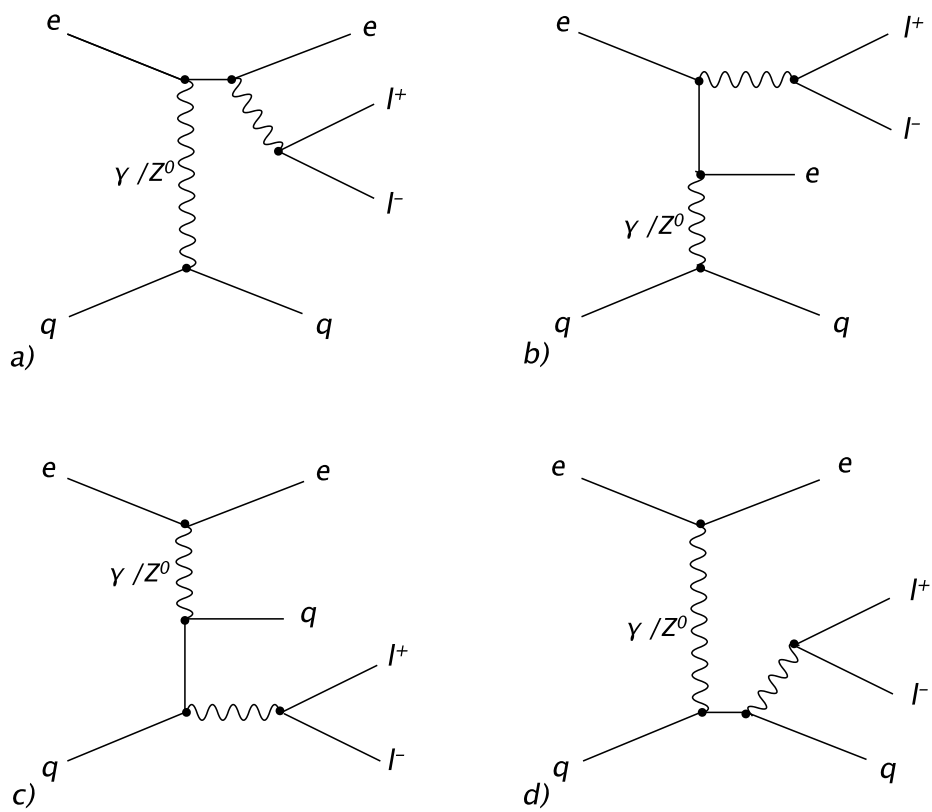


Figure 1.2: Bremsstrahlungs processes: Cabibbo-Parisi b) and Drell-Yan effect c). In a) and b) the photon is radiated from the electron side, in c) and d) from the proton side

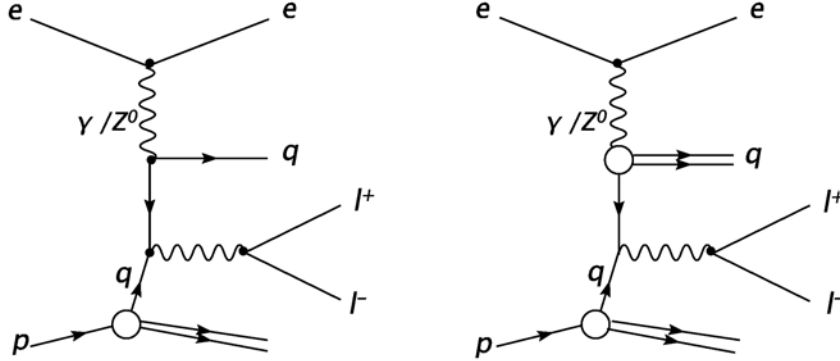


Figure 1.3: Drell-Yan effect: point-like (left) and resolved type (right)

Electron pairs are produced in Bhabha scattering ($e^-e^+ \rightarrow e^-e^+$):

$$\frac{d\sigma}{dt} = \frac{2\pi\alpha^2}{\hat{s}^2} \left(\frac{t^2 + u^2}{\hat{s}^2} + \frac{\hat{s}^2 + u^2}{t^2} + \frac{2u^2}{t\hat{s}} \right). \quad (1.9)$$

While only the s -channel contributes in the case of muon pair production, the cross section for Bhabha scattering is clearly increased by the additional term in (1.9) due to a contribution from the t -channel.

In the case of the Drell-Yan process, where the Bremsstrahlung is radiated from the quark side, the cross section can be evaluated by calculating the sub-process $q\bar{q} \rightarrow l^-l^+$:

$$\left[\frac{d\sigma}{dt dx} \right]_{ep \rightarrow eXl^+l^-} = f_{q/e} \left[\frac{d\sigma}{dt} \right]_{q\bar{q} \rightarrow l^+l^-}. \quad (1.10)$$

$f_{q/e}$ is the convolution of the photon flux, $f_{\gamma/e}$, with the probability that the photon disintegrates into a quark pair $f_{q/\gamma}$ [Art91]. It is easy to distinguish between the point-like and the resolved processes shown in figure 1.3. In the first case the process is described as an interaction between point-like particles (γ - q -coupling) whereas the second case occurs in the regime of photoproduction ($Q_e^2 \rightarrow 0$). This is where photons have to be interpreted as particles with a partonic structure represented by the ‘blob’ in the picture on the right. In the Vector Meson Dominance Model [Sak69] this structure is described mathematically by superimposing the bare photon $|\gamma_B\rangle$ and hadronic components $|h\rangle$:

$$|\gamma\rangle = \sqrt{1-c^2}|\gamma_B\rangle + c|h\rangle \quad (1.11)$$

where c is a normalisation factor. Having the same quantum number as the photon, the state $|h\rangle$ could be a vector meson for example. Events with a virtuality Q^2 smaller than 25 GeV^2 are typically of the resolved type.

The cross section of the Drell-Yan process is very small compared to the two-photon process because the Drell-Yan lepton pairs are boosted in the proton direction. Therefore, noteworthy contributions are only provided at very small polar angles θ , which are excluded in our analysis.

1.2.3 Z^0 -Production

Bremsstrahlung processes can also take place with Z^0 -bosons. The Feynman diagrams have already been shown in figure 1.2. Instead of a photon a Z^0 boson is radiated from the electron or the proton (quark) side. Because of the large Z^0 -mass ($M_{Z^0} = 91.19 \text{ GeV}$), the cross-section of these processes is very small.

1.2.4 Comparison Between the Electroweak Processes

In figure 1.4, the cross sections of the different electroweak processes are presented. Keeping in mind that $d\sigma/dP_T$ decreases quickly with the transverse momentum, the y-axis is multiplied by a factor of P_T^3 . For the two-photon process, the elastic case ($\gamma\gamma_{el}$), the inelastic case ($\gamma\gamma_{ine}$), and the sum of them ($\gamma\gamma_{tot}$) are displayed. The Cabibbo-Parisi effect is shown for electron- (CP_{ee}) and muon pair production ($CP_{\mu\mu}$), the Drell-Yan process is presented for the point-like (DY_{PNT}) and the resolved type (DY_{VMD}).

Generally it can be noted that in the P_T -range presented here, lepton pair production is dominated by the $\gamma\gamma$ -process. The contributions of the Cabibbo-Parisi effect are larger than the contributions due to the Drell-Yan process.

Cross-sections of the elastic and inelastic Bethe-Heitler process are of the same order. At higher transverse momenta their magnitudes become comparable to the CP-process. The increase of CP-cross-section can be explained by the Z^0 -resonance. As mentioned above, the contributions of the Cabibbo-Parisi effect for electrons are much larger than for the muons due to an additional diagram (t-channel). While the muon fraction is in the order of the Drell-Yan effect at small transverse momenta, it approaches the electron fraction in higher P_T regions.

The Drell-Yan effect is dominated by the point-like type. However, compared to the $\gamma\gamma$ -process the Drell-Yan contribution is about two orders of magnitude smaller at low P_T and about one order of magnitude larger at higher momenta.

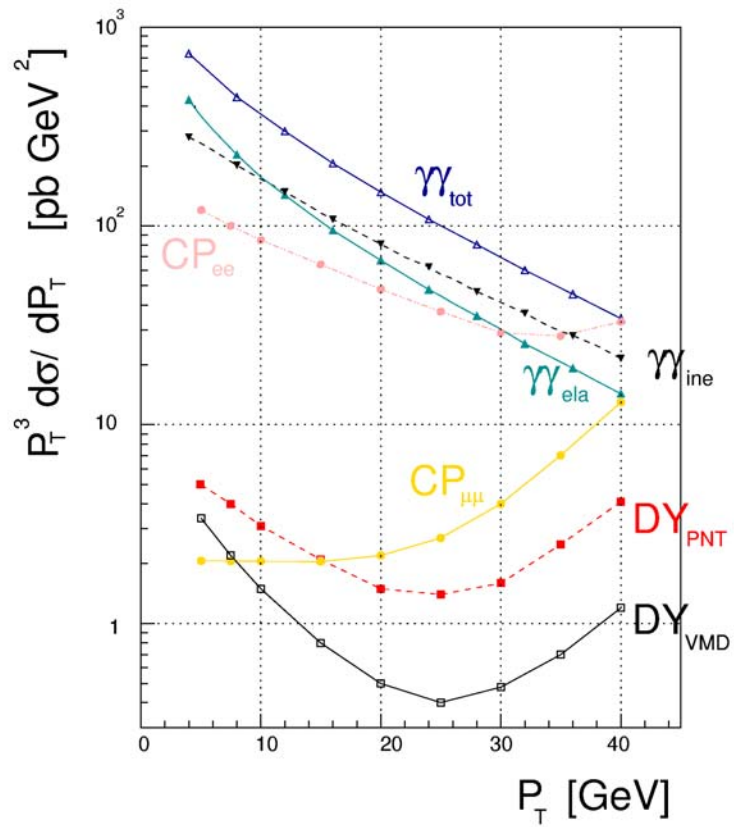


Figure 1.4: Electroweak lepton pair production: comparison between the different process types, the two photon ($\gamma\gamma$), the Cabibbo=Parisi (CP), and the Drell-Yan process (DY)

1.2.5 Monte Carlo Samples

In order to compare the experimental data to the theoretical predictions, Monte Carlo programmes have been developed. These programmes contain the matrix elements of the required processes as well as information about the detector and the triggers. A Monte Carlo simulation consists of three steps:

- Generation of the incident particles
- Simulation of the detector and trigger response
- Reconstruction of particles according to the detector signals

In the first step, partonic densities of the proton are taken into account in order to determine the initial state and to calculate the matrix elements. The computation is improved by considering radiative effects in the initial and final states. In the second section, the resulting stable particles are introduced in a simulation of the H1-detector. The simulation, based on the programme GEANT [Bru94], contains the detector geometry as well as the characteristics of the materials used in the different parts of the detector. For the best possible comparison between the experimental situation and the theoretical prediction, it is important to take special features like dead areas in the detector into consideration.

In the third step, the reconstruction of simulated events is performed in the same way as for real physical events.

In our case we generate particles with the programme GRAPE [Abe01], which demonstrates an improvement on the older generator programme LPAIR [Bar91]. In contrast to the latter, GRAPE simulates not only the two-photon process but also the di-lepton production via γZ^0 , $Z^0 Z^0$ collisions and Bremsstrahlung processes. Exceptions are the Bremsstrahlung from the proton and the resolved Drell-Yan effect which may be generated by the programme PYTHIA [Sjo01]. At this level GRAPE contains a cut which excludes values of the virtuality less than $Q^2 = 25 \text{ GeV}$.

The cross section calculation uses the exact matrix elements in electroweak theory at tree level i.e. at lowest order (diagrams without loops). Furthermore the influence of radiative effects in the initial and final state and of interference effects in the final state e^+e^- are taken into account. The programme also allows to choose a sub-set of diagrams e.g. the sub-process $\gamma\gamma \longrightarrow l^+l^-$ in the case of the Bethe-Heitler effect.

To simulate the process $ep \longrightarrow el^+l^-X$ and to treat correctly the proton

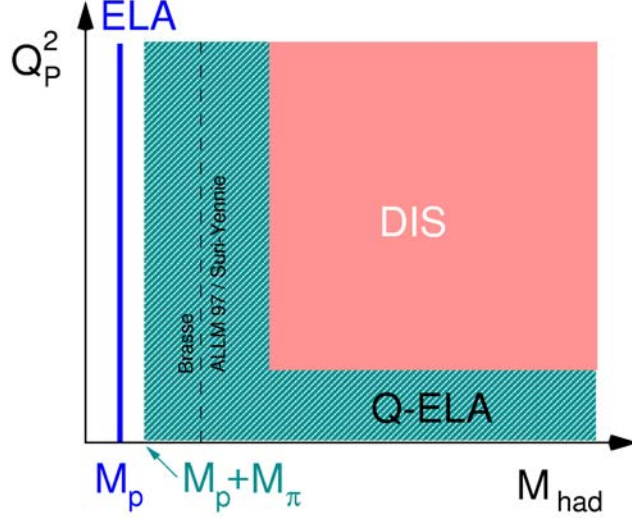


Figure 1.5: Division of phase-space: the quantities Q_p^2 and M_{had}^2 are used to classify the regions of elastic (ELA), quasi-elastic (Q-ELA), and deep inelastic (DIS) scattering. Q_p^2 is displayed as function of M_{had}^2 . The dotted line in the quasi-elastic sector corresponds to the border between two different parametrisations of the structure function (Brasse et al., ALLM 97).

structure, GRAPE has to distinguish between different physical situations. The following two variables are used to classify three categories, the elastic, the quasi-elastic and the deep-inelastic sectors:

$$Q_p^2 := -[p_{e_{ini}} - (p_{e_{fin}} + P_{l^-} + P_{l^+})]^2 \quad (1.12)$$

$$M_{had}^2 := [(p_{e_{ini}} + p_{p_{ini}}) - (p_{e_{fin}} + P_{l^-} + P_{l^+})]^2 \quad (1.13)$$

Q_p^2 is the negative momentum squared of the photon emitted by the proton and M_{had}^2 the invariant mass of the hadronic system.

The division of the phase-space is shown in figure 1.5 where Q_p^2 is plotted against M_{had}^2 . The threshold separating the elastic and the quasi-elastic regions can be defined at $M_{had}^2 = M_p + M_\pi$, while the lower limits for the deep-inelastic sector are given by $M_{cut} = 5$ GeV and $Q_{min} = 1$ GeV, respectively. The proton structure is described by the electric and magnetic form factors, $G_E^p(Q_p^2)$ and $G_M^p(Q_p^2)$ in the elastic case and by the electromagnetic structure functions $W_1(Q_p^2, M_{had}^2)$ and $W_2(Q_p^2, M_{had}^2)$ in the quasi-elastic case.

For deep-inelastic scattering, the Quark Parton Model is used to calculate the diagrams.

1.3 Vector Meson Resonances

A completely different way to produce lepton pairs at HERA is the decay of the vector meson resonances J/ψ and Υ . Both $|J/\psi\rangle = |c\bar{c}\rangle$ and $|\Upsilon\rangle = |b\bar{b}\rangle$ constitute bounded states (ground state and excitations) which are treated in analogy to the hydrogenium atom. In the case of the J/ψ the system is called charmonium, in the case of the Υ it is named bottomonium. The masses of the ground states are $M_{J/\psi(1S)} = 3096.916 \pm 0.011$ MeV, and $M_{\Upsilon(1S)} = 9460.30 \pm 0.026$ MeV [PDG04]. As the Υ decay can produce more energetic lepton pairs than the J/ψ decay, we will only give a brief overview of the former.

There are two different production mechanisms, an elastic case described by the so-called Vector Meson Dominance Model (VMD) and an inelastic case provided in photon-gluon or gluon-gluon reactions [Schm02].

In the VMD a photon from the electron side fluctuates in a vector meson that interacts subsequently with the proton. To describe the process correctly, a colourless object referred to as ‘‘pomeron’’ has to be introduced.

In the inelastic situation the vector meson can be generated by direct photon-gluon fusion, or so-called ‘‘resolved photon process’’ where two gluons are produced via a quark loop. The diagrams of the described mechanisms can be seen in figure 1.6.

Branching ratios for lepton pair production by the decay of the ground state $\Upsilon(1S)$ can be taken from [PDG04]:

$$\begin{aligned} \Upsilon(1S) &\longrightarrow \tau^+\tau^- & : & (2.67 \pm_{0.16}^{0.14}) \% \\ \Upsilon(1S) &\longrightarrow \mu^+\mu^- & : & (2.48 \pm 0.06) \% \\ \Upsilon(1S) &\longrightarrow e^+e^- & : & (2.38 \pm 0.11) \% \end{aligned}$$

Although Υ -production with a subsequent decay in lepton pairs can be simulated by Monte Carlo generators - DIFFVM [Lis98] for the elastic and EPJPSI [Jun92] for the inelastic case - we do not make use of them. The only significant contributions of the Upsilon-decay occur around the value of its mass $M_{\Upsilon(1S)} = 9.46$ GeV resulting in a single narrow peak. Since we are interested in high- P_T events a minimal transverse momentum is required ($P_T > 10$ GeV for Lepton 1 and $P_T > 5$ GeV for Lepton 2, respectively). The contribution of the Υ -decay is strongly affected by the chosen cuts, making it possible to neglect the process. This has been shown in the di-muon analysis [Lei02].

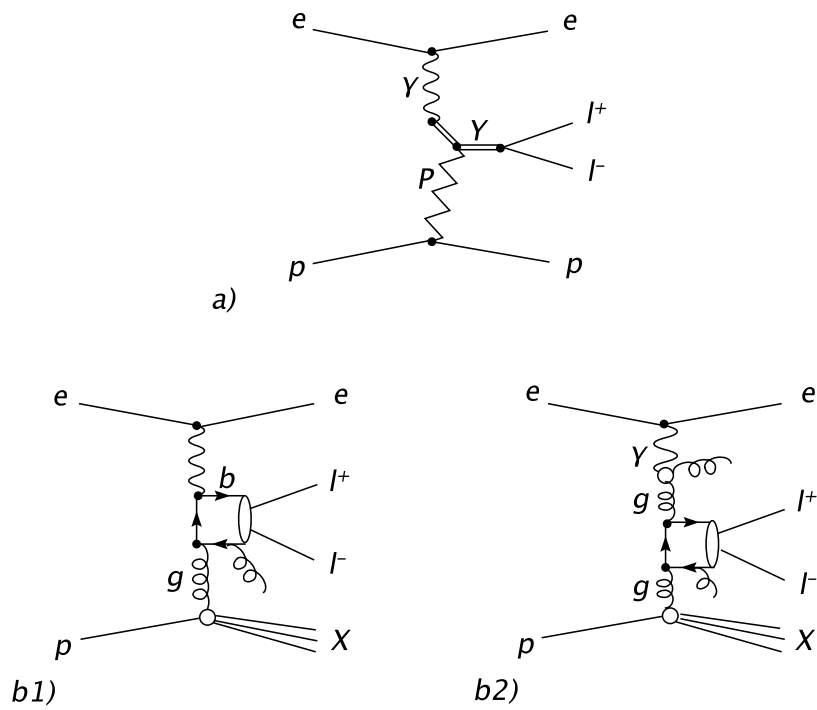


Figure 1.6: Lepton Pair production via Υ decay: in this picture the different production mechanisms are presented. a) shows the elastic process in the VMD (“pomeron”-) model and in b) the inelastic process via photon-gluon fusion b1) and gluon-gluon fusion b2) is illustrated.

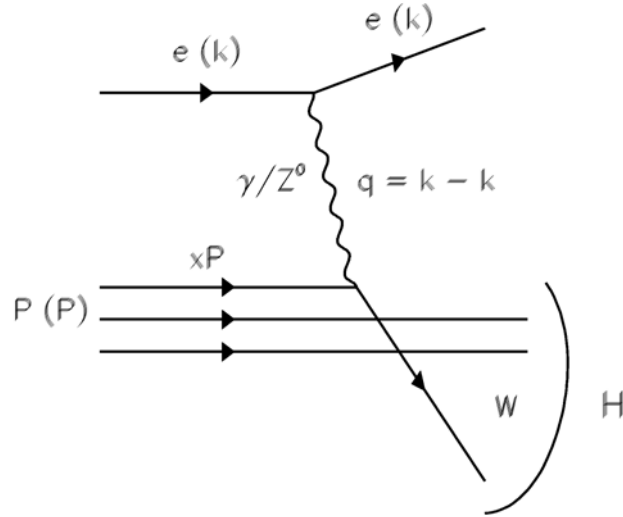


Figure 1.7: NC-DIS: electron-quark scattering mediated by neutral currents

1.4 Background Processes

All multi-lepton channels can more or less be masked by the background, making it difficult to correctly compare the results of the analysis to the theoretical prediction. As well as the signal – lepton pair production simulated by GRAPE – we have to simulate contributions from the background. This stems either from the ep -interaction (physics background) or from particles not produced by ep collisions (non-physics background), e.g. cosmic muons. Here we will restrict the description to the former type and in Chapter 4 we will explain how to get rid of the contributions due to cosmics.

The Physics background consists of events which are supposed to match one analysis class due to the misidentification of at least one of the particles. In our multi-lepton-analysis, particles identified as electrons or muons can be fakes. We have to think about the true identity of these particles and the underlying processes in which they have been produced.

1.4.1 Misidentification of Electrons

Unlike electrons, photons do not have a track in the detector because they have no charge. Unfortunately, their energy deposits in the electromagnetic

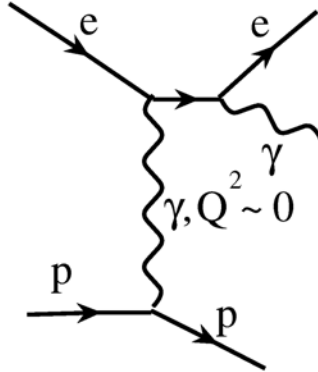


Figure 1.8: QED Compton effect: an emitted photon can be detected by mistake by an electron

calorimeter cannot be distinguished from the electron clusters. Therefore, they can be misidentified as electrons, especially if there are tracks of other particles in the detector. Thus we have to taken into account two processes, the deep inelastic scattering mediated by neutral currents (NC-DIS) and elastic or inelastic QED Compton processes. The NC-DIS is presented in figure 1.7. Photons can be radiated from the electron or the quark side. QED Compton is shown in figure 1.8. Photons can be radiated from the electron. The background due to radiated photons can be suppressed by requiring that the electromagnetic cluster has an associated track in the calorimeter.

1.4.2 Misidentification of Muons

Hadrons, especially kaons or pions, can be misinterpreted as a muon signal. These particles can sometimes be part of a jet stemming from the NC-DIS process. It is also possible to detect muons which are decay products of a particle in the jet. This type of background is reduced by implementing an isolation criteria between muons and jets.

1.4.3 Simulation of the Background

Following the discussion above, we have to simulate the NC-DIS and the QED Compton processes in order to estimate the size of the background. For the first process we use DJANGO [Schu91] or RAPGAP [Jun95] generators, which take also into account the contributions from the inelastic QED

Compton process. The simulation of the elastic QED Compton process is provided by the generator WABGEN [Ber98].

1.5 Goals of the Analysis

1.5.1 Multi-Electron Analysis of HERA-I Data

The subject of this diploma thesis has been motivated by a Multi-Electron analysis performed at H1 with HERA-I data in order to test the Standard Model [H103a]. In the data sample corresponding to an integrated luminosity of 115.2 pb^{-1} di- and tri-electron events have been investigated.

The selection cuts can be divided into two groups, the preselection and the final selection.

First of all the phase-space is defined by restrictions on the energy and the polar angle:

- **Energy:** $E^{ele} > 5 \text{ GeV}$
- **Polar Angle:** $5^\circ < \theta_{l1,2} < 175^\circ$

In the forward region between $\theta = 5^\circ$ and 20° the energy is required to be greater than $E_{ele} > 10 \text{ GeV}$. Further details can be found in [H103a].

The final selection is built up by the two- and the three-electron channel. An event which can enter the final selection has to contain two central particles $20^\circ < \theta < 150^\circ$ carrying a minimal transverse momentum:

- **Transverse Momentum:** $P_{T_{ele1}} > 10 \text{ GeV} \quad P_{T_{ele2}} > 5 \text{ GeV}$

For the third electron in the $e-e-e$ channel the bounds on the energy are $E_{ele} > 5 \text{ GeV}$ in the central and backward region ($20^\circ < \theta < 175^\circ$) and $E_{ele} > 10 \text{ GeV}$ in the forward region.

For the di- and tri-electron selection the number of observed events was in good agreement with the theoretical prediction. This can be seen in table 1.2 which also shows that both channels are dominated by the signal. The invariant mass distributions are presented in figure 1.9.

In the mass region $M_{12} > 100 \text{ GeV}$ where the SM prediction is small, six outstanding events have been detected in the data sample. Three have been found in the $e-e$ channel while the Monte Carlo predicts 0.30 ± 0.04 , and the other three events were found in $e-e-e$ compared to the expected value of 0.23 ± 0.04 .

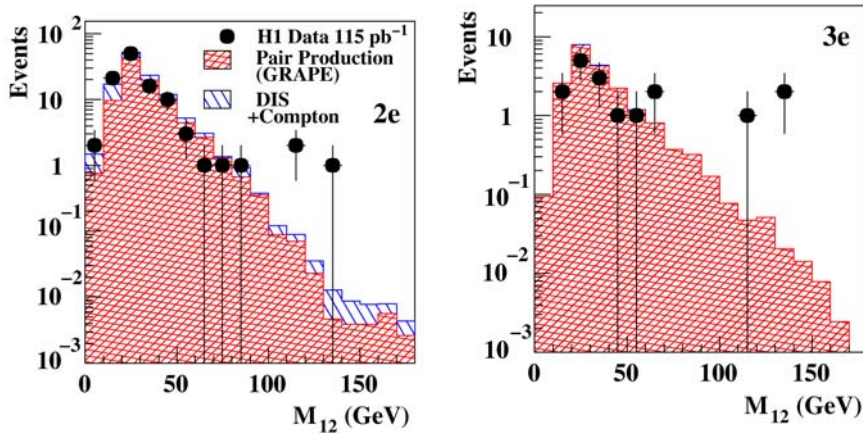


Figure 1.9: Invariant mass distributions in the multi-electron analysis on the HERA-I data for the di- (left) and the tri-electron channel (right) [H103a].

Selection	Data	SM	Pair Production (GRAPE)	DIS + Compton
ee	108	117.1 ± 8.6	91.4 ± 6.9	25.7 ± 5.2
eee	17	20.3 ± 2.1	20.2 ± 2.1	0.1 ± 01

Table 1.2: Comparison between Data and SM prediction for the two- and three-electron channel from [H103a].

In [H104b], the di-muon channel was studied in detail, using an integrated luminosity value of 70 pb^{-1} . In contrast to the six high-mass events found in the former analysis, no events at masses $M_{12} > 100 \text{ GeV}$ were detected. The results of the search for multi-electron events motivate us to connect and to extend the two previous analyses. In order to realise this, the same integrated luminosity is used for both the electron- and the muon channels. We define general selection criteria which are supposed to be valid for either kind of particle. Our analysis is enlarged beyond the “pure” e - and μ -classes so as to include the mixed channels e - μ and e - μ - μ . With respect to these criteria we may speak of a search for “multi-lepton events”. The analysis is also extended to the HERA-II data.

1.6 Lepton Production Beyond the Standard Model

1.6.1 Supersymmetry and Doubly Charged Higgs

Physics beyond the Standard Model is a field containing a huge number of models that pursue similar goals. A promisingly large part of BSM-physics is covered by the supersymmetric (SUSY) models. In contrast to the Standard Model, SUSY theories can show that the running coupling constants of the strong, the weak, and the electromagnetic interactions converge to one point in the range of order of 10^{15} GeV. This highlights the unification of the three interactions at large energies. Furthermore, some of the mathematical problems raised by the SM can be solved. The supersymmetric left-right models (SUSYLR) were created to find an explanation for the parity-violation observed in low-energy weak interactions. Implementing the see-saw mechanism [Gel79] which attests that there is a light and a heavy neutrino in every lepton family, the model also explains the small observed neutrino masses. The Standard Model is part of the theory within the limits of low energies.

The left-right symmetric model of R.N. Mohapatra and G. Senjanovic [Moh80a] is based on the gauge group $SU(2)_L \otimes SU(2)_R \otimes U(1)_{B-L}$. It yields left or right handed triplets of Higgs bosons [Moh80b], $H_{R,L} = (H_{R,L}^0, H_{R,L}^\pm, H_{R,L}^{\pm\pm})$ providing neutral, as well as simply and doubly charged Higgs particles. In connection with lepton pair production, the doubly charged Higgs $H^{\pm\pm}$ is a matter of particular interest. Generally its coupling to lepton pairs can be described by the Lagrangian

$$\mathcal{L} = h_{ij}^{L,R} H^{\pm\pm} \bar{l}_i^c P_{L,R} l_j \quad (1.14)$$

with the generation indices $i, j = e, \mu, \tau$, the Yukawa couplings $h_{ij}^{L,R}$, and the lepton fields $P_{L,R} = (1 \pm \gamma^5)/2$ and l . A decay of the $H^{\pm\pm}$ to lepton pairs and mixed combinations like $e\text{-}\mu$ is possible.

In figure 1.10 the diagrams of the processes for muon-pair production via doubly charged Higgs decay are presented.

Possible production of doubly charged Higgs bosons was investigated by the H1 Collaboration in a preliminary analysis and was presented at the ICHEP conference [H104a]. The channels $e\text{-}e$, $\mu\text{-}\mu$, $e\text{-}\mu$ with an accumulated luminosity of 118 pb^{-1} and $\tau\text{-}\tau$ (65 pb^{-1}) were studied. No indication for $H^{\pm\pm}$ - production could be observed in the analysis. Limits

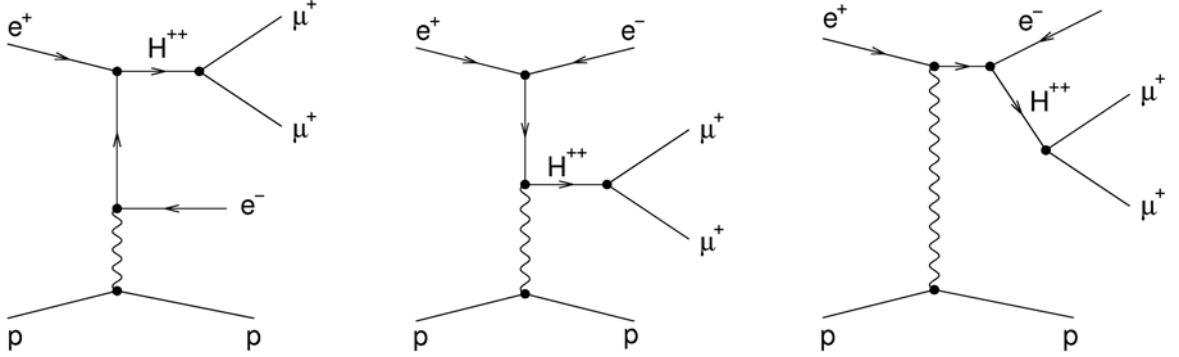


Figure 1.10: Physics Beyond the Standard Model: examples for doubly charged Higgs production in ep collisions

have been derived on the Yukawa couplings $h_{ee}^{L,R}$, $h_{e\mu}^{L,R}$ and on the $H^{\pm\pm}$ -mass. On the assumption that the doubly charged Higgs only decays in electron pairs $H^{\pm\pm} \rightarrow e^{\pm}e^{\pm}$, a lower limit on the mass was set to about 139 GeV for a value of $h_{ee}^{L,R} = 0.3$. This value corresponds to the strength of the electromagnetic coupling.

Assuming that only the process $H^{\pm\pm} \rightarrow e^{\pm}\mu^{\pm}$ exists, it was possible to determine a lower limit of about $M_{H^{\pm\pm}} \simeq 140$ GeV for a value of $h_{e\mu}^{L,R} = 0.3$. The results presented in figure 1.11 and figure 1.12 are complementary to searches performed at LEP [OPAL03], [LEP03] and Tevatron [CDF04].

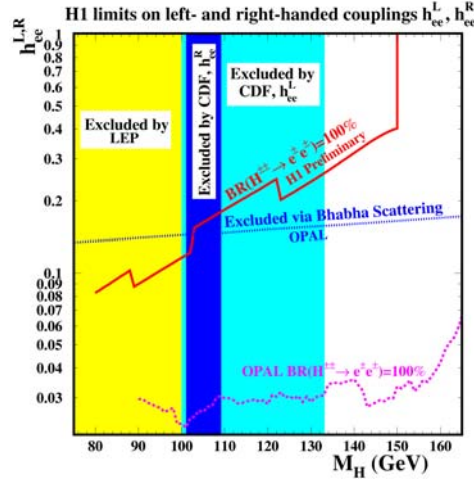


Figure 1.11: Exclusion limits on the coupling $h_{ee}^{L,R}$ at 95% confidence level as function of the doubly charged Higgs mass. The results of the H1 analysis are compared to the limits derived by other experiments, from OPAL (direct search for $H^{\pm\pm}$ -production and indirect determination of the exclusion limits via Bhabha scattering), LEP experiments [OPAL03], [LEP03] and CDF [CDF04] (direct searches).

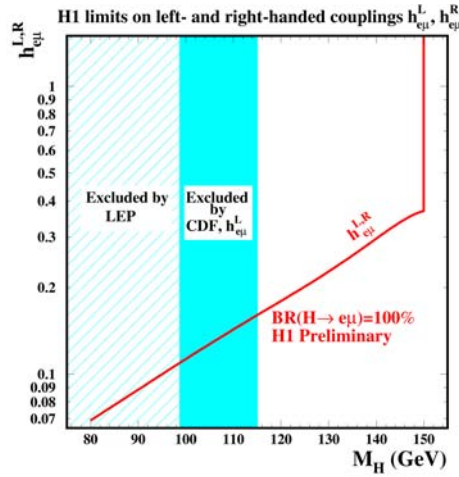


Figure 1.12: Exclusion limits on the coupling $h_{e\mu}^{L,R}$ at 95% confidence level as function of the doubly charged Higgs mass. The H1 result is compared to the results from the LEP experiments [LEP03] and CDF [CDF04] (both obtained from direct searches).

Chapter 2

Experimental Setup

In this chapter a summary is given about the storage ring HERA and the H1-experiment. The knowledge about the detector setup is important for a good understanding of the physics in the experiment.

2.1 The HERA Collider

The HERA accelerator is located at DESY in Hamburg and currently provides the only opportunity world-wide to analyse highly-energetic electron-proton collisions. Older accelerators are used to pre-accelerate electrons and protons and inject them into the HERA storage ring which has a circumference of about 6.3 km. Then the particle beams are further accelerated up to an energy of $E_{ele} = 27.6$ GeV for the electrons and $E_p = 920$ GeV (820 GeV until 1997) for the protons, and are brought to collision. The center-of-mass energy is $\sqrt{s} \simeq 318$ GeV (300 GeV until 1997).

During 1994-1998 and 2000-2004 positron-proton collisions were used. In the years 1998-1999 the positrons were replaced by electrons. In the following we will use the term “electron” in a general manner to encompass the positrons as well.

A remarkable feature of HERA is the large number of 210 bunches of protons and electrons which can be stored in the ring. The time interval between two consecutive bunch crossings is 96 ns. By comparison, the time difference at LEP was 22 μ s and will be 25 ns at the LHC.

There are two collision points at HERA where the two general-purpose experiments, H1 and ZEUS, are installed. One further place at the accelerator is engaged with the fixed-target experiment HERMES.

A schematic view of HERA can be seen in figure 2.1.

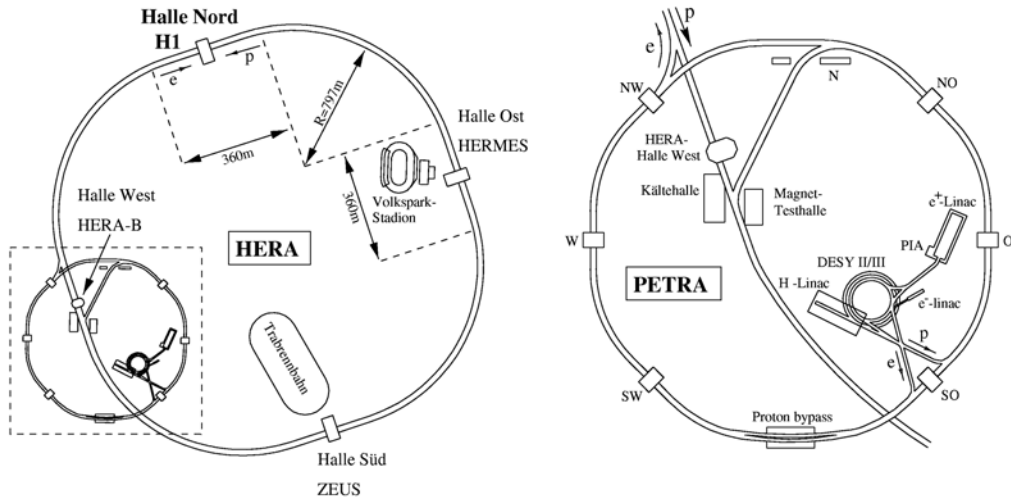


Figure 2.1: The storage ring HERA at DESY with the pre-accelerators PETRA and DESY

2.2 The H1 Detector

The H1 Detector, which is situated in the north of the HERA storage ring, measures approximately 12m x 10m x 15m and weighs about 2800 tonnes. It almost covers the total solid angle of 4π and is designed asymmetrically due to the different energy of the proton and electron beam ($E_p \gg E_{ele}$). A coordinate system in the detector is chosen in a manner that the incident protons define the z -direction. This way the y -axis points to the top and the x -axis to the center of the storage ring. The polar angle θ is measured with respect to the direction of the proton beam, the azimuthal angle ϕ is obtained in the x - y plane with respect to the x -axis.

The detector comprises a large number of different components and features which can be summarised in three main categories (from inside to out):

- **Inner tracking system:** Contains mainly three types of trackers, silicon trackers, multi wire proportional chambers and drift chambers.
- **Calorimeters:** The central region is covered by the Liquid Argon Calorimeter (LAr). Particles in backward detection can be detected by the Spaghetti Calorimeter (SpaCal) and for extremely small angles θ in forward direction by the Plug Calorimeter.

HERA Experiment H1

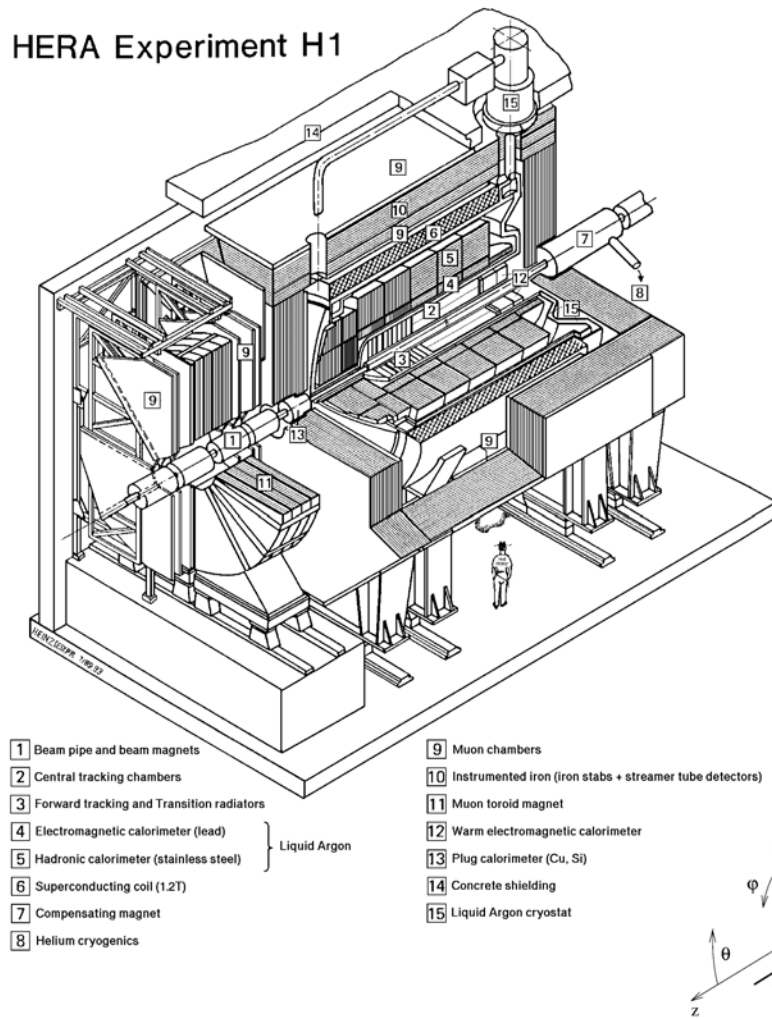


Figure 2.2: The H1 Detector: protons come from the right, and electrons from the left. The principal detector devices are explained in the text, the choice of the coordinate system is represented by the small image (bottom right).

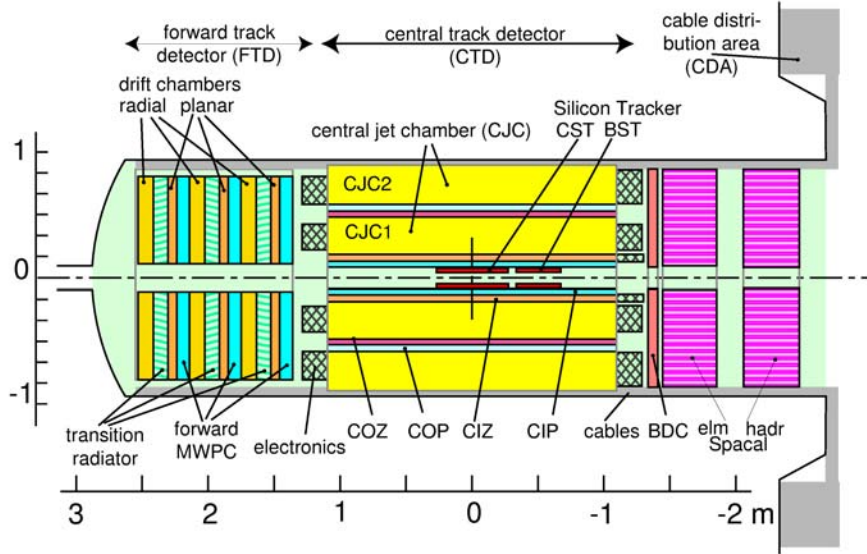


Figure 2.3: The inner tracking system of the H1 Detector.

- **Muon Detectors:** In the outer part of the detector. They consist of the Central Muon Detector and the Forward Muon System.

The calorimeters are surrounded by a superconducting coil which produces a constant \mathbf{B} -field of 1.15 T in the inner tracking system and the calorimeters. A detailed description can be taken from [H197]. An image of the full detector is shown in figure 2.2.

2.2.1 Tracking System

A schematic view of the inner tracking system can be taken from figure 2.3. It consists of the Central Tracking Device (CTD) covering the polar region $20^\circ < \theta < 160^\circ$, the Forward Tracking Device (FTD) in the range $5^\circ < \theta < 20^\circ$, and the Backward Tracking Chamber (BTC) between $153^\circ < \theta < 177.5^\circ$. In the CTD, a main part of track information is obtained by the two Central Jet Chambers (CJC) which provide a good resolution in the r - ϕ plane of $\sigma_{r-\phi} \simeq 170 \mu\text{m}$. Since the planes of anode wires are parallel to the beam axis, the resolution in z is worse reaching a value of about one percent of the wire length, corresponding to $\sigma_z \simeq 2.2 \text{ cm}$. The resolution can be improved by the CIZ and COZ, the Central Inner- and Outer z -Chambers, leading to a value of $\sigma_z \simeq 300 \mu\text{m}$.

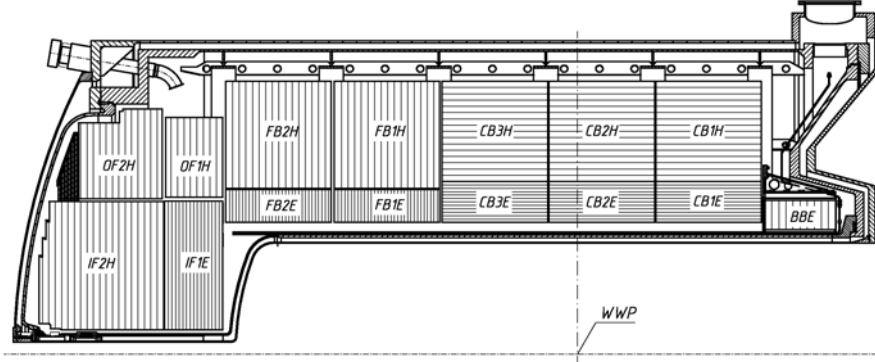


Figure 2.4: Longitudinal section of the Liquid Argon Calorimeter. The figure shows the division of the LAr in eight wheels. The segments of the electromagnetic part are denoted by an “E”, those of the hadronic part by the index “H”.

2.2.2 Calorimeters

The central region and also a part of the forward region (between $\theta = 4^\circ$ and $\theta = 153^\circ$) are covered by the Liquid Argon Calorimeter. The LAr consists of an electromagnetic inner and a hadronic outer part, both sub-divided into eight segments (“wheels”) as shown in figure 2.4. Beside the liquid argon serving as detection material, the calorimeter accommodates absorber plates. These comprise lead plates in the electromagnetic, and steel plates in the hadronic part.

The LAr is a non-compensating calorimeter, i.e. a hadron of the same energy as an electron does not dissipate the same fraction of its energy. This can be explained by hadronic decays or nuclear excitations in the absorber material, which means some energy does not contribute to the hadronic shower. Hence the electromagnetic energy resolution $(\frac{\sigma_E}{E})_{em} \simeq \frac{0.12}{\sqrt{E[GeV]}}$ is much better than the hadronic one, which is in the order of $(\frac{\sigma_E}{E})_{had} \simeq \frac{0.5}{\sqrt{E[GeV]}}$.

In the backward region ($153^\circ < \theta < 177.8^\circ$) particle detection is done by the SpaCal, a lead/scintillating-fiber calorimeter. Resolutions on the energy are $(\frac{\sigma_E}{E})_{em} \simeq \frac{0.071}{\sqrt{E[GeV]}}$ for electromagnetic particles and $(\frac{\sigma_E}{E})_{had} \simeq \frac{0.56}{\sqrt{E[GeV]}}$ for hadrons.

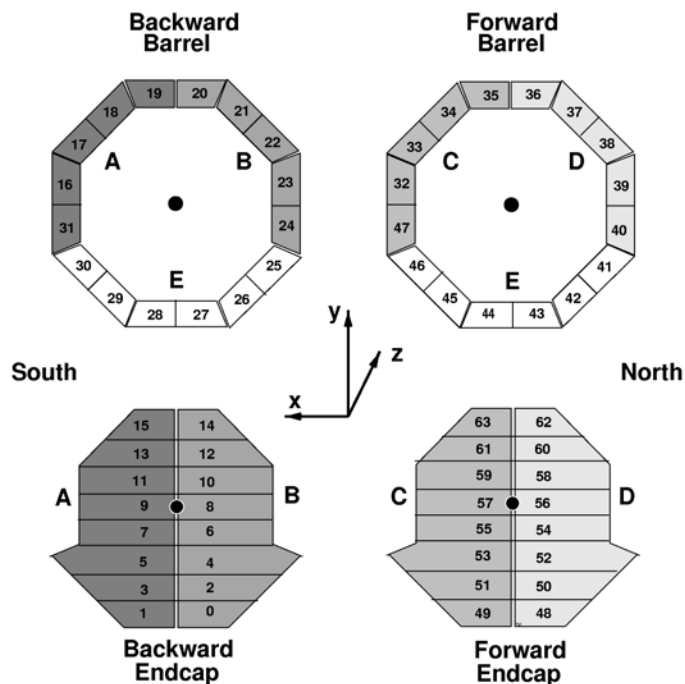


Figure 2.5: Central Muon Detector: design of the 64 modules in the four parts of the CMD.

The PLUG Calorimeter in the very forward range is designed to measure hadronic energy using copper plates as a detection material. The energy is determined with a fairly low accuracy: $(\frac{\sigma_E}{E})_{had} \simeq \frac{1.5}{\sqrt{E[GeV]}}$.

2.2.3 Muon System

The muon system is made up of two detectors: the Forward Muon Detector ($3^\circ < \theta < 17^\circ$) and the Central Muon Detector (CMD). The CMD contains four sub-detectors, the forward and backward barrel in the central range, which are complemented by the end-caps in the forward (forward endcap), and backward range (backward endcap), respectively. Each sub-detector is divided in 16 modules of the type presented in figure 2.5.

Figure 2.6 shows the composition of a single module. Between the ten iron layers with a thickness of 7.5 cm, the sensitive parts of the detector in the shape of “strips” and “pads” are mounted. The strips are drift-chambers, i.e. they are used to reconstruct tracks, whereas the pads provide calorimetric

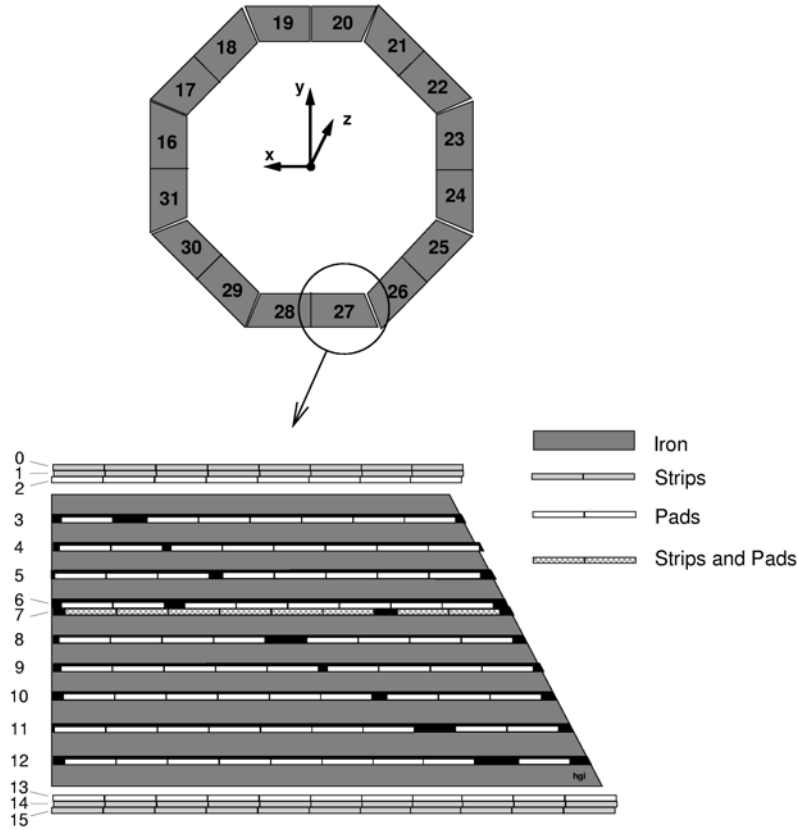


Figure 2.6: Section through an iron module: between the iron layers sensitive regions (Pads and Strips) provide the detection of hadronic or muonic signals in the instrumented iron.

information. Strips and pads can measure hadronic energy leaking out of the LAr, but they are also used for the muon detection (see Chapter 2.3). The CMD is often referred to as “instrumented iron”.

Further details can be found in [Lan98].

2.2.4 Triggers

Every 96 ns an electron bunch crosses a proton bunch at the interaction point of the detector according to a frequency of 10.4 MHz. It is evident that it is neither required nor practicable to keep all events produced in the ep collisions. Therefore triggers are used to select interesting physics events.

The readout system at H1 can only write event information to summary tape with a rate of about 10 Hz. To reduce the number of events, and subsequently the required rate, a multi-level concept was adapted consisting of five trigger levels (L1)-(L5). Each level is only activated when an event has passed the previous level. (L1)-(L4) work on-line whereas (L5) is an off-line trigger level. We give a short description of the different levels of the trigger system. A schematic view can be seen in figure 2.7:

- **Level 1 (L1)**

The first trigger level reduces the input rate of about 10 MHz to an output rate of about 1 kHz. A decision is reached within $2.3 \mu\text{s}$. Because the event information of 24 bunch crossings can be stored in pipelines, L1 can work without deadtime (the time period in which H1 cannot measure events). The validation of events is based on signals in 256 trigger elements which are associated with the measurements of the sub-detectors. So-called “sub-triggers” are created from the logical combinations of the 256 elements. If a positive decision is taken, i.e. if an event is accepted by one of the sub-triggers, the event is forwarded to the next trigger level L2, and the pipelines are stopped. From this instant deadtime starts to accrue.

- **Level 2 (L2)**

The second trigger level is required to decrease the rate to a value of about 200 Hz. If level 3 is not used, the output rate should reach a value of roughly 50 Hz. A decision is made within $20 \mu\text{s}$. L2 is built up by two triggers, a topological and a neural network trigger. The former works by combining several detector components using geometrical information, the latter is optimised in such a way that it can distinguish between interesting physics events and background.

- **Level 3 (L3)**

A third trigger level is projected to reach an improved decision during the readout. To this end, it is based on a system of micro-processors. L3 has not been put into operation so far.

- **Level 4 (L4)**

On the fourth level, the full detector information is available. 30 processor boards provide a simplified event reconstruction in order to decide (within 100 ms) if an event is permanently saved or rejected. In L4 the sub-trigger conditions of L1 are checked, and background can be excluded using adequate background finders.

- **Level 5 (L5)**

Trigger Level 5 works off-line. Here, the complete event reconstruction is available, applying calibration and correction constants to the data. The events are then sorted into physics classes corresponding to their topologies and are written on the data summary tape (DST).

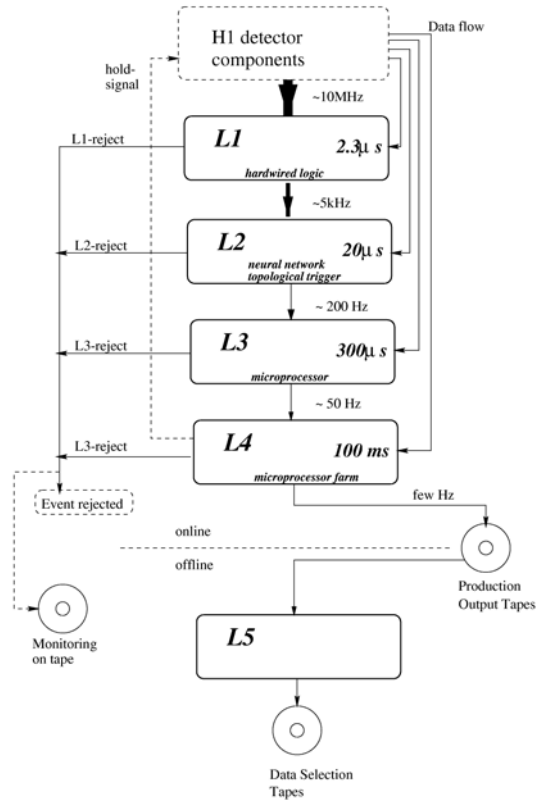


Figure 2.7: The five levels of the trigger-system at H1

Chapter 3

Particle Identification

Charged particles are characterised by their curved tracks in the detector. The signatures of electrons and muons in the experiment are very different but the identification of both particle types is based on the association to tracks. Hence, we will start the current chapter with a description of track selection, and then discuss how the electron and muon finder work.

3.1 Track Selection

Two types of tracks are reconstructed from the hits in the trackers:

- Non-vertex-fitted tracks (also called “DTNV”): segments of elementary tracks which are not necessarily associated with a vertex
- Vertex-fitted tracks (also named “DTRA”): results from non-vertex-fitted tracks that have been adapted to the primary vertex of the event

A charged particle can be represented by several track hypotheses.

The selection of “good” tracks consists of two steps following the Lee West algorithm [Wes97]. First of all the track search is carried out by quality cuts (see [H100]), then – in the case of ambiguities – the best of all selected tracks is determined.

The variables to which cuts are applied, are the transverse momentum P_T , the polar angle θ , the track length R_{length} and finally, the distance of closest approach $|d_{ca}|$ from the track to the primary vertex in the r - ϕ -plane.

Furthermore, tracks can be found in the central tracking system (“C”) by

the CJC 1 and 2, in the FTD (“F”) or in both of them (“K”). If they are associated with a primary vertex, they are labelled with “1”, if the tracks are adjusted to a secondary vertex, the label is “2”. In case of ambiguities the best track hypotheses is found by the preference “CKF” and “12”, which means that central tracks are preferred to combined tracks or forward tracks, and that tracks associated with a primary vertex are preferred to tracks from secondary vertices.

3.2 Electron Identification

3.2.1 Electron Finder

The principle behind the electron finder is to identify electrons by searching for electromagnetic clusters in the LAr calorimeter and the SpaCal. Our description will primarily focus on the identification of LAr-electrons. Further details can be found in [H100].

The particle identification is performed by general cuts, estimations which describe the characteristics of the electromagnetic shower, and by criteria that associate a track with the cluster.

The cluster candidate is required to fulfil:

- $E^{el} > 5 \text{ GeV}$
- Number of cells $N_{cell} > 3$

Several estimators are now applied to check if the cluster is electromagnetic. To take into account the different parts of the detector, the cut values on these estimators depend on θ , see [Bru98].

- Electromagnetic fraction $f_{em} = E_{em}/E_{tot}$: E_{em} denotes the energy in the electromagnetic part of the calorimeter while E_{tot} is the total cluster energy. Only cells with positive energy are taken into account.
- Transverse radius $\sigma_R = \sqrt{(\langle r^2 \rangle - \langle r \rangle^2)}$: r^n are the moments of order n of the transverse distances which are calculated by

$$\langle r^n \rangle = w^{-1} \sigma_{cell} w_i r_i^n \quad (3.1)$$

where $w_i = E_i/V_i$ is the ratio between energy and volume of the cell i , and $w = \sigma_{cell} w_i$.

- Energy fraction in the “hot” core $f_{hot} = E_{hot}^N/E_{em}$: to calculate this quantity the energy of the N most energetic cells E_{hot}^N in the neighborhood of the clusters is taken into account. Since the size of the cells varies in θ , the values of N are different for different parts of the LAr.
- Isolation criteria: In the case of electrons stemming from hadronic decay – for instance from the disintegration of a π^0 – the electron is in direct proximity to a particle jet. To reject this type of background processes, the quantity $f_{iso} = E_{tot}/E_{iso}$ is defined. E_{iso} signifies the energy in an isolation cone of radius $R_{\eta-\phi} = 0.25 \text{ rad}$. Just like above, only cells with positive energy are considered. A cluster is identified as electromagnetic if
 - either $f_{iso} > 0.98$
 - or $f_{iso} > 0.95$ and $E_{had}^{cone} < 300 \text{ MeV}$ where E_{had}^{cone} is the hadronic energy in the isolation cone.

3.2.2 Additional Criteria

In the previous section we explained how a particle is identified as an electron by the electron finder using only calorimetric information. Nevertheless, there is a certain rate of misidentification, which means that not every particle declared as an “electron” is actually an electron. For our analysis the challenge was to find the best compromise between the two conflicting goals: to minimise the rate of misidentification on the one hand, and to obtain the highest possible efficiency on the other hand. Consequently, it was necessary to impose stricter criteria on the particles than those used by the electron finder.

The phase-space is limited to values of the polar angle between

- $5^\circ < \theta_{ele} < 175^\circ$.

In this region, electrons are required to be isolated by demanding a minimal distance of 0.5 rad to other electrons and jets in the η - ϕ -plane. The total θ range can be classified into three regions according to the detector geometry:

- **Forward:** $5^\circ < \theta_{ele} < 20^\circ$.
- **Central:** $20^\circ < \theta_{ele} < 150^\circ$.
- **Backward:** $150^\circ < \theta_{ele} < 175^\circ$.

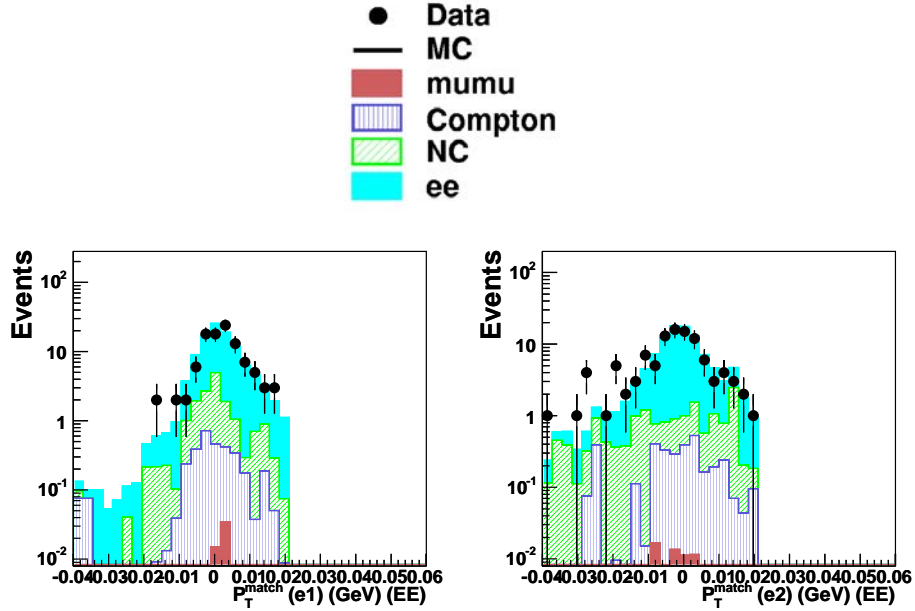


Figure 3.1: Distribution of the quantity P_T^{match} which checks the agreement between the transverse momenta of track and cluster in the central detector region. $e1$ and $e2$ are the two electrons of the di-electron channel from multi-lepton analysis (see Chapter 4.1).

The next chapter will show that the central part plays the dominant role in our analysis. In this region, where the highest track reconstruction efficiency is provided, the cluster identification is complemented by a track requirement. A “good track” has to be found which can be associated with the electromagnetic cluster. Track and cluster have to match geometrically and in P_T . The first condition is checked by extrapolating the track in the calorimeter. The distance of closest approach between track and cluster has to be smaller than 12 cm in the r - ϕ -plane. To test the P_T -matching a new variable is introduced to compare the transverse momenta of track and cluster [H103a]:

$$P_T^{match} = \frac{1}{P_T^{track}} - \frac{1}{P_T^{cluster}} \quad (3.2)$$

This quantity is required to be less than 0.02 GeV^{-1} . Its distribution for the two electrons of the di-electron channel (see Chapter 4.1) is displayed in figure 3.1.

R_{start} stands for the starting radius of the measured track. It is defined as

the distance between the z -axis and the first measured point in the central drift chambers. In order to suppress photons which convert in the central tracking system, R_{start} is required to be smaller than 30 cm. In terms of our selection, an electron is isolated if the energy in a cone of radius $R_{\eta-\phi} = 0.75$ rad around the particle is less than 2.5% of its energy. In addition, no other “good” track should be present within a distance of 0.5 rad in the η - ϕ plane.

Central Region	Forward Region
$E > 5$ GeV $E(R_{\eta-\phi} < 0.75)/E_{ele} < 2.5$ % Good isolated track with $P_T > 1$ GeV $\Delta_{extrapol. track-cluster}^{closest approach} < 12$ cm $R_{start} < 30$ cm $\Delta_{\eta-\phi}^{tr-tr} > 0.5$ rad Track-cluster matching: $P_T^{match} < 0.02$ GeV ⁻¹ ($P_T^{match} < 0.04$ GeV ⁻¹ for HERA-II) $\Delta_{\eta-\phi}^{e-e/j} > 0.5$ rad	$E > 10$ GeV $E(R_{\eta-\phi} < 0.75)/E_{ele} < 2.5$ % $\Delta_{\eta-\phi}^{e-e/j} > 0.5$ rad
	Backward Region
	$E > 5$ GeV $\Delta_{\eta-\phi}^{e-e/j} > 0.5$ rad

Table 3.1: Electron identification: chosen phase-space for electrons and identification criteria applied in addition to the Electron Finder

In the forward and backward region the probability for an electron shower is higher due to the higher material density. Moreover, since the forward trackers do not provide the efficiency level of the central trackers, the tracking requirement was removed in these regions. Thus, we apply a harsher cut to the electron energy of $E_{ele} > 10$ GeV in order to reduce the misidentification rate due to the hadronic background from DIS events. For the same reason, the electron is required to be isolated in the calorimeter. This criterion, also used in the central region, is presented in the description above. Since the jets from DIS events are detected preferentially in the forward region, we can relax the cuts in the backward region. A summary of the criteria described above is given in table 3.1.

3.2.3 Electron Identification Efficiencies

Because the reconstruction efficiency for electromagnetic clusters in the calorimeter is almost 100% [Bru98], the electron identification efficiency strongly de-

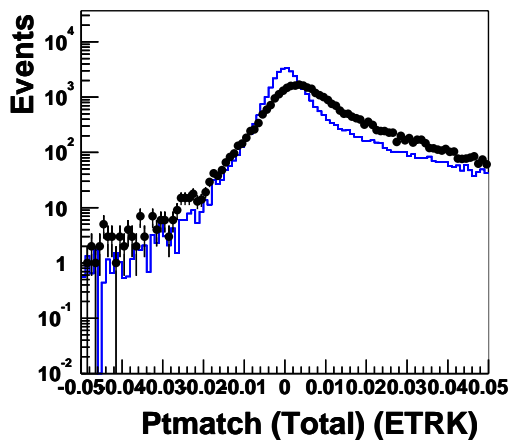


Figure 3.2: P_T -match distribution (HERA-II) for the scattered electron using an inclusive NC sample.

depends on the efficiency of associating a track with a cluster. This was checked using a NC data sample. The selection was carried out under the following criteria:

- $|z_{vtx}| < 35$ cm
- $44 \text{ GeV} < E - P_z < 66 \text{ GeV}$
- $N_{ele}^{cl} = 1$
- $P_T^{ele} > 8 \text{ GeV}$
- $20^\circ < \theta_{ele} < 150^\circ$
- electron not in the LAr cracks (spacings between different segments)
- electron isolated in the calorimeter: $E_{cone}^{R=0.75} < 1.025$

The identification efficiency is determined by the equation

$$\epsilon_{ele} = \frac{N_{ele}^{sel}}{N_{ele}^{ini}} \quad (3.3)$$

The number of events which was found when no additional cuts were applied, is denoted by N_{ele}^{ini} . Then, we looked at the total inefficiency introduced by all quality criteria and determined N_{ele}^{sel} . The criteria were given by:

- “good” track
- spatial agreement between track and cluster
- P_T -matching requirement
- $R_{start} < 30$ cm

When the P_T -match distributions for HERA-II were checked, a bad description of the data by the MC was noted (see figure 3.2). The exact reason has not been verified yet. Hence the P_T -match cut was relaxed to a value of 0.04 GeV^{-1} to guarantee a larger efficiency, and an additional inefficiency was added to the Monte Carlo.

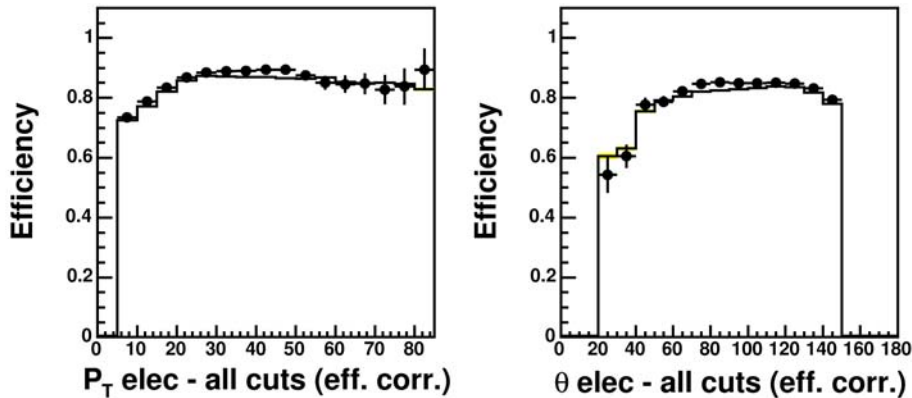


Figure 3.3: Measurement of the electron identification efficiency for 2004 data as a function of P_T (top) and θ_{ele} (bottom).

Figure 3.3 shows the result for the identification efficiency when all additional criteria were applied. The number of events N_{ele}^{sel} was compared to the initial data sample. ϵ is plotted as a function of P_T and θ . After correction of the efficiency in the MC, data are well described by the simulation. An identification efficiency of about 80% is reached in the central region between $40^\circ < \theta < 150^\circ$.

From this plot, the systematic error on the electron identification efficiency was determined to be 3% in the backward region and 15% in the forward region.

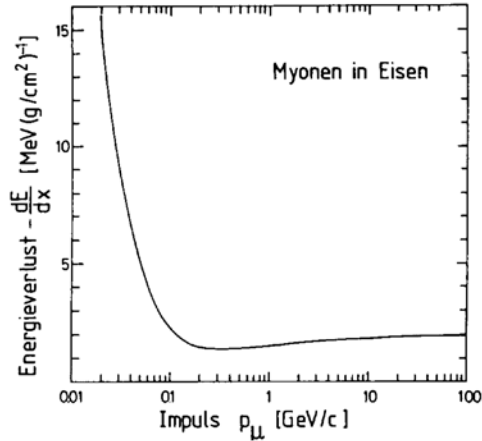


Figure 3.4: Mean energy loss for muons in iron as a function of the muon momentum

3.3 Muon Identification

3.3.1 Muon Finder

While an electron loses most of its energy by Bremsstrahlung leading to an electromagnetic shower in the calorimeter, this effect is only marginal for muons because of their high mass. Since muons do not participate in the strong interaction, they only lose a small fraction of their energy due to the ionisation of atoms in the traversed material. This type of energy loss depends on both the energy and the momentum and can be described by the Bethe-Bloch formula. In figure 3.4 $(-dE/dx)$ in iron is plotted as function of the muon momentum. It can be seen that the ionization is minimal at around 200 MeV. For higher momenta it hardly differs from the minimum value because $(-dE/dx)$ only increases logarithmically. Thus the muons in the detector are called “minimal ionising particles” depositing an energy of about 10 MeV per centimeter traversed in the liquid argon.

Muons with an energy greater than 1-2 GeV can reach the Central Muon Detector (CMD). Most muons are detected by hits in the CMD linked to an inner track in the tracking system. A smaller amount of muons is identified by a minimal ionising pattern in the LAr, associated with an inner track. These two principles are implemented in the muon finder [H100]. As in the case of the electrons before, the track linking can be ambiguous, which

means that different inner tracks are associated with a hit pattern in the instrumented iron. To solve the linking problem different hypotheses are set up, one for each track combination. The hypotheses are classified into five quality grades where “1” is the best and “5” the worst grade, in order to find the best muon candidate. In the following a description of each grade will be provided:

- **Grade 1: Iron muons linked by the H1REC**

If tracks are found both in the inner tracking system and the muon system (instrumented iron or Forward Muon Detector), the H1 reconstruction software [H1REC] extrapolates inner tracks with $P_T > 1$ GeV to the instrumented iron. The iron track is defined by the position of the first hit seen from the vertex side, its direction at this position, and the ratio between charge and momentum [Kae00].

The tracks can be linked if the following criteria on the polar angle

$$|\theta_{inner} - \theta_{iron}| < 0.2 \text{ rad} \quad (3.4)$$

and on the azimuthal angle

$$\begin{aligned} -\frac{\pi}{2} < (\phi_{inner} - \phi_{iron}) < 0.2 \text{ rad} & \quad \text{if } \kappa > 0 \\ -\frac{\pi}{2} < (\phi_{iron} - \phi_{inner}) < 0.2 \text{ rad} & \quad \text{if } \kappa < 0 \end{aligned} \quad (3.5)$$

are satisfied [Kae00], [Lan98]. The link probability is obtained from a χ^2 -test by

$$\chi^2 = (\mathbf{x}_{extra} - \mathbf{x}_{inner})^T \mathbf{V} (\mathbf{x}_{extra} - \mathbf{x}_{inner}). \quad (3.6)$$

The vectors \mathbf{x}_{extra} and \mathbf{x}_{inner} are constructed from parameters of the extrapolated and inner tracks, respectively. These parameters are the z-coordinate and the azimuthal angle ϕ_{point} of the first track point, and the direction of flight ϕ_{flight} at that point. The link probability is required to exceed a threshold value which is normally chosen to be 10^{-4} .

Since signals in the muon system might have been faked by hadrons (e.g. pions or kaons) a set of additional cuts is applied on the muon candidates in order to suppress this kind of background. The variables which we place cuts on, are: ρ_0 , which is the smallest distance between an extrapolation of the iron track to the vertex in the r - ϕ plane, z_0 , which denotes the z-coordinate of the starting point of the iron track, and n_{layers} , which is the number of hit layers in the muon detector. The cut values are shown in figure 3.5.

Iron muons with track in			
Forward endcap		Backward endcap	
ρ_0	< 100 cm	ρ_0	< 100 cm
z_0	< 100 cm	z_0	< 100 cm
n_{layers}	≥ 6	n_{layers}	≥ 3
first layer	≤ 5	first layer	≤ 8
last layer	≥ 6	last layer	≥ 3
Barrel		Forward muon toroid	
ρ_0	< 100 cm	track quality	= 1 2
z_0	< 100 cm	z_0	> -400 cm
n_{layers}	≥ 2	z_0	< 300 cm
first layer	≤ 5		
last layer	≥ 2		

Figure 3.5: Cuts on iron muons to suppress hadronic background from [H100]

- **Grade 2: Iron muons matched in η - ϕ**

Grade 2 muons are identified in a similar way to grade 1 muons by linking an iron track to an inner track. Unlike grade 1, the criteria on the link probability is replaced by a calculation of the distance between the tracks in the η - ϕ metric. The candidates have to fulfil the criterion:

$$\Delta_{\eta-\phi} = \sqrt{(\eta_{iron} - \eta_{inner})^2 + (\phi_{iron} - \phi_{inner})^2} < 0.5 \text{ rad} \quad (3.7)$$

- **Grade 3: Tail catcher muons matched in η - ϕ with an inner track**

Each layer of the modules in the CMD is equipped with pad-electrodes which measure the hadronic energy leaking out of the calorimeter. Hence the pads are called “tail catchers”. They can also be used to record muons, especially in regions where the reconstruction efficiency for iron tracks is reduced due to geometrical features, e.g. gaps between different modules of the instrumented iron. The link between the track found by the tail catchers and an inner track is accepted if the η - ϕ -criteria of grade 2 are fulfilled.

The large amount of hadrons which are detected by the tail catchers can be reduced by a cut on the energy deposit around the extrapolated inner track in the calorimeter.

- **Grade 4: Muons detected in the LAr**

Since we will not use grade 4 or 5 muons in our analysis, we will only

refer briefly to them. Muons which stop in the calorimeter due to their low energy, can be detected by the resulting minimal ionising pattern. To check if the pattern belongs to a muon, a set of estimators is used, for instance the energy deposit around the extrapolated inner track. A classification of the muon quality is carried out.

- **Grade 5: Iron muons in the forward muon toroid without association to an inner track**

Due to the poor reconstruction efficiency in the forward tracking system, it is possible to detect a signal in the forward muon toroid which cannot be ascribed to an inner track. Since the momentum of forward muons is measured in the forward muon toroid with high accuracy, particle kinematics can be determined successfully in this case.

The algorithm to find the best hypothesis from all the created and graded muon candidates is explained in [H100]. Initially, it is searched for a grade 1 muon, then if the grade 1 conditions could not be satisfied, the criteria of grade 2 are checked and so on. When the best hypothesis has been found, all other possibilities are excluded from further processing.

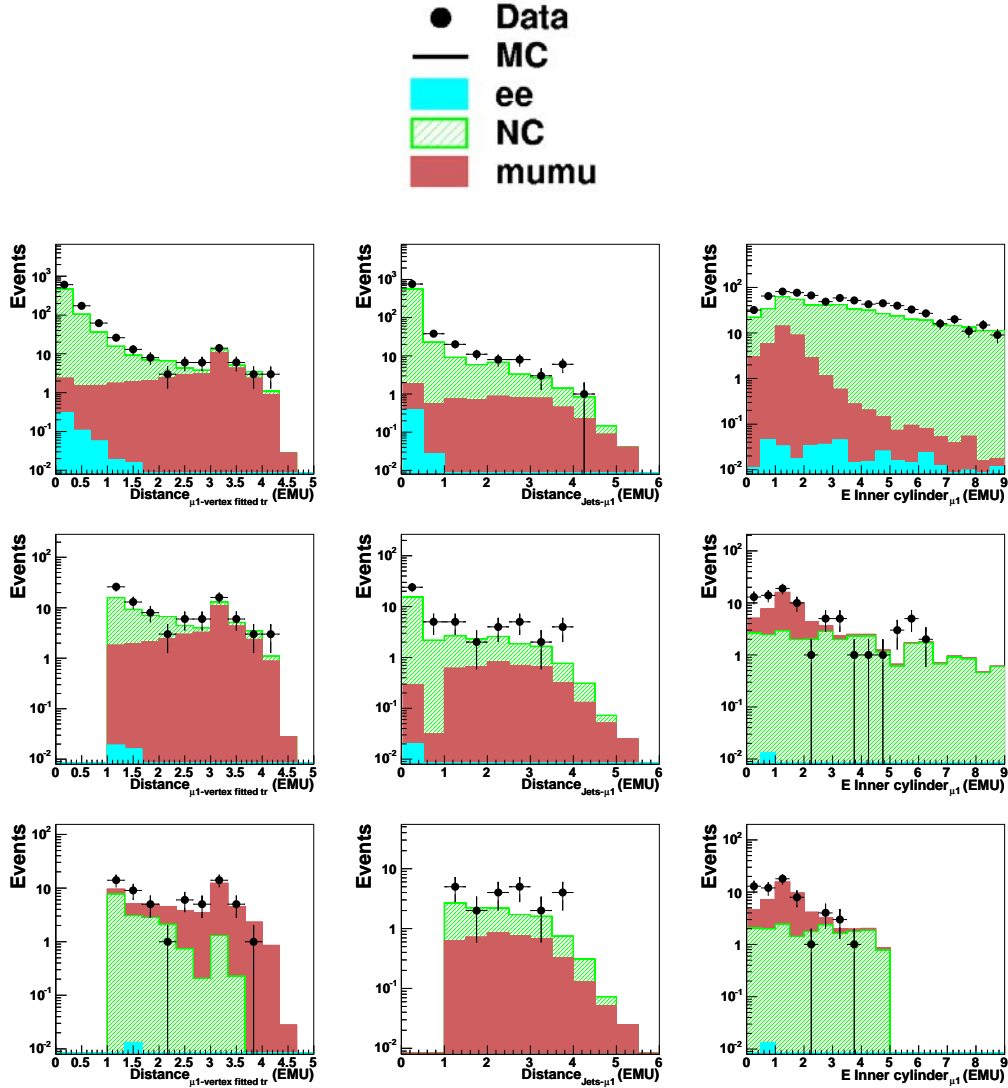
3.3.2 Additional Criteria

To reduce the background due to misidentified muons, and consequently to analyse a purer data sample, we only select muons up to grade 3. Hence, an iron signal is required which can be associated with an inner track. Since the reconstruction in the forward and backward tracking system does not reach the level of the central region, the restrictions to the phase-space are even larger for muons than for electrons. We demand:

- $20^\circ < \theta_\mu < 160^\circ$
- $P_{T\mu} > 2 \text{ GeV}$.

The muon is isolated if the non-muonic energy surrounding the particle does not exceed a certain threshold value. To calculate this, we define a cylinder of radius $R = 0.5$ units in η - ϕ around the particle track. The non-muonic energy in this cylinder is required to be less than 5 GeV. To reduce background muons stemming from the decay of hadrons or b -quarks, the distance between the muon track and other tracks or jets is required to be greater than 1 rad in the η - ϕ plane. To summarise:

- $E_{cone}^{calo} < 5 \text{ GeV}$



- $\Delta_{\eta-\phi}^{tr-tr} > 1$ rad
- $\Delta_{\eta-\phi}^{tr-jet} > 1$ rad

The effect induced by the cuts can be illustrated for the e - μ -channel of the multi-lepton analysis (see Chapter 4.1) where one electron and one muon are detected in the final state.

The situation before the cuts in the e - μ -channel is displayed in figure 3.6 (top) for the distance between the muon and tracks, the muon and jets and the non-muonic energy in a cone. The channel is dominated by the NC-background. This background can be partially reduced when the muon is required to be separated from other tracks (figure 3.6 center). A more sophisticated selection is reached when the muon is isolated against jets and non-muonic energy fractions in the calorimeter (figure 3.6 bottom).

A large part of the NC-background has been suppressed by the chosen cuts.

3.3.3 Triggers for the Muon Selection

Choice of Sub-Triggers

The multi-level concept of the triggers has been presented in Chapter 2. After an event has passed the last trigger level, the information, from the subtriggers in level 1, is still available. As we have already mentioned, the sub-triggers combine the signals from different detector components. Hence, it is possible to preselect events by choosing one or more sub-triggers according to the required event topology. In the case of the di-muon channel, we use sub-triggers designed for muon-identification. Specifically, we look at s19, s22, s34 and s56 for HERA-I, and at s18 for HERA-II and describe them as follows:

- **s19:** Combines muon signals in the barrel with high track multiplicities.
- **s22:** Requires a signal in the outer endcaps in combination with high track multiplicities.
- **s34:** Corresponds to s19, but uses low track multiplicities.
- **s56:** Trigger which combines a signal in one of the muon detectors with a signal in the SpaCal.
- **s18:** HERA-I: Signal in the outer endcaps in combination with low track multiplicities.
HERA-II: Unifies former s18 and s19 trigger, requiring a signal in the barrel or the endcaps.

An event is kept if it has been accepted by at least one of the sub-triggers used.

Prescaling of Sub-Triggers

In order to reduce the event rates within the multi trigger levels, sub-triggers with a high rate have to be prescaled with a factor d . This means that only the fraction $(1/d)$ of the events accepted by the sub-trigger is forwarded to the next level. Prescaling may be necessary if topologies with high event rates are studied, as for example in a low- P_T muon analysis. In our case we do not consider prescaled sub-triggers.

Trigger Efficiencies

The efficiency for Monte Carlo events can be calculated by the simple formula

$$\epsilon_{trig} = \frac{N_{trigg\ evts.}}{N_{all\ evts.}} \quad (3.8)$$

dividing the number of triggered by the total number of events. However, the determination for a data sample is more complicated because all events in the data not set by at least one of the sub-triggers of L1 will be lost forever. This problem can be handled by the use of a bias-free reference sub-trigger. If N is the total number of events in the sample, the number of events N_1 , N_2 and N_{12} triggered by the sub-triggers 1, 2 and the combination of 1 and 2 (logical AND: 1&&2) is given by:

$$\begin{aligned} N_1 &= N \cdot \epsilon_1 \\ N_2 &= N \cdot \epsilon_2 \\ N_{12} &= N \cdot \epsilon_{12} \end{aligned} \quad (3.9)$$

If we define ϵ_1^* (ϵ_2^*) as the efficiency for subtrigger 1 (2) provided that sub-trigger 2 (1) is set, we can write the third line of (3.9) like this:

$$N_{12} = N_1 \cdot \epsilon_2^* = N_2 \cdot \epsilon_1^* \quad (3.10)$$

Using a bias-free event sample, for independent subtriggers 1 & 2 $\epsilon_1 = \epsilon_1^*$ (and $\epsilon_2 = \epsilon_2^*$, respectively), and the efficiency of trigger 2 can be evaluated by

$$\epsilon_2 = \epsilon_2^* = \frac{N_{12}}{N_1} \quad (3.11)$$

In our analysis we followed the idea of an efficiency measurement provided in [Lei02]. The following data / MC-sample was used:

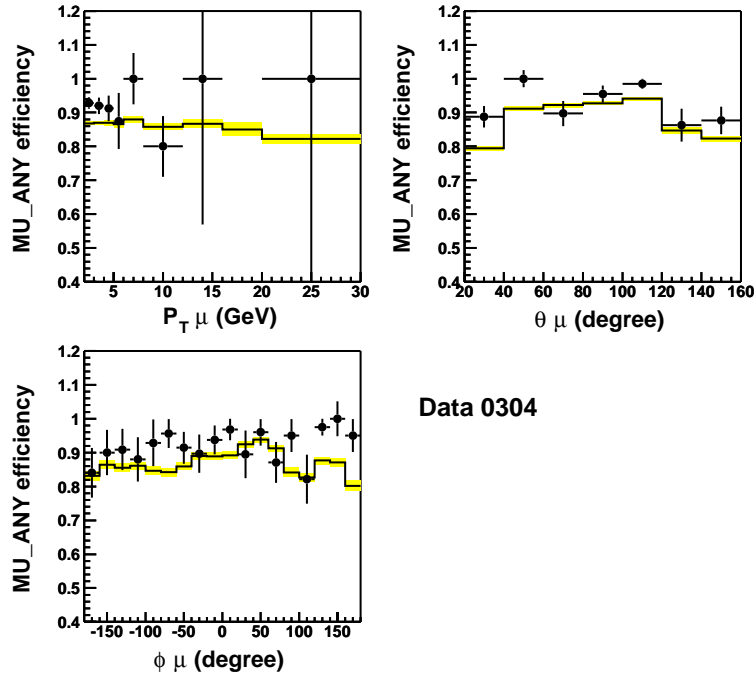


Figure 3.7: Efficiency of muon trigger elements in the endcaps and the barrel (2004 data)

- di-muon sample corresponding to multi-lepton analysis with
- $P_{T_{\mu_{1,2}}} > 2 \text{ GeV}$

The cuts on transverse momentum were relaxed to guarantee better statistics.

The efficiency was calculated for signals from the barrel (MU_BAR), disjunctions of trigger signals from the endcaps (MU_ECQ), and from the endcaps and the barrel (MU_ANY). As an independent reference or “monitoring” trigger, all sub-triggers, which do not contain trigger elements from the muon detector, were used. The efficiency for the combination of barrel and endcaps for 2004 data is displayed in figure 3.7 as function of P_T and the polar angle θ of the muon. The triggers were simulated by the Monte Carlo and then, the efficiency was calculated in the same way as for the data. The graphics show that the MC simulation of the triggers provides a good description of the data. The systematic uncertainties on the trigger can be obtained from the differences between data and MC. They were determined to a value of 5% for HERA-I and 10% for HERA-II.

3.3.4 Muon Identification Efficiencies

To check the reconstruction efficiency of muons, we used an elastic sample containing one identified muon and an additional track which was not associated with the first muon. The following cuts were applied to select the sample:

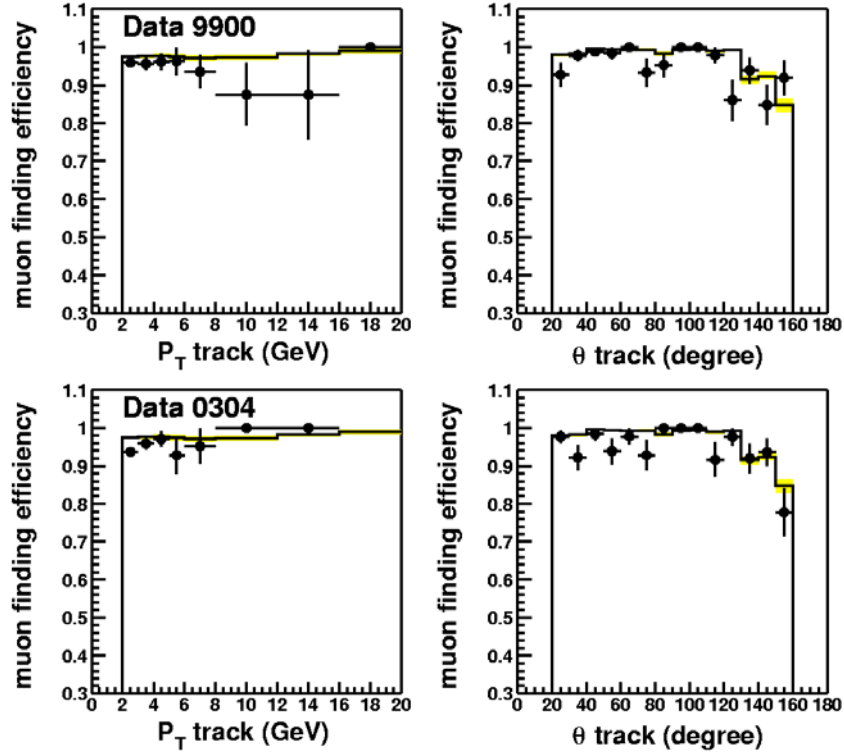


Figure 3.8: Identification efficiency of muons checked with a 1999-2000 data sample (top) and a 2004 data sample (bottom).

- $P_T^{tr1,2} > 2$ GeV
- exactly 2 “good” tracks in the event
- $P_T^{miss} < 10$ GeV
- $20^\circ < \theta_{tr} < 160^\circ$
- Distance between the z -vertex and the interaction point $|z_{vtx}| < 35$ cm
- Opening angle between the tracks $\alpha < 160^\circ$

- No electrons, no jets

The efficiency was then calculated by the formula

$$\epsilon_{\mu} = \frac{N_{\mu\mu}}{N_{all}} \quad (3.12)$$

where N_{all} is the total number of events with one “good” muon plus one track and $N_{\mu\mu}$ is the number of events with two identified muons. The result is presented in figure 3.8 for 1999-2000 and for 2004 data. We see a good agreement between data and Monte Carlo for both samples with an identification efficiency around 95%. In the backward region a lower efficiency is reached. The systematic error on the identification efficiency is taken from the difference between data and MC leading to a value of 5%.

3.4 Systematic Errors

To be able if we want to compare data and theoretical prediction correctly, we have to take systematic uncertainties into account. These can be classified into two groups, those of an experimental nature and those of a theoretical nature. The description will start with the experimental errors concerning the measurement of quantities and particle identification.

3.4.1 Experimental Uncertainties

The following experimental uncertainties are considered in our analysis:

- **Energy** For electrons the error depends on the z -range varying from 0.7% to 3% for the HERA-I [Hei99] and from 1.5% to 3% for the HERA-II run [H104c]. For muons the error on the energy is derived from the error on the track curvature. It is of the order of 5% [Lei02].
- **Polar Angle** The uncertainties on theta have been studied in detail in [H103b]. For HERA-I the error is determined to 3 mrad (electrons and muons) and is even higher for HERA-II, estimated at 5 mrad. The difference is justified because the alignment-correction of the LAr calorimeter with respect to the tracking system for the HERA-II run has not been calculated and applied yet.
- **Identification Efficiency** For muons a relative value of 5% was taken, for the electrons the error varies on θ_e from 3% up to 15%.

- **Trigger** The error on trigger efficiency for electrons and for muons was determined to 5%. (10% for HERA-II).
- **Luminosity** Errors of 1.5% for HERA-I and 3% for HERA-II on the measurement of luminosity are taken into account.

3.4.2 Theoretical Uncertainties

The Monte Carlo Generators used here, only contain calculations on tree level. Therefore, they neglect higher order contributions leading to a systematic error on the simulation.

- **GRAPE** The generator GRAPE which is used to simulate the signal (see 1.2.5) does not consider lepton pairs produced by Bremsstrahlung from the proton side or by the resolved Drell-Yan process. In addition, the limited knowledge about the proton structure causes uncertainties in the case of the inelastic lepton pair production. The error is of the order of 3% [H103a].
- **NC/COMPTON** To estimate the uncertainty on the background prediction, several samples in which NC- or COMPTON-processes are enhanced, were studied [H103a]. A value of 20% has been found in these studies.

Chapter 4

Multi-Lepton Analysis

The previous chapter showed how electrons and muons are selected. The criteria have been applied in order to maintain data quality and to reduce the number of misidentified particles. We will now present the idea of the multi-lepton analysis. Since the search for tau-topologies is not part of this diploma thesis, the term “lepton” will be used in the following in a general manner for “electrons” and “muons” whereas the terms “electrons” and “muons” will only stand for the particles which have passed all requirements presented in Chapter 3, and enter the final selection.

It will be seen that the analysis is structured by two main classes, one for two leptons $l-l$, and one for three leptons $l-l-l$, according to the number of leptons in the final state. The criteria a lepton has to pass in order to enter one of the classes will treat electrons and muons in the same way. The only exception is necessary by additional cuts in case of two muons where the sample is dominated by a big number of cosmic muon events.

From the main classes $l-l$ and $l-l-l$, the electron/muon classes, e.g. $e-e$ or $e-\mu-\mu$, can be derived as sub-classes. We will present the results for the HERA-I and -II data and will compare them to the Standard Model prediction. An extra section will be provided to discuss the high mass candidates at $M_{12} > 100$ GeV.

4.1 Lepton Selection Criteria

4.1.1 Phase-space for Electrons and Muons

As described above, the final lepton selection is set up by the di-lepton class $l-l$ and the tri-lepton class $l-l-l$ corresponding to the number of particles in the events ($n_l = 2$ and $n_l = 3$, respectively). Events with $n_l > 3$ are also

accepted. The lepton generations are merged, i.e. no distinction is made between electrons and muons, and the particles are sorted by decreasing transverse momentum:

$$P_{T_{i1}} > P_{T_{i2}} (> P_{T_{i3}}) \quad (4.1)$$

An isolation between the leptons is realised by the cut

$$\sqrt{(\Delta\eta)^2 + (\Delta\phi)^2} > 0.5 \text{ rad} \quad (4.2)$$

in the η - ϕ -plane.

Di-Lepton Class

The di-lepton channel suffers more from impurities induced by background than the tri-lepton channel. To reject the particles, the photons, pions and other hadrons which fake electron or muon signatures, we must implement tight cuts in the di-lepton class. The necessary criteria which are based on a conjunction between different particle signatures – a cluster-inner track linking in case of electrons, an inner-outer track linking for muons – can only be provided in the central region (see the previous chapter).

Beside the limitation on the θ -range, the phase-space is also cut on the transverse momentum in order to improve data quality. In addition, the chosen P_T -cuts will completely reject the J/ψ -production. Lepton events due to the Υ -decay are suppressed at roughly 100%. The restrictions on the phase-space are summarised in table 4.1. From the di-lepton class l - l the e - e , μ - μ , and e - μ sub-classes can be derived.

Transverse Momentum	Polar Angle
$P_{T_{i1}} > 10 \text{ GeV}, P_{T_{i2}} > 5 \text{ GeV}$	$20^\circ < \theta_{l1,2} < 150^\circ$

Table 4.1: Di-lepton selection: Restrictions on the phase-space.

Tri-Lepton Class

In the tri-lepton selection two central leptons are required which fulfil the criteria described above. The third lepton is allowed to have any energy, any transverse momentum or any polar angle which correspond to the preselection criteria on electrons and muons presented in Chapter 3.

The tri-lepton class l - l - l contains the sub-classes e - e - e and e - μ - μ .

4.1.2 Anti-cosmics Rejection

In the $\mu\text{-}\mu$ channel a lot of background remains which could not be eliminated by the selection criteria applied on the leptons so far (Chapter 3 and Chapter 4.1.1). The main source of this background are the so-called “cosmic muons”. They are produced by high-energy protons from cosmic radiation interacting with nuclei in the atmosphere. In a first step, charged pions are generated which decay subsequently into muons:

$$p + \text{Nucleus} \longrightarrow \pi^\pm + X, \quad \pi^\pm \longrightarrow \mu^\pm + \bar{\nu}_\mu(\nu_\mu) \quad (4.3)$$

Typically, the cosmic muons are produced in an altitude of about 15 kilometers, but due to the long life-time ($\tau_\mu \simeq 2.2 \cdot 10^{-6}$ s) and the large γ -factor (close to c), they are able to reach the sea level.

In [Lei02] a detailed study is dedicated to the cosmic background. It is shown that the cosmics, which enter the H1 detector, can be distinguished from the di-muon events stemming from ep-interactions, by different features:

- Distance from the interaction point
- Timing behavior
- Collinearity

The cuts applied to reject the cosmic background, are summarised in table 4.2.

Feature	Chosen Cut
z -Component of vertex	$ \Delta_{zvx} \leq 35$ cm
Event timing	$\Delta t_0 = (\text{Event-}t_0 - \bar{t}_0) < 25$ ticks
Opening Angle	$\alpha_{\mu 1,2} < 160^\circ$
Sum Theta	for $\alpha_{\mu 1,2} > 150^\circ$: $\theta_{\mu_1} + \theta_{\mu_2} < 170^\circ \ \ \theta_{\mu_1} + \theta_{\mu_2} > 190^\circ$

Table 4.2: Di-muon channel: Rejection of background due to cosmics.

Cosmics prefer to enter first the upper part of the detector, but there is no favoured region along the z -axis. Therefore, the reconstructed vertex of a cosmic event can be far away from the interaction point whereas the

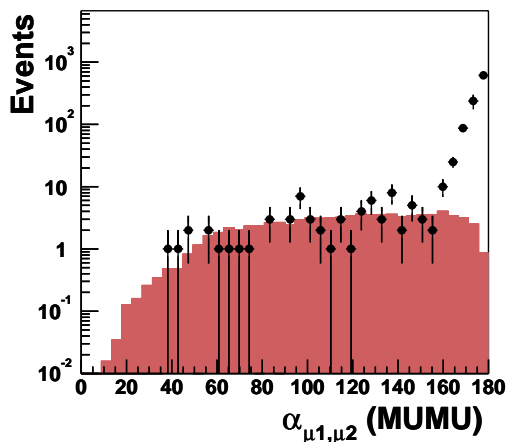


Figure 4.1: Cosmics rejection due to the collinearity of the particles: for opening angles greater than 160° data exceed the Monte Carlo at about two orders of magnitude due to cosmic events.

probability for ep -events decreases if the distance is increased. A cut can be applied to the variable $|\Delta_{zvtx}|$ which marks the spacing between the nominal and the reconstructed vertex.

Events can also be distinguished by their timing behaviour. While the cosmics pass the detector uniformly distributed, physics events are correlated to the “HERA-Clock” which is associated with the crossover of electron and proton bunches. They follow the HERA-clock in a normal distribution around the mean value \bar{t}_0 of the run period. In our selection, the difference Δt_0 between the mean t_0 and the Event- t_0 , measured by the CJC’s, is required to be smaller than 25 “ticks”, about 25 ns.

To check the collinearity of the two muons, a quantity has to be defined which correlates the muon pair. Here the opening angle between μ_1 and μ_2 is chosen, given by:

$$\cos \alpha = \frac{\mathbf{P}_{\mu 1} \cdot \mathbf{P}_{\mu 2}}{|\mathbf{P}_{\mu 1}| |\mathbf{P}_{\mu 2}|} \quad (4.4)$$

In the case of cosmics where there is only one particle faking a muon-pair, it is evident that α will be calculated to values close to 180° . A big amount of cosmics can be rejected by requiring an opening angle of $\alpha < 160^\circ$. Figure 4.1 shows the situation before the cut. It can be noted that data are in good agreement with the theoretical expectation up to an opening angle of 160° . Unlike the cross-section $\sigma_{\gamma\gamma}$ of the two-photon process (see the Monte Carlo distribution) data increase quickly in this region due to the cosmic

muon events.

Additionally, a cut on the sum of the polar angle of the muon-pair was used in [Lei02] if $\alpha > 150^\circ$. By this criterion, which is also implemented in our analysis, two events of 68 have been rejected as cosmics.

4.1.3 P_T Correction by the “ P_T -Balance Method”

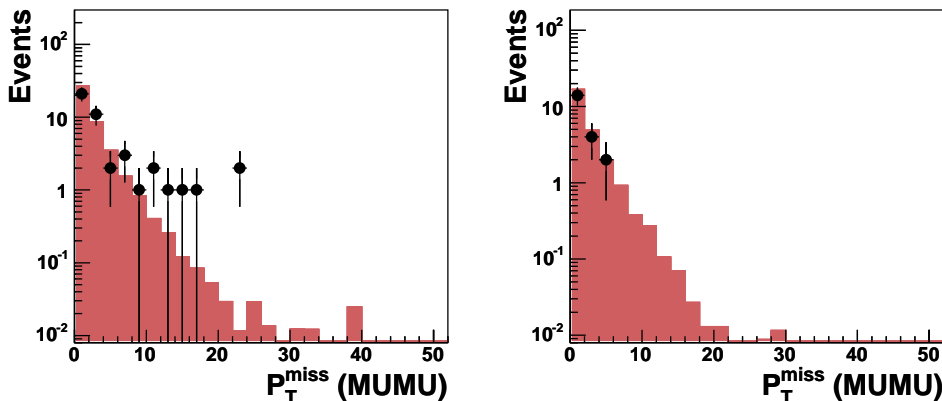


Figure 4.2: Check of transverse momentum conservation: distributions of P_T for HERA-I (left) and HERA-II data (right) in the μ - μ channel.

The muon momentum is determined by the curvature of the particle track. The error on the transverse momentum, obtained likewise from the information of the trackers, is between 2-5%. In the case of high P_T events, where the curvature is very small, too high values of P_T are determined. If only the transverse momentum of one particle is over-estimated, a high value of missing transverse momentum P_T^{miss} will be observed as a consequence. Figure 4.2 shows the P_T^{miss} distributions in the di-muon channel. The missing transverse momentum in the MC events can go up to 20 GeV. The slope is described by data. Hence, the goal is to correct the initial P_T -values for muons. The method chosen to do this, is called P_T -Balance and is based on the assumption that the total transverse momentum of the event is zero:

$$P_x = P_y = 0 \quad \Rightarrow \quad P_T^{miss} = \sqrt{P_x^2 + P_y^2} = 0 \quad (4.5)$$

Furthermore, since only the momentum of the muon with the biggest error on P_T will be corrected, it is presumed that the momenta of the other particle(s)

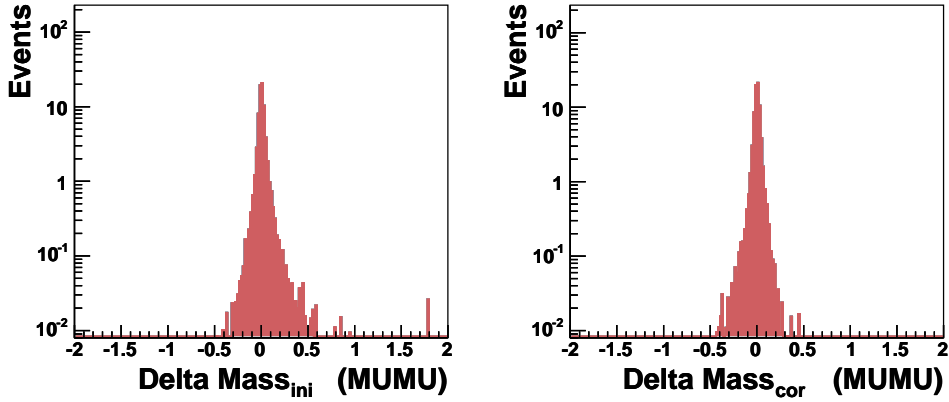


Figure 4.3: Comparison of reconstructed and generated invariant masses before and after the P_T -balance.

in the event are determined properly.

The total momentum vector of an event with two muons is

$$\mathbf{p}_{tot} = \mathbf{p}_{\mu 1}^{ini} + \mathbf{p}_{\mu 2}^{ini} + \mathbf{p}_{res}. \quad (4.6)$$

\mathbf{p}_{res} is the residual momentum due to electrons or hadrons.

We calculate the difference between the total momentum \mathbf{p}_{tot} and the momentum of the muon with the bigger error $d(P_T^{rel})$. Without loss of generality here it is supposed to be muon 1:

$$\mathbf{p}_{dif} = \mathbf{p}_{tot} - \mathbf{p}_{\mu 1}^{ini} \quad (4.7)$$

Now we have

$$\mathbf{p}_{\mu 2}^{ini} = \mathbf{p}_{\mu 2}^{cor} \quad (4.8)$$

and

$$\mathbf{p}_{Tdif} = \mathbf{p}_{T\mu 1}^{cor}. \quad (4.9)$$

The effect of the method was tested on a MC GRAPE sample. The invariant masses of the reconstructed particles M_{12}^{rec} were compared to the invariant masses of the generated particles M_{12}^{gen} :

$$\Delta_M = \frac{M_{12}^{rec} - M_{12}^{gen}}{M_{12}^{gen}} \quad (4.10)$$

The distributions of Δ_M are shown in figure 4.3. On the left, the initial mass of the reconstructed particles has been used, on the right Δ_M is displayed when the P_T -correction has been performed. This way the resolution of the mass is improved and the tail on the right side of the distribution is removed.

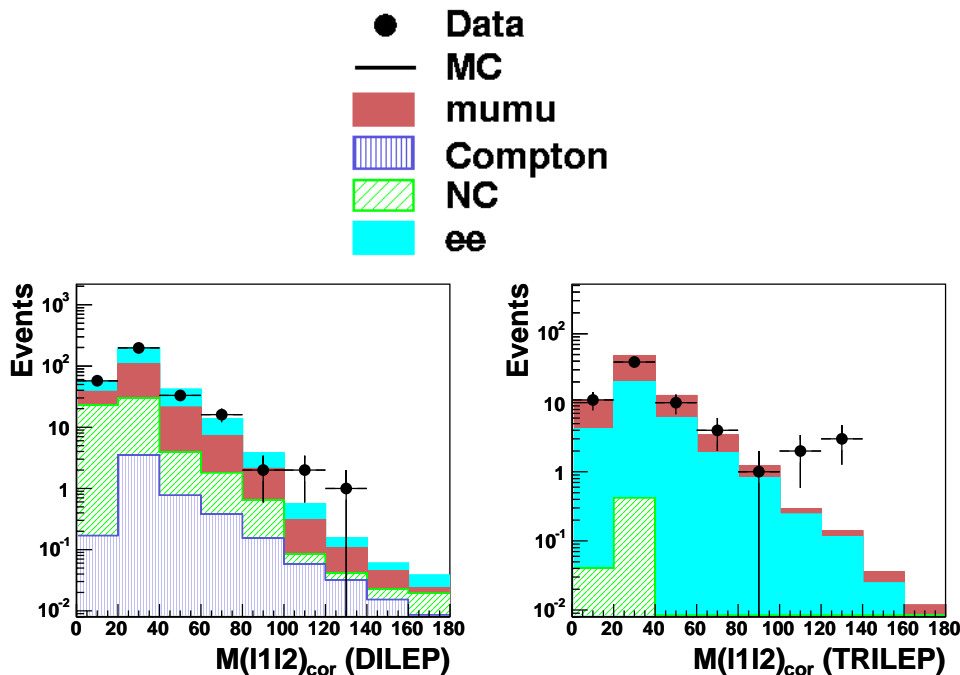


Figure 4.4: Invariant mass distributions of the two highest- P_T leptons for the total 1994-2004 sample in the di-lepton (left) and the tri-lepton-channel (right).

4.2 Results of the Analysis

In section (4.1) we describe the cuts of our final selection and illustrate which way the cosmic events in the di-muon channel can be suppressed. We will now present the results of the multi-lepton analysis covering HERA-I and -II data with an integrated luminosity of 172 pb^{-1} . We will start with a general discussion focussed on the characteristic variables, the invariant mass of the two highest P_T -leptons, M_{12} , and the sum of transverse energies $\sum E_T$, and then proceed with a detailed description of each channel.

The invariant mass distributions of the two highest- P_T leptons are presented in figure 4.4 for the di- and the tri-lepton channel.

Both in the di-lepton and in the tri-lepton class, data are in good agreement with the Monte Carlo simulation. It is excellent for smaller invariant masses where statistics are good. In the region of high M_{12} we observe a slight excess of data compared to the Standard Model prediction. For the di-lepton channel the three high-mass $e-e-e$ events, found in the Multi-Electron Anal-

ysis [H103a] (see also Chapter 1.5), become manifest in the presented plot. In the tri-lepton channel five events with invariant masses $M_{12} > 100$ GeV were detected. Three events stem from the HERA-I sample and have already been presented in [H103a], while two high-mass events were found in the 2004 data. It can be seen in the next section that both of them were observed in the $e\text{-}\mu\text{-}\mu$ -channel.

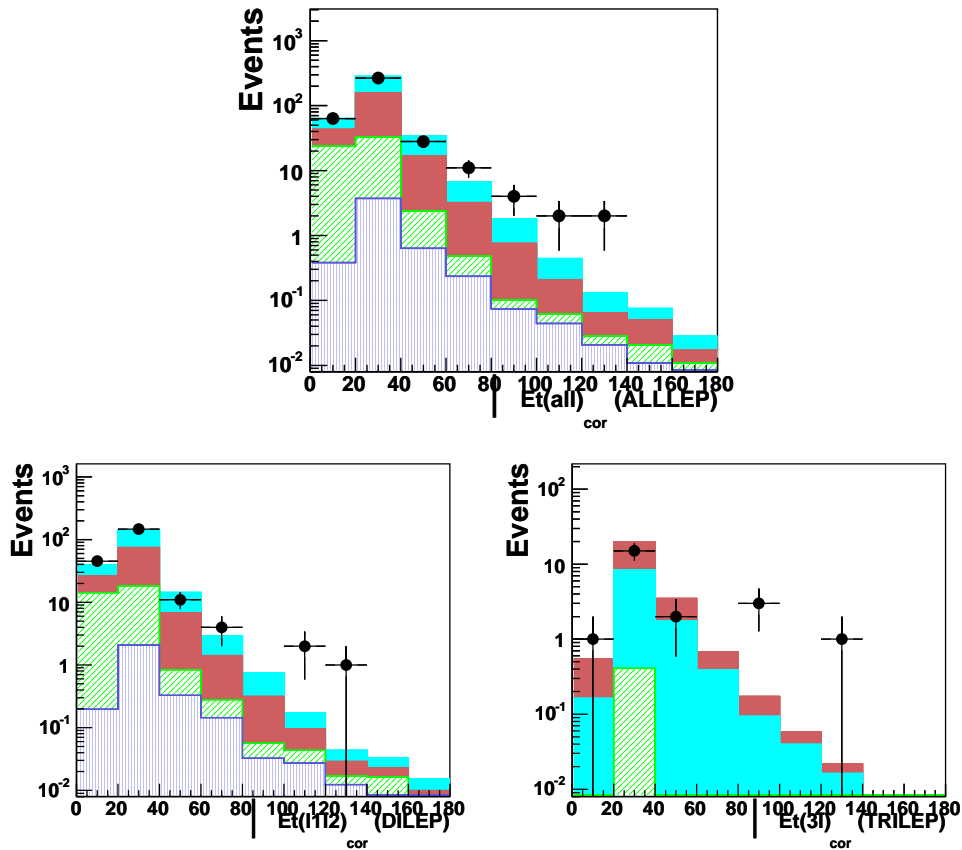


Figure 4.5: Distributions of the scalar sum of transverse energies of all leptons merging di- and tri-lepton classes (top). The plot covers the total 1994-2004 data sample. Bottom pictures: On the left, the $\sum E_T$ -distribution in the di-lepton class is shown for HERA-I data, on the right, the $\sum E_T$ -distribution in the tri-lepton class is displayed for HERA-II data.

The distributions of the scalar sum of transverse energies of all leptons $\sum E_T$ are presented for 1994-2004 data (HERA-I and -II) in figure 4.5 merging the $l\text{-}l\text{-}$ and the $l\text{-}l\text{-}l$ -classes.

The agreement between experiment and theory is satisfying. Nevertheless, a small deviation between data and MC at high energies is observed. Four events with $\sum E_T > 100$ GeV were recorded, three from HERA-I in the di-lepton channel ($e-e$, see bottom left), and one event from HERA-II in the tri-lepton channel ($e-\mu-\mu$, see bottom right). The Standard Model prediction for the range $\sum E_T > 100$ GeV is 0.69 ± 0.11 (see Chapter 4.5).

Table 4.3 summarises the number of events in all channels for the totality of the collected data sample from the years 1994-2004.

Selection	Data	SM	Pair Production (GRAPE)	DIS + Compton
$e-e$	156	160.6 ± 19.1	134.4 ± 10.9	26.2 ± 9.9
$\mu-\mu$	66	68.4 ± 9.7	68.4 ± 9.7	—
$e-\mu$	86	82.7 ± 9.3	49.4 ± 3.4	33.7 ± 7.3
$e-e-e$	26	32.5 ± 3.4	32.5 ± 3.4	0.02 ± 0.02
$e-\mu-\mu$	42	42.1 ± 5.2	42.1 ± 5.2	—

Table 4.3: Comparison between experiment and theory in the sub-classes of the multi-lepton analysis.

From left to right, the first column gives the name of the sub-channel, starting with the di-lepton channels. In the next two columns, the number of events in the data and the number of predicted events including the systematic errors, are presented. The SM prediction is then split up into the signal (expectation due to pair production) and the background (neutral current and QED Compton). The numbers show the good agreement between data and theoretical prediction. Within the error, data correspond to the Monte Carlo simulation. All sub-channels are dominated by the signal. While the $\mu-\mu$, $e-e-e$, and $e-\mu-\mu$ selection are quite “pure”, the proportion of background in the $e-\mu$ channel is at the order of 41%. This will be discussed in further detail in the next section.

4.3 Sub-Classes of Di-Lepton Channels HERA-I and -II

Starting with the di-lepton selection we will now focus on the single sub-channels.

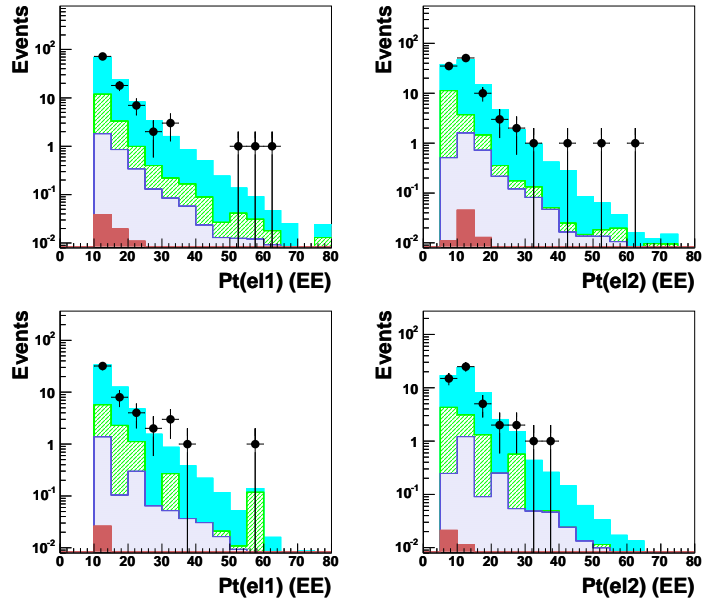


Figure 4.6: Distributions of transverse momenta in the di-electron channel for HERA-I (top) and HERA-II data (bottom).

4.3.1 e - e Channel

In figure 4.6 the transverse momenta of the two electrons in the e - e channel are displayed. The e - e channel is dominated by lepton pair production. For HERA-I and -II the signal fraction constitutes 83.4% (84% for HERA-I, and 82.1% for HERA-II), the remaining 16.6% concern background events due to a bad particle identification. They are split up in neutral current (13.4%) and QED Compton events (3.2%).

In the NC-case, pions, which disintegrate into a photon pair, or other jet components pretend an electron signature. In the Compton processes electrons are faked by radiated photons.

A good agreement between data and theory can be seen in the P_T distributions. 156 events were found in the data for 161 ± 25.3 predicted (HERA-I: Data: 105, MC: 107.2 ± 14.3 , HERA-II: Data: 51, MC: 53.9 ± 10.9). The three events in the high mass range from the Multi-Electron analysis [H103a] are represented in the HERA-I diagrams by the three electrons with a transverse momentum $P_{T_{e1}}$ between 50 and 65 GeV and a momentum $P_{T_{e12}}$ between 40 and 65 GeV.

Consistency between experimental results and theoretical prediction can also be observed in figure 4.7 for the θ distribution.

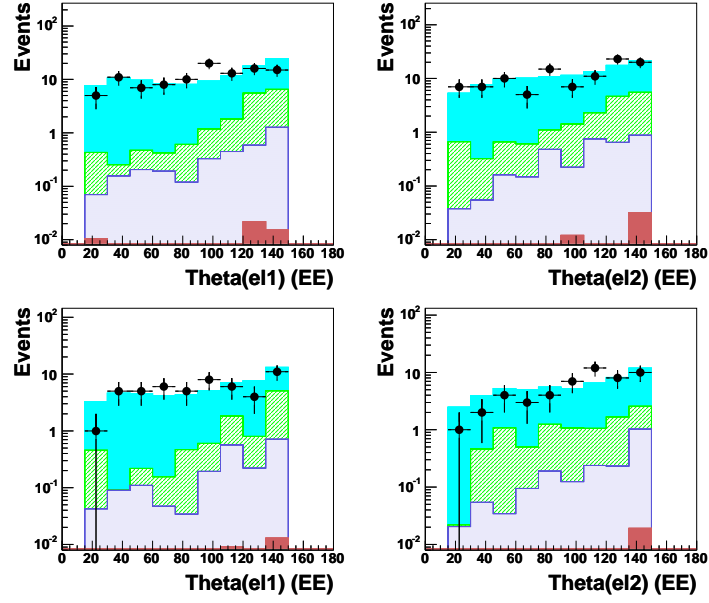


Figure 4.7: Polar angle distributions in the di-electron channel for HERA-I (top) and HERA-II data (bottom).

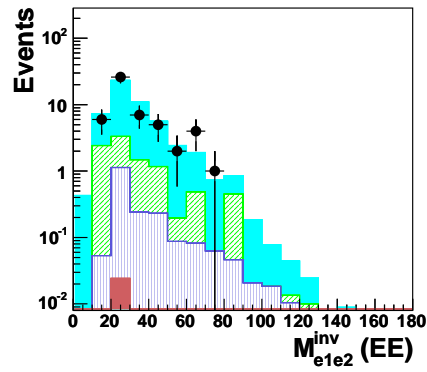


Figure 4.8: Distribution of the invariant mass M_{12} in the e - e channel for the HERA-II run.

Figure 4.8 shows the distribution of the invariant mass of the two electrons M_{12} for the HERA-II sample. The highest M_{12} -value found in data events is 75.86 GeV.

4.3.2 e - μ Channel

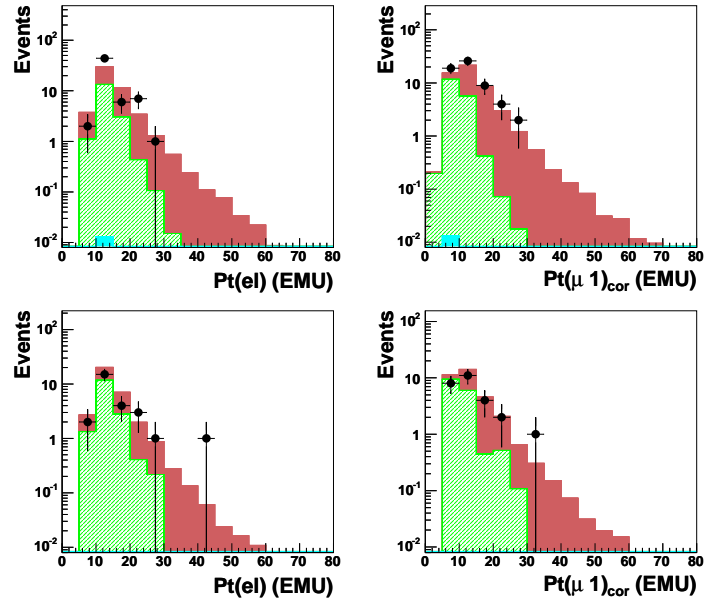


Figure 4.9: Distributions of transverse momenta in the e - μ channel for HERA-I (top) and HERA-II data (bottom).

Lepton pair production leads to e - μ signatures if the scattered electron is detected in the event and if one muon does not satisfy the kinematical criteria. Although the e - μ sub-channel is also dominated by the signal, the background fraction is higher than in the case of the di-electrons. 59% of the events in the simulation are produced in lepton pair production whereas 41% are neutral current events. In a hadronisation process, jets are produced, which contain pions or kaons. These could pretend muon signatures or could disintegrate into muons. The background is even higher in the HERA-II run (Pair production: 50.4%, NC-DIS: 49.6%) than in the HERA-I run (Pair production: 64.4%, NC-DIS: 35.6%). This could be explained by the matching requirement between cluster and track which has been relaxed for HERA-II (see Chapter 3.2.3)

With respect to the good consistency between data and Standard Model,

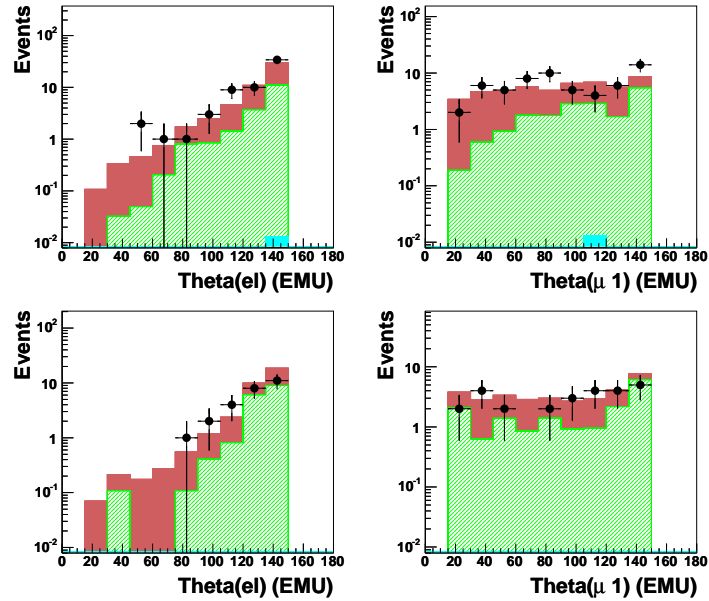


Figure 4.10: Polar angle distributions in the $e\text{-}\mu$ channel for HERA-I (top) and HERA-II data (bottom).

both background and signal seem to be simulated correctly. Nevertheless, it should be an objective to reduce the fraction of non-signal events furthermore.

Figure 4.9 shows the P_T distributions of the $e\text{-}\mu$ class. In the whole range data match the Monte Carlo prediction. It is obvious that a higher cut on P_T (or E_T) would eliminate most of the NC-background. In [Pee03] where a cut $E_T > 20$ GeV has been applied on the particles, its fraction is around 2%. However, this cut would also considerably decrease the acceptance for lepton pair production in the present analysis.

The highest transverse momentum in the $e\text{-}\mu$ selection was determined for an electron in the 2004 data. The value is $P_{T_{ele}} = 43.66$ GeV.

In figure 4.10 the distribution of the polar angle are displayed. Data are in good agreement with the Monte Carlo.

4.3.3 $\mu\text{-}\mu$ Channel

Since the final topologies for NC-DIS and QED Compton are typically $e\text{-}j$, and $e\text{-}\gamma$ or $e\text{-}j\text{-}\gamma$, respectively, the di-muon channel is not influenced by this kind of background. The main background source in the $\mu\text{-}\mu$ selection are

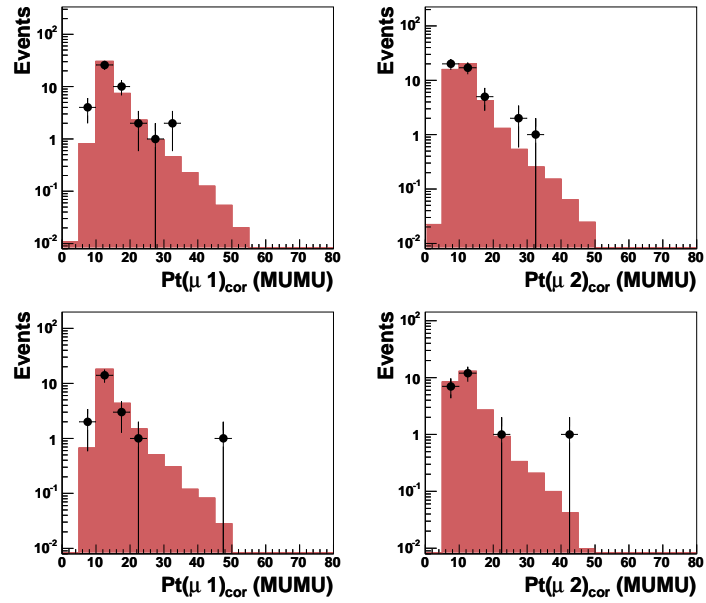


Figure 4.11: Distributions of transverse momenta in the di-muon channel for HERA-I (top) and HERA-II data (bottom).

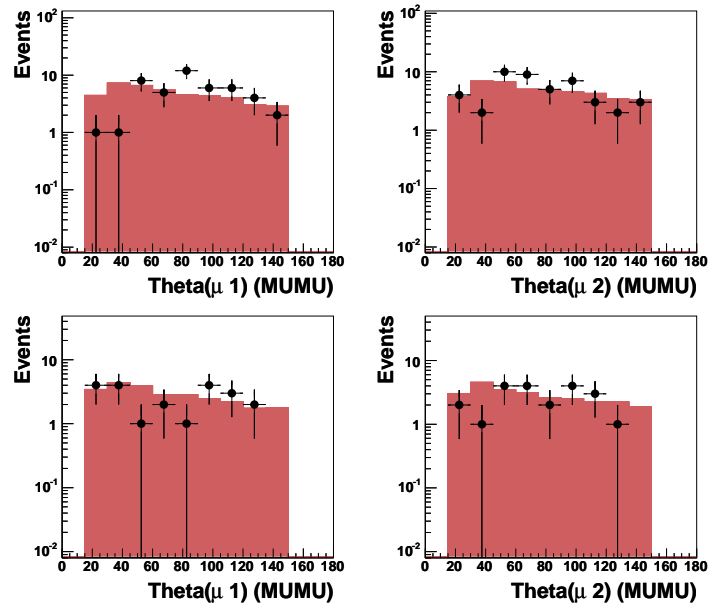


Figure 4.12: Polar angle distributions in the di-muon channel for HERA-I (top) and HERA-II data (bottom).

the non ep events due to cosmic muons. Special cuts were made to eliminate them as described in section 4.1.2. In addition, all events were scanned in order to recognise remaining cosmics in the sample. 7 events (roughly 10% of 73 events) were identified as cosmics and excluded from the sample. After the visualisation, 66 di-muon events are found in the data, which are in good agreement with the SM prediction of 68.4 ± 11.9 events. This is shown in figure 4.11 and figure 4.12.

The $\mu\text{-}\mu$ event with the highest invariant mass stems from the HERA-II period. The transverse momenta of the muons are $P_{T_{\mu 1}} = 46.54$ GeV and $P_{T_{\mu 2}} = 40.97$ GeV, the invariant mass and the sum of transverse energies is evaluated to $M_{12} = 87.35$ GeV and $\sum E_T = 87.51$ GeV.

4.4 Sub-Classes of Tri-Lepton Channels HERA-I and -II

This category is formed by the sub-channels $e\text{-}e\text{-}e$ and $e\text{-}\mu\text{-}\mu$. Lepton pair production gives rise to these signatures if an electron or muon pair is produced and if the scattered electron is also reconstructed in the detector. We will begin the description with the tri-electron channel.

4.4.1 $e\text{-}e\text{-}e$ Channel

The background in the $e\text{-}e\text{-}e$ selection, induced by neutral current processes for HERA-I and -II, is less than 0.05%. Since only 26 events were detected in the data, statistics in the $e\text{-}e\text{-}e$ sample is worse than in the other sub-channels. Nevertheless, data match the Monte Carlo simulation within the errors. The agreement can be seen in figure 4.13 and in figure 4.14 where the transverse momenta of the electrons and their polar angles are presented.

As the distribution of the longitudinal momentum $E - P_Z$ for HERA-I has already been presented in [H103a], here only the plot for the 2004 data is shown. The distribution of figure 4.16 verifies an accumulation of the events at values around 55 GeV.

As in the di-electron channel before, there is a slight excess of data in comparison to the theory at high P_T (HERA-I). The common feature of the three high-mass events is one high energetic electron detected under a small polar angle θ .

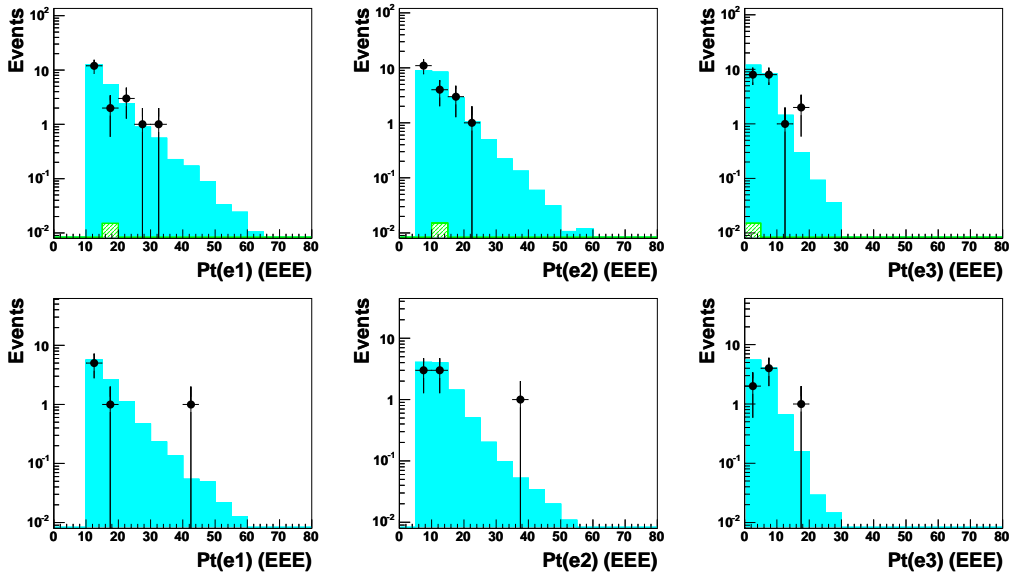


Figure 4.13: Distributions of transverse momenta in the tri-electron channel for HERA-I (top) and HERA-II data (bottom).

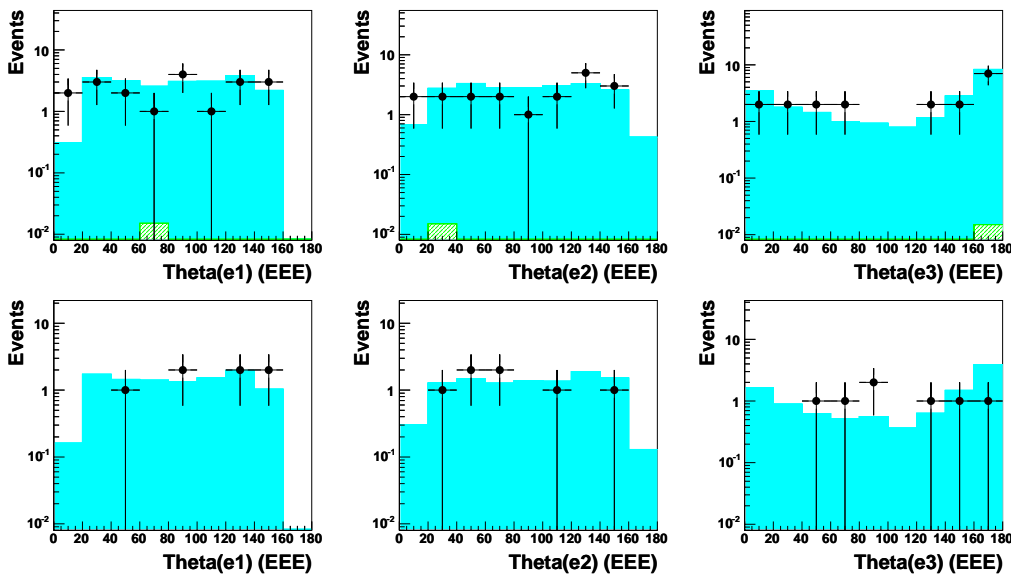


Figure 4.14: Polar angle distributions in the tri-electron channel for HERA-I (top) and HERA-II data (bottom).

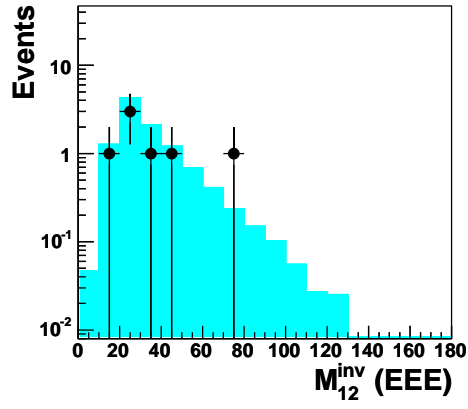


Figure 4.15: Distribution of the invariant mass M_{12} in the e - e - e channel for 2004 data.

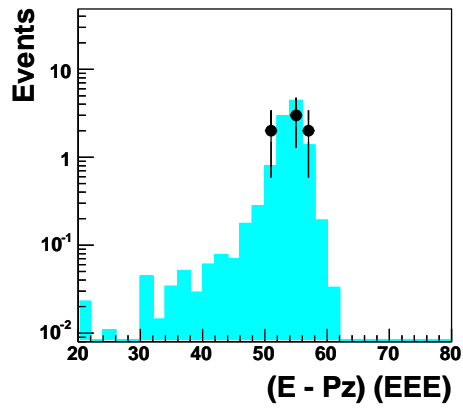


Figure 4.16: Distribution of the longitudinal momentum $E - P_z$ in the e - e - e channel for 2004 data.

The mass distribution for HERA-II is shown in figure 4.15. The largest invariant mass was observed in Run 384390, Event 32486 evaluated to $M_{12} = 79.74$ GeV. The transverse momenta of the two highest P_T -electrons were determined to $P_{T_{e_1}} = 42.04$ GeV and $P_{T_{e_2}} = 39.65$ GeV.

4.4.2 e - μ - μ Channel

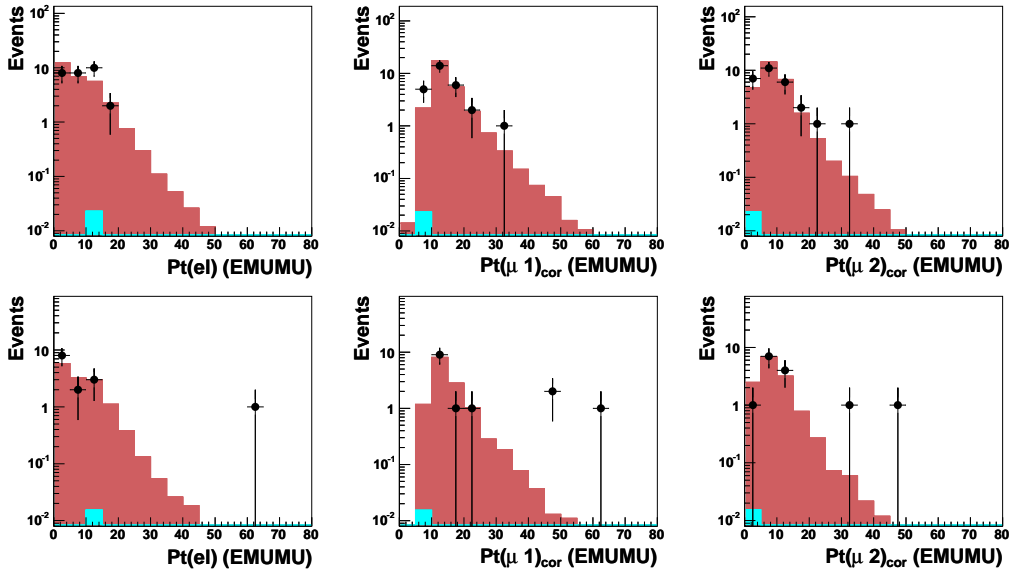


Figure 4.17: Distributions of transverse momenta in the e - μ - μ channel for HERA-I (top) and HERA-II data (bottom).

Figure 4.17 shows the P_T control plots in the e - μ - μ channel. The general agreement between data and MC (42 events in the data for 42.0 ± 5.8 predicted) is good. HERA-I data correspond to the simulation in the whole range while HERA-II data exceed the prediction in regions of higher transverse momenta. Two events with an invariant mass $M_{12} > 100$ GeV were detected:

- **R 367354, E 22364:**
 - $P_{T_{\mu 1}} = 62.27$ GeV, $P_{T_{e_1}} = 64.00$ GeV
 - $M_{12}^{e\mu} = 128.89$ GeV, $\sum E_T = 126.25$ GeV

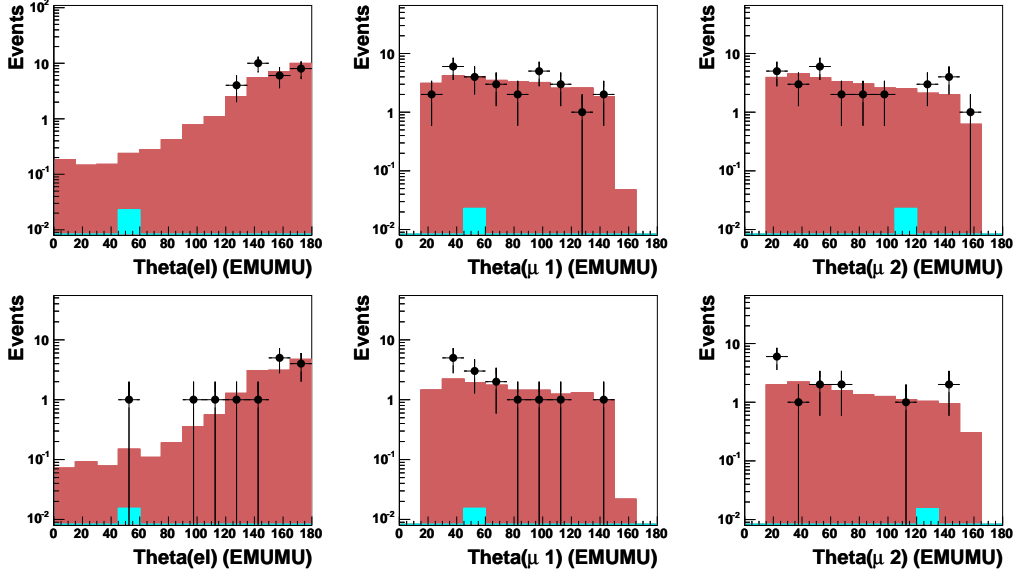


Figure 4.18: Polar angle distributions in the $e\text{-}\mu\text{-}\mu$ channel for HERA-I (top) and HERA-II data (bottom).

- **R 383168, E 78379:**

- $P_{T\mu_1} = 48.76$ GeV, $P_{T\mu_2} = 45.90$ GeV
- $M_{12}^{\mu\mu} = 102.09$ GeV, $\sum E_T = 94.66$ GeV

Additionally, one further event with an invariant mass $M_{12}^{\mu\mu} = 83.69$ GeV was found. The two muons are the highest- P_T particles in the event with values at $P_{T\mu_1} = 46.59$ GeV and $P_{T\mu_2} = 34.48$ GeV.

The θ distributions are presented in figure 4.18 showing a good agreement between experiment and theory. It is obvious that the scattered electron is mainly observed in the backward region.

4.4.3 Radiative Events

$e\text{-}e\text{-}\mu$ Event

In the 1994-2000 data one event with a $e\text{-}e\text{-}\mu$ signature was found for 0.92 ± 0.56 predicted events. It is presented in figure 4.19.

Besides the muon ($P_T^\mu = 13.82$ GeV), two electrons with $P_T^{e1} = 13.64$ GeV and $P_T^{e2} = 1.30$ GeV were detected. The second electron was emitted under

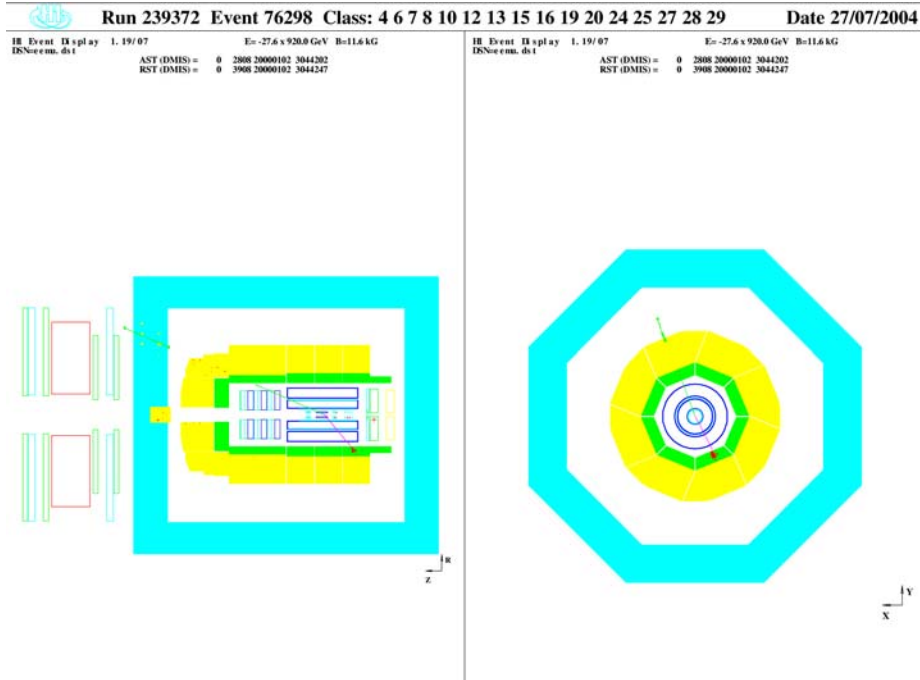


Figure 4.19: Display of an e - e - μ event detected in the 1994-2000 data.

a large polar angle of $\theta_{e2} = 173.87^\circ$. The invariant mass is calculated to $M_{12} = 48.04$ GeV. It can be assumed that the second electron is either a photon which has produced an electromagnetic cluster in the SpaCal, or an electron generated by photon conversion. In both cases the event may be interpreted as e - μ -event with a radiated photon.

4-Lepton Event

Additionally, one four-lepton event was observed in HERA-II data for a theoretical prediction of 0.56 ± 0.14 events. The event display (figure 4.20) shows three electrons with transverse momenta between 6 and 12 GeV in the central part of the detector, and one electromagnetic cluster in the very backward region ($P_T = 1.06$ GeV, $\theta = 170.73^\circ$). As in the case of the e - e - μ event, the SpaCal cluster can be attributed to a photon or a photon, which converted into an electron.

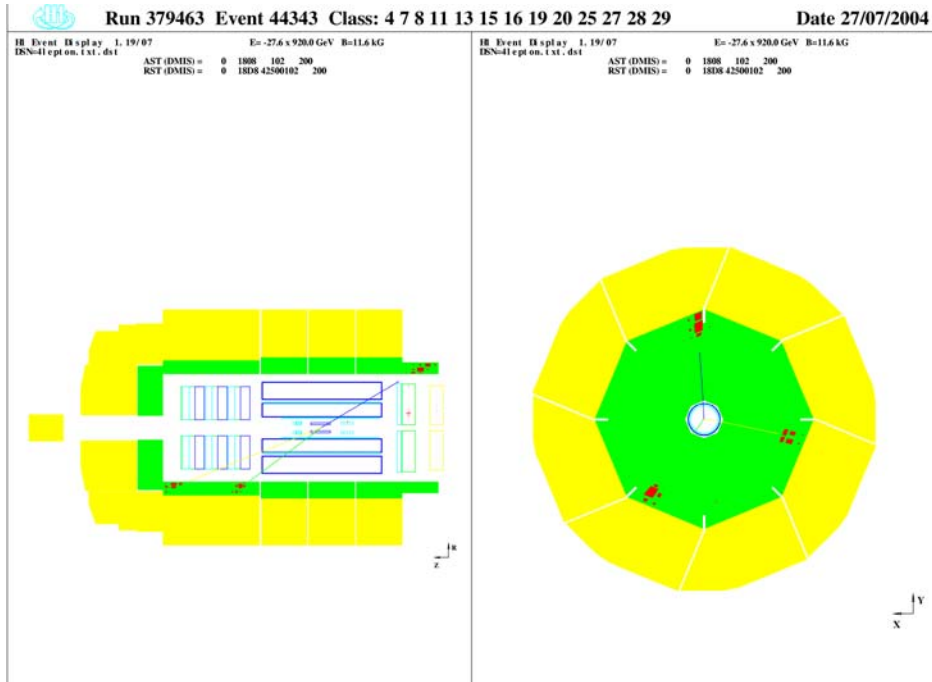


Figure 4.20: Display of an 4-lepton event detected in the 1994-2000 data.

4.5 Events in the High Mass Range

This section is summarising the events which have been found in the high-mass or high-energy region. In table 4.4 the eight events with an invariant mass $M_{12} > 100$ GeV are compared to the Standard Model prediction for this range. The comparison shows a deviation of data with respect to the Monte Carlo simulation. Nevertheless, statistics are too low to permit profound conclusions about a possible excess.

An overview of the high- $\sum E_T$ events for di-, tri and all leptons is given in table 4.5.

In the following section we will focus on the two high-mass events selected in the HERA-II data. A method will be presented to improve the resolution on the event parameters and subsequently on the derived quantities, such as the invariant mass M_{12} .

Selection	Data	SM	Signal	Background
$e-e M_{ee} > 100 \text{ GeV}$	3	0.51 ± 0.04	0.33 ± 0.03	0.18 ± 0.03
$\mu-\mu M_{\mu\mu} > 100 \text{ GeV}$	0	0.04 ± 0.01	0.04 ± 0.01	—
$e-\mu M_{e\mu} > 100 \text{ GeV}$	0	0.31 ± 0.03	0.31 ± 0.03	—
$e-e-e M_{ee} > 100 \text{ GeV}$	3	0.38 ± 0.04	0.38 ± 0.04	—
$e-\mu-\mu M_{e\mu} > 100 \text{ GeV}$	1	0.04 ± 0.01	0.04 ± 0.01	—
$e-\mu-\mu M_{\mu\mu} > 100 \text{ GeV}$	1	0.02 ± 0.01	0.02 ± 0.01	—

Table 4.4: Comparison between data and theory in the high mass range $M_{12} > 100 \text{ GeV}$.

Selection	Data	SM	Signal	Background
$l-l \sum E_T > 100 \text{ GeV}$	3	0.42 ± 0.04	0.29 ± 0.03	0.13 ± 0.02
$l-l-l \sum E_T > 100 \text{ GeV}$	1	0.11 ± 0.02	0.11 ± 0.02	—
ALL LEP $\sum E_T > 100 \text{ GeV}$	4	0.69 ± 0.11	0.57 ± 0.05	0.13 ± 0.03

Table 4.5: Summary of the events with $\sum E_T > 100 \text{ GeV}$ in the di- and tri-lepton channel and for all leptons in comparison to the SM prediction.

Chapter 5

Kinematical Fit for High Mass Events

5.1 Motivation

Chapter (4.1.3) highlights the fact that transverse momenta of muons could be determined incorrectly in the high P_T range where the track curvature is small. In the method presented, the transverse momentum of the muon with the highest error dP_T is corrected in such a way that the momenta of all the particles become balanced. ($P_T^{miss} = 0$).

There is, however, a problem with this method with errors on P_T of two muons that are large because only the P_T of one particle is corrected. Thus, we are trying in this chapter a more sophisticated technique, a constrained fit.

We are going to give evidence of the fit being based on the requirement of conserved transverse and longitudinal momentum of the event. The fit is applied to the four-vectors of the particles in the detector.

The kinematical fit on high mass events is mainly motivated by two reasons. On the one hand it puts us into a position to improve kinematic measurements, e.g. the resolution on transverse momenta, energies and quantities which can be derived from the former ones like the invariant mass M_{12} . On the other hand we can study if or how the invariant masses are shifted by the fit, and if the final results are compatible with the interpretation that the high-mass lepton pairs stem from the decay of a single resonance.

A constrained fit has already been applied to the high-mass events found in the HERA-I data and published [H103a]. Figure 5.1 shows the three $e-e$ and three $e-e-e$ events. The results are summarised and presented in figure 5.2.

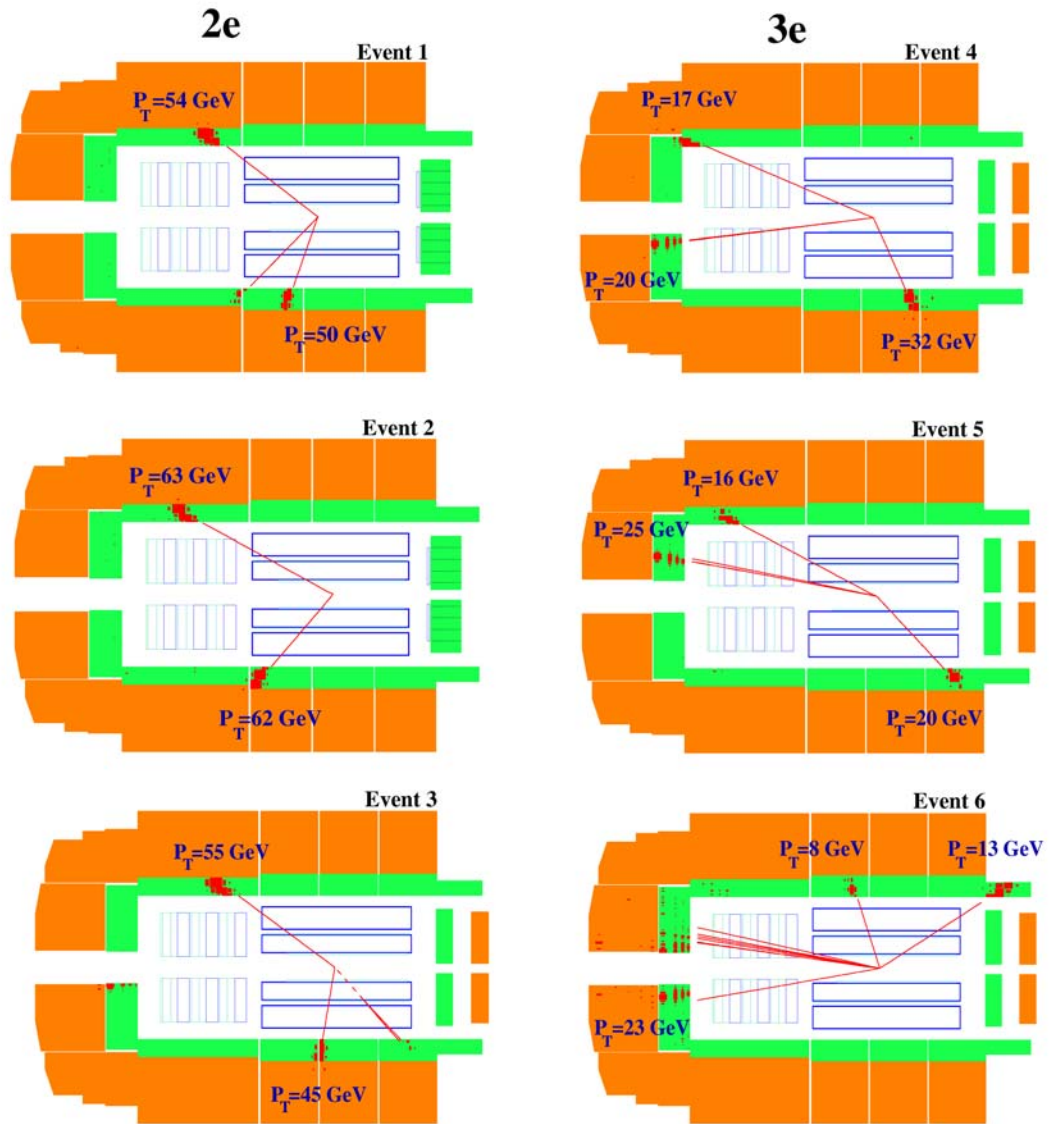


Figure 5.1: High-mass events from HERA-I, labeled as di-electron (left) and tri-electron events (right). Event 1 and 3 have an additional low-energetic electron while 6 contains a hadronic part [H103a].

Particle	E [GeV]	θ [degrees]	ϕ [degrees]	Charge (significance)
Multi-electron Event 1 (2e)				
Run 83507	$E - P_z = 54.0 \pm 1.1$ GeV		$P_T^{miss} = 3.1 \pm 1.8$ GeV	
Event 16817	$M_{12} = 111.2 \pm 2.4$ GeV		$M_{12}^{fit} = 111.3 \pm 0.4$ GeV	
e_1	90.3 ± 3.1	36.6 ± 0.2	98.48 ± 0.05	- (4σ)
e_2	53.6 ± 1.4	69.6 ± 0.3	-77.05 ± 0.05	undetermined
low energy e	4.4 ± 0.3	44.3 ± 0.3	-155.46 ± 0.03	+ (70σ)
Multi-electron Event 2 (2e)				
Run 89256	$E - P_z = 43.9 \pm 0.8$ GeV		$P_T^{miss} = 1.9 \pm 1.8$ GeV	
Event 224212	$M_{12} = 130.0 \pm 2.6$ GeV		$M_{12}^{fit} = 129.3 \pm 2.4$ GeV	
e_1	132.4 ± 4.3	28.6 ± 0.1	8.73 ± 0.06	undetermined
e_2	82.4 ± 1.8	48.4 ± 0.2	-171.50 ± 0.03	- (6σ)
Multi-electron Event 3 (2e)				
Run 254959	$E - P_z = 57.3 \pm 1.4$ GeV		$P_T^{miss} = 3.5 \pm 2.0$ GeV	
Event 17892	$M_{12} = 112.5 \pm 2.4$ GeV		$M_{12}^{fit} = 109.5 \pm 1.0$ GeV	
e_1	96.9 ± 3.3	34.6 ± 0.3	52.66 ± 0.02	+ (10σ)
e_2	46.1 ± 1.1	80.1 ± 0.9	-125.62 ± 0.01	+ (15σ)
fwd em cluster	70_{-2}^{+100} ^a	4.5 ± 0.1	-132.7 ± 1.0	undetermined
photon	1.1 ± 0.1	132.0 ± 5.5	39.8 ± 7.3	0
^a this error includes the uncertainty due to energy loss in the beampipe				
Multi-electron Event 4 (3e)				
Run 168058	$E - P_z = 55.7 \pm 1.4$ GeV		$P_T^{miss} = 1.1 \pm 0.8$ GeV	
Event 42123	$M_{12} = 137.4 \pm 2.9$ GeV		$M_{12}^{fit} = 138.8 \pm 1.2$ GeV	
e_1	35.8 ± 0.9	115.6 ± 0.9	-5.98 ± 0.02	+ (18σ)
e_2	173.0 ± 5.5	6.6 ± 0.1	-159.1 ± 0.5	undetermined
e_3	44.8 ± 1.7	21.8 ± 0.2	139.10 ± 0.03	- (12σ)
Multi-electron Event 5 (3e)				
Run 192864	$E - P_z = 53.8 \pm 1.4$ GeV		$P_T^{miss} = 0.7 \pm 0.6$ GeV	
Event 123614	$M_{12} = 118.1 \pm 2.6$ GeV		$M_{12}^{fit} = 121.9 \pm 0.6$ GeV	
e_1	138.9 ± 4.5	10.2 ± 0.1	44.1 ± 0.6	undetermined
e_2	28.1 ± 0.8	134.7 ± 0.3	-95.85 ± 0.01	+ (25σ)
e_3	35.3 ± 1.5	26.6 ± 0.1	172.71 ± 0.05	+ (5σ)
Multi-electron Event 6 (3e)				
Run 267312	$E - P_z = 57.4 \pm 1.6$ GeV		$P_T^{miss} = 2.4 \pm 0.8$ GeV	
Event 203075	$M_{12} = 134.7 \pm 3.1$ GeV		$M_{12}^{fit} = 132.3 \pm 1.4$ GeV	
e_1	186.0 ± 5.9	7.11 ± 0.05	-71.3 ± 0.4	undetermined
e_2	25.5 ± 0.8	148.8 ± 0.2	120.25 ± 0.02	+ (32σ)
e_3	8.5 ± 0.5	69.7 ± 0.3	164.90 ± 0.01	+ (57σ)
hadrons ^b	123.2 ± 6.7	6.1 ± 1.1	53.5 ± 1.1	
^b mass of the visible hadronic system: 24.0 ± 2.5 GeV				

Figure 5.2: Results of the kinematical fit for the HERA-I events with $M > 100$ GeV. From the figure initial M_{12} and reconstructed invariant masses M_{12}^{fit} can be compared [H103a].

Figure 5.2 demonstrates that the shift between initial and final invariant masses is in the order of 1-3 GeV. While the initial relative errors on M_{12} have been calculated to values of roughly 2-2.5%, the resolution has been improved by the fit to values of dM_{12} between 0.5 and 1%.

In order to check the high-mass events carefully and to improve the P_T -balance method, the kinematical fit has been applied to the two $e\text{-}\mu\text{-}\mu$ events with $M_{12} > 100$ GeV found in the 2004 data. Due to their completely different signature in the detector, the fit procedure had to be modified for muons. The fitting of electrons and muons will be discussed in detail in the following. First, we will introduce the programme “APLCON”, which the fit makes use of. It has been developed by V. Blobel [Blo97].

5.2 Description of the Fit Programme APLCON

As already mentioned, the kinematical fit is a constrained fit imposing longitudinal and transverse momentum conservation to adjust a finite number of particle observables.

The kinematical fit is based on three hypotheses which can be deduced easily by looking at the 4-vectors of the incident particles:

- Lepton (Electron/Positron): $(E_e, 0, 0, -E_e)$
- Proton $(E_p, 0, 0, E_p)$

As the initial transverse momentum $P_T = \sqrt{P_x^2 + P_y^2}$ is zero, it has to be zero in the final state due to momentum conservation if all particles of the event have been measured.

From the 1- and 4-component of the momentum-vector, we calculate the conserved quantity $E - P_z$:

$$E - P_z = E_e + E_p - E_p + E_e = 2E_e$$

with an electron/positron energy of $E_e = 27.5$ GeV.

Finally, we can summarise the three constraints deduced above:

$$P_x = 0 \tag{5.1}$$

$$P_y = 0 \tag{5.2}$$

$$E - P_z = 55 \text{ GeV} \tag{5.3}$$

Following the notation of [Blo97], we write the measured parameters as vector \mathbf{x} with n components x_1, x_2, \dots, x_n , and its covariance matrix as \mathbf{V}_x :

$$\mathbf{x} = \begin{pmatrix} x_1 \\ x_2 \\ \dots \\ \dots \\ x_n \end{pmatrix} \quad \mathbf{V}_x = \begin{pmatrix} \sigma_{11} & \sigma_{12} & \dots & \sigma_{1n} \\ \sigma_{21} & \sigma_{22} & \dots & \sigma_{2n} \\ \dots & \dots & \dots & \dots \\ \dots & \dots & \dots & \dots \\ \sigma_{n1} & \sigma_{n2} & \dots & \sigma_{nn} \end{pmatrix} \quad (5.4)$$

The diagonal elements can be identified with the standard deviations of the parameters, e.g. $\sigma_{11} = \sigma_1^2$ is the standard deviation of the vector component x_1 . The covariance matrix is symmetric, i.e. $\mathbf{V}_x^T = \mathbf{V}_x$ and $\sigma_{ij} = \sigma_{ji}$, respectively.

For the kinematical fit the derivative matrix of m quantities with respect to the n components x_i is needed. This matrix is called \mathbf{A} , and is given by

$$\mathbf{A} = \begin{pmatrix} A_{11} & A_{12} & \dots & A_{1n} \\ A_{21} & A_{22} & \dots & A_{2n} \\ \dots & \dots & \dots & \dots \\ \dots & \dots & \dots & \dots \\ A_{n1} & A_{n2} & \dots & A_{nn} \end{pmatrix} = \begin{pmatrix} \partial y_1 / \partial x_1 & \partial y_1 / \partial x_2 & \dots & \partial y_1 / \partial x_n \\ \partial y_2 / \partial x_1 & \partial y_2 / \partial x_2 & \dots & \partial y_2 / \partial x_n \\ \dots & \dots & \dots & \dots \\ \dots & \dots & \dots & \dots \\ \partial y_m / \partial x_1 & \partial y_m / \partial x_2 & \dots & \partial y_m / \partial x_n \end{pmatrix}. \quad (5.5)$$

The vector \mathbf{y} is set up by the m parameters.

The principle the programme APLCON relies on is called “the Principle of Constrained Least Squares”. It uses the Lagrange Multiplier Method. In the ideal case, the parameters \mathbf{x} satisfy one or more constraint equations f :

$$f(\mathbf{x}) = 0 \quad (5.6)$$

Unlike the mathematical idealisation, we generally have to correct the measured values, marked by \mathbf{x}_0 , by a vector $\Delta\mathbf{x}$ to fulfil the conditions:

$$f(\mathbf{x}_0 + \Delta\mathbf{x}) = 0 \quad (5.7)$$

The search for the corrections Δx , which are meant to conform to

$$\Delta\mathbf{x}^T \mathbf{V}_x^{-1} \Delta\mathbf{x} = \text{minimum} \quad (5.8)$$

is realised by the method of Lagrangian multipliers. To each constraint equation f a parameter λ is added. For the function obtained

$$L(\Delta\mathbf{x}, \lambda) = \Delta\mathbf{x}^T \mathbf{V}_x^{-1} \Delta\mathbf{x} + 2\lambda^T f(\mathbf{x}_0 + \Delta\mathbf{x}) \quad (5.9)$$

a stationary point need to be determined by demanding that the derivatives of L with respect to all $\Delta \mathbf{x}_i$ and to all λ_j disappear.

If the conditions $f(\mathbf{x}_0 + \Delta \mathbf{x}) = 0$ are non-linear, they have to be linearised. For these purposes, equation (5.7) has to be expressed in terms of the correction $\Delta \mathbf{x}$:

$$\begin{aligned} f(\mathbf{x}_0 + \Delta \mathbf{x}^* + (\Delta \mathbf{x} - \Delta \mathbf{x}^*)) &= 0 \\ f|_{\mathbf{x}_0 + \Delta \mathbf{x}^*} + (\Delta \mathbf{x} - \Delta \mathbf{x}^*) \left. \frac{\partial f}{\partial \mathbf{x}} \right|_{\mathbf{x}_0 + \Delta \mathbf{x}^*} &= 0 \\ \left(\frac{\partial f^*}{\partial \mathbf{x}} \right) \Delta \mathbf{x} &= \left(\frac{\partial f^*}{\partial \mathbf{x}} \right) \Delta \mathbf{x}^* - f^* \end{aligned} \quad (5.10)$$

The problem is solved in an iterative way, using the quantity $\Delta \mathbf{x}^*$ which denotes the previous correction. f^* and the derivative $\partial f^*/\partial \mathbf{x}$ are calculated at the point $\mathbf{x}_0 + \Delta \mathbf{x}^*$.

Equation (5.10) can be written in a more suggestive way:

$$\mathbf{f} + \mathbf{A}(\Delta \mathbf{x} - \Delta \mathbf{x}^*) = 0 \quad (5.11)$$

with the shortcuts

$$\mathbf{f} = \begin{pmatrix} f_1(\mathbf{y}^*) \\ f_2(\mathbf{y}^*) \\ \dots \\ \dots \\ f_m(\mathbf{y}^*) \end{pmatrix} \quad \mathbf{A} = \begin{pmatrix} \partial f_1/\partial x_1 & \partial f_1/\partial x_2 & \dots & \partial f_1/\partial x_n \\ \partial f_2/\partial x_1 & \partial f_2/\partial x_2 & \dots & \partial f_2/\partial x_n \\ \dots & \dots & \dots & \dots \\ \dots & \dots & \dots & \dots \\ \partial f_m/\partial x_1 & \partial f_m/\partial x_2 & \dots & \partial f_m/\partial x_n \end{pmatrix} \quad (5.12)$$

corresponding to the definition of \mathbf{A} in (5.5).

Now a stationary point of the function

$$L = \Delta \mathbf{x}^T \mathbf{W} \Delta \mathbf{x} + 2\lambda^T (\mathbf{f} + \mathbf{A}(\Delta \mathbf{x} - \Delta \mathbf{x}^*)) \quad (5.13)$$

need to be found by differentiation. In (5.13) \mathbf{W} is equivalent to the inverse covariance matrix, \mathbf{V}_x^{-1} , and is known as the weight matrix.

The differentiation with respect to all $\Delta \mathbf{x}$ leads to

$$\mathbf{W} \Delta \mathbf{x} + \mathbf{A}^T \lambda = 0, \quad (5.14)$$

and the derivatives with respect to the Lagrangian multipliers λ are given by

$$\mathbf{A} \Delta \mathbf{x} = -\mathbf{f} + \Delta \mathbf{x}^*. \quad (5.15)$$

Thus the equation system can be written as

$$\begin{pmatrix} \mathbf{W} & \mathbf{A}^T \\ \mathbf{A} & 0 \end{pmatrix} \begin{pmatrix} \Delta \mathbf{x} \\ \lambda \end{pmatrix} = \begin{pmatrix} 0 \\ -\mathbf{f} + \Delta \mathbf{x}^* \end{pmatrix}. \quad (5.16)$$

The programme APLCON evaluates (5.16) by matrix inversion. In the case of non-linear problems, the iteration stops when convergence is reached. This can be written mathematically by

$$\sum_m |f_m(\mathbf{x}_0 + \Delta \mathbf{x})| < \epsilon, \quad (5.17)$$

where the explicit size of ϵ has to be defined by the user. After the final iteration, the minimised quantity

$$S = \Delta \mathbf{x}^T \mathbf{V}_x^{-1} \Delta \mathbf{x} \quad (5.18)$$

should follow a χ^2 -distribution with ν degrees of freedom, where ν is equal to m , the number of constraint equations. Further details can be found in the next section and in [Blo97] and [Blo02].

5.2.1 Quality of the Kinematical Fit

The quality of a fit can be checked by a χ^2 -test. For n variables x_i , which follow a normal-distribution around the mean μ_i and have the variance σ_i^2 , χ^2 can be defined as:

$$\chi^2 = \frac{(x_1 - \mu_1)^2}{\sigma_1^2} + \frac{(x_2 - \mu_2)^2}{\sigma_2^2} + \dots + \frac{(x_n - \mu_n)^2}{\sigma_n^2} = \sum_{i=1}^n \frac{(x_i - \mu_i)^2}{\sigma_i^2} \quad (5.19)$$

If the variances of the n quantities have been obtained independently for each x_i , the number of degrees of freedom ν is equivalent to the number of measured variables n .

To test if the values of μ_i and σ_i^2 are correct, χ^2 can be compared to the number of degrees of freedom ν . A good quality is accomplished if the χ^2 is approximately equal to ν . For non-correlated parameters, the number of degrees of freedom is equivalent to the number of parameters. For correlated quantities, the number of degrees of freedom ν is reduced by the number of relations r between the x_i :

$$\nu = n - r \quad (5.20)$$

If $\chi^2 > \nu$, the variances (errors squared) have been under-estimated. The inverse case, $\chi^2 < \nu$, results from over-estimated errors [Sco00].

5.3 Choice of Parameters

The quality of the kinematical fit is intimately connected to the choice of fit parameters which have to meet the requirements as follows:

- Parameters have to be independent of each other
- Precise measurement for the chosen parameters ought to be possible
- Corresponding errors have to be estimated properly

These conditions will require different strategies to fit electrons and muons.

5.3.1 Fitting Electrons

A possible set of independent parameters for electrons is represented by the Cartesian coordinates of the electron cluster barycenter in the LAr Calorimeter or the SpaCal, by the energy E_{calo} deposited in the calorimeter and by the z-component of the event vertex z_V . Since the azimuthal angle ϕ is measured with high accuracy by the tracking system, we decided to transform the Cartesian coordinates of the cluster to cylindrical coordinates $(x, y, z)_C \longrightarrow (R, \phi, z)_C$. The choice of cylindrical coordinates also corresponds to the detector geometry. The cluster is corrected by the vertex position. As mentioned above, ϕ_C is subsequently replaced by ϕ_{tr} if the electron is found in the central part of the detector.

Errors on the cylindrical cluster coordinates can be re-calculated from the errors on Cartesian coordinates of the cluster barycenter. An exception is made for the angle ϕ where the error is determined by the trackers. The error on the energy is given by the resolution of the calorimeter $\frac{0.15 \cdot E}{\sqrt{E}}$ [H197] and by the error on the calorimetric calibration, which varies as a function of θ between values of 0.7 and 3%. [Hei99]

The set of parameters chosen to fit electrons is summarised in table 5.1.

Vector x of the fit parameters:	
Cylindrical cluster coordinates (exception: ϕ_C replaced by ϕ_{tr})	$(R_C, \phi_{tr}, z_C)_{e_i}$
Calorimetric energy	E_{C_i}
z-Component of the event vertex	z_V
Diagonal elements of the error matrix V_x:	
Error on barycenter of clusters (error on the energy and the volume of the cells)	$dx_C, dy_C, dz_C \longrightarrow dR_C, dz_C$
Error on ϕ_{tr} found out by trackers	$d\phi_{tr}$
Error on the energy	$dE_C = 15\% / \sqrt{E} + (0.7 \oplus 3\%)_{sys.}^{calib.}$
Error on z-vertex	dz_V

Table 5.1: Input quantities for the kinematical fit for electrons.

5.3.2 Fitting Muons

The muon signature in the detector is made up of an inner track in the inner tracking system and an outer track in the Muon Detector. Unlike electrons, where the measurement of energy, of polar and of azimuthal angles is done in the calorimeter, the kinematic observables of a muon are measured by the trackers. Therefore, the fit input for muons has to be chosen differently from the input for electrons.

The track of a charged particle is characterised by its curvature, which is used to determine the transverse momentum P_T by

$$P_T = \frac{0.3 \cdot q \cdot B[T]}{\kappa[cm]}, \quad (5.21)$$

where B is the magnetic field, and q the particle charge.

The inverse transverse momentum P_T^{-1} is directly proportional to the measured curvature: $P_T^{-1} \propto \kappa$. Determined by the curvature of the tracks, only the errors on the inverse momentum guarantee to be symmetric. Therefore, P_T^{-1} is a valid fit parameter in the case of muons.

However, we have observed that the errors dP_T and dP_T^{-1} can be overestimated if the curvature is small, i.e. in the case of high momenta. We made

a check with a 1999-2000 MC-GRAPE sample to verify the credibility of the indicated errors. The selection corresponds to the di-muon channel of the multi-lepton analysis, only the cuts on P_T were relaxed to investigate also the low- P_T -range. Thus the criteria are:

- $P_T^{\mu 1} > 2\text{GeV}$, $P_T^{\mu 2} > 2\text{GeV}$
- other criteria from the multi-lepton analysis

For the error-check the difference between the inverse momenta of reconstructed and generated particles was calculated:

$$\Delta P_T^{-1} = \frac{1}{P_T^{rec}} - \frac{1}{P_T^{gen}} \quad (5.22)$$

This quantity was plotted for several bins in P_T . For each bin the distribution was fitted by a Gaussian, and the σ of the fit was determined. Then the quantity

$$dP_T^{-1}(rec - gen)_{rel} = \frac{\sigma_i}{1/ \langle P_T \rangle_i} \quad (5.23)$$

was evaluated.

$dP_T^{-1}(rec - gen)$ was compared to the error on the inverse momentum provided by the track reconstruction $dpti_{tr}$. The latter quantity was plotted for the same P_T -intervals as above. Then the mean value obtained for each bin i was divided by $1/ \langle P_T \rangle_i$

$$dP_T^{-1}(trackers)_{rel} = \frac{\langle dpti_{tr} \rangle}{1/ \langle P_T \rangle_i} \quad (5.24)$$

to obtain a relative error as in equation (5.23).

The errors in (5.23) and (5.24) were correlated by a pull distribution defined as follows:

$$P_T^{pull} = \frac{dP_T^{-1}(rec - gen)}{dP_T^{-1}(trackers)} \quad (5.25)$$

The sigma of the Gaussian fit obtained for each bin should be around 1 if the error is determined correctly. Otherwise we can distinguish between the two cases:

- $P_T^{pull} > 1$: error on the quantity $dP_T^{-1}(trackers)$ is supposed to be under-estimated
- $P_T^{pull} < 1$: error on $dP_T^{-1}(trackers)$ is supposed to be over-estimated

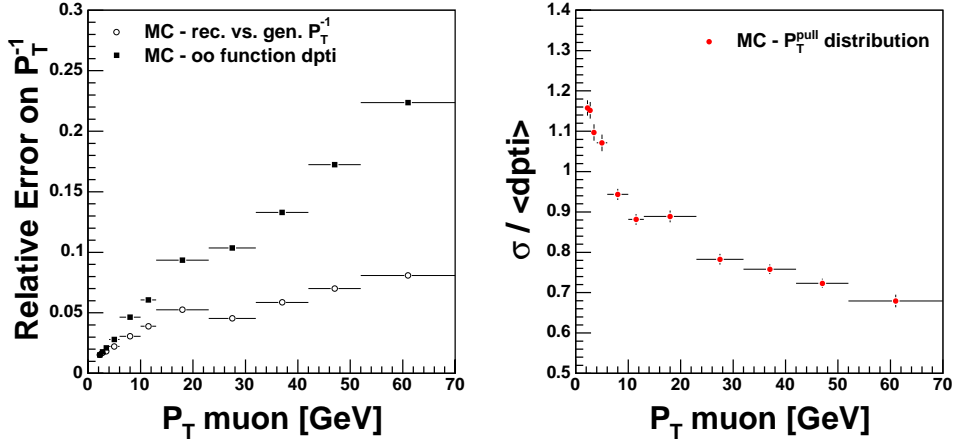


Figure 5.3: The distribution on the difference of inverse momenta of reconstructed and generated particles $dP_T^{-1}(rec - gen)_{rel}$ is compared to the error on inverse P_T provided by the fit of the muon tracks (left). The errors can also be compared by a P_T^{-1} pull distribution (right).

The results of the error studies are presented in figure 5.3. On the left, $dP_T^{-1}(rec - gen)_{rel}$ from equation (5.23) is compared to $dP_T^{-1}(trackers)_{rel}$ from equation (5.24). On the right, the P_T^{pull} distribution (see equation 5.25) is displayed.

We expected to see a similar run of the distributions in figure 5.3 (left) and to find values of σ close to 1 in figure 5.3 (right). However, the values provided by the trackers exceed the values obtained from the comparison between reconstructed and generated transverse momenta by a factor 2-3 at high P_T s.

Two regions can be distinguished in the P_T^{pull} distribution:

- Low P_T : $dP_T^{-1}(trackers) < dP_T^{-1}(rec - gen)_{rel}$
- High P_T : $dP_T^{-1}(trackers) > dP_T^{-1}(rec - gen)_{rel}$

The errors determined by the fit of the muon tracks could be over-estimated in the high- P_T range. However, we have to use $dP_T^{-1}(trackers)$ because of our goal to apply the fit to data events (no availability of generated quantities).

For the muon fit cylindrical coordinates (R, ϕ, z) are used. For R the fixed value of $R_{calo} = 100.5$ cm is taken, which stands for the radial distance between the z -axis and the inner edge of the electromagnetic calorimeter. The azimuthal angle of the muon track ϕ_μ^{tr} , measured with high accuracy, is

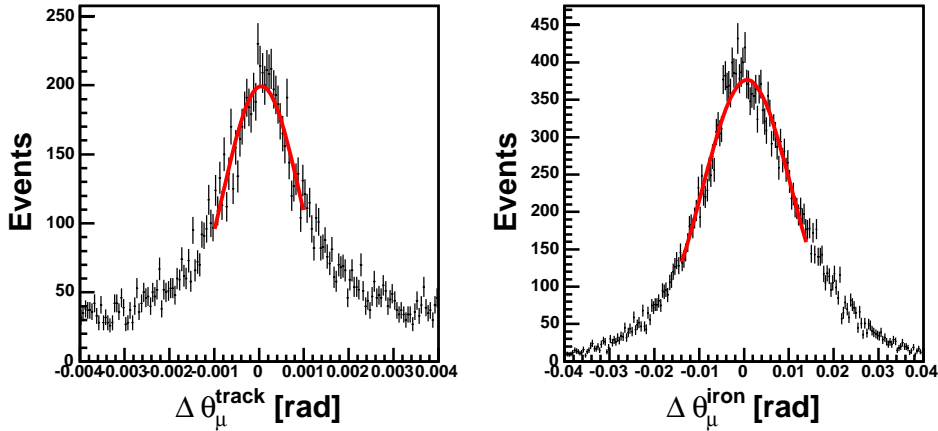


Figure 5.4: Comparison between the polar angles theta of reconstructed muons determined by an inner track θ_{tr}^{rec} (left), or determined via an iron track θ_{iron}^{rec} (right) and generated muons θ^{gen} .

used. The z -coordinate is given by

$$z = \frac{R_{calo}}{\tan \theta_{tr}^{\mu}} + z_V = z_D + z_V \quad (5.26)$$

where z_V is the z -component of the event vertex.

Since z_D corresponds to the distance between the z -components of the impact and the reconstructed vertex, it is denoted by the subscript “ D ”. z_D is a valid fit parameter because it is calculated independently of z -vertex.

We also had to check in which part of the detector, inner trackers or muon system, the better measurement of the polar angle is done. For these purposes, reconstructed and generated particles of a 1999-2000 MC-GRAPPE sample were compared again. We calculated the difference between the reconstructed polar angle θ_{tr}^{rec} measured by the inner tracks and the θ^{gen} of the generated particle. In the same way the angle measured in the iron θ_{iron}^{rec} , were compared to θ^{gen} . We summarise:

$$\Delta\theta_{innertrack} = \frac{\theta_{tr}^{rec} - \theta^{gen}}{\theta^{gen}} \quad \text{and} \quad (5.27)$$

$$\Delta\theta_{ironclus} = \frac{\theta_{iron}^{rec} - \theta^{gen}}{\theta^{gen}} \quad (5.28)$$

The distributions of $\Delta\theta_{innertrack}$ and $\Delta\theta_{ironclus}$ are displayed in figure 5.4. The σ -values of the Gaussian fit were calculated to 0.05° for the inner track

Vector x of the fit parameters:	
Cylindrical coordinates ($\phi_C \rightarrow \phi_{tr}$)	$(R_{calo}, \phi_{tr}, z_D)_{\mu_i}$
Inverse transverse momentum	$(P_T^{-1})_{\mu_i}$
z -Component of the event vertex	z_V
Diagonal elements of the error matrix V_x:	
z_D (using the error of θ)	$(dz_D)_{\mu_i}$
Error on ϕ_{tr} found out by trackers	$d\phi_{tr}$
Error on the inverse P_T	$(dP_T^{-1})_{\mu_i}$
Error on z -vertex	dz_V

Table 5.2: Input quantities for the kinematical fit on muons.

angles and to 0.58° for the iron track angles. This demonstrates that a better resolution on the angular measurement is provided by the inner trackers. Consequently, θ_{tr}^μ is used to calculate the fit variable z_D .

The set of parameters chosen to fit muons is summarised in table 5.2.

5.4 Tests of the Fit Method for Muons

In order to find out whether the chosen fit method for muons works properly, we applied it first to Monte Carlo e - μ - μ events with high invariant masses. The reconstructed observables were fitted, and their initial and final values – particularly M_{12} were compared to the generated quantities. We expected the reconstructed masses to have approached the generated masses after the fit. The results of the kinematical fit applied to three high mass events, are discussed in the next section.

5.4.1 MC Event Sample

As a study example three high-mass events were chosen from a GRAPE Monte Carlo sample.

Event 1

The first event is displayed in figure 5.5:

The survey of the parameters and their corresponding errors is given in

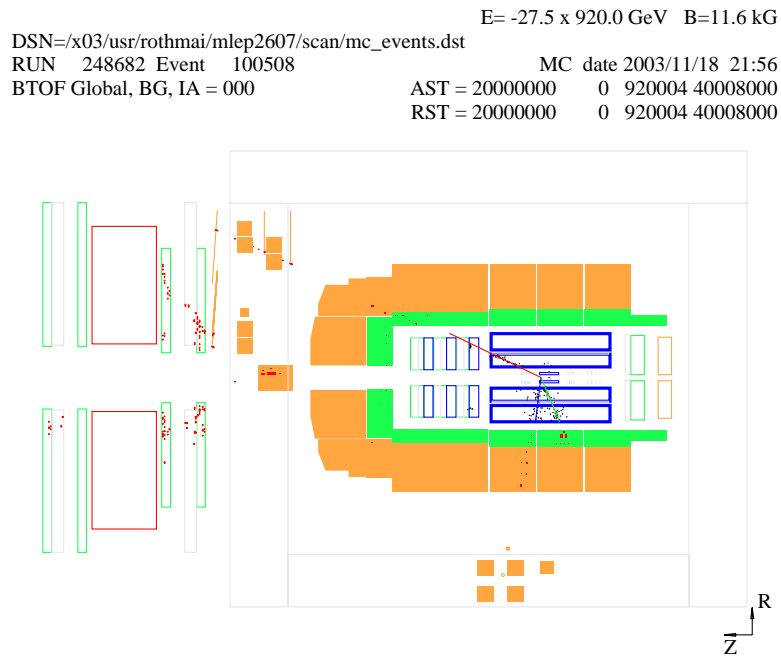


Figure 5.5: Event display of the first MC event.

table 5.3. The dominant uncertainties in the fit input are the errors on the inverse transverse momentum (for the muons), on the energy (electron) and on z-vertex:

- $(dP_T^{-1})_{\mu_1}^{rel} = 7.98 \%$
- $(dP_T^{-1})_{\mu_2}^{rel} = 42.80 \%$
- $(dE)_{ele}^{rel} = 5.26 \%$

a) Input Fit Parameters				
Particle	P_T^{-1} [GeV $^{-1}$]	R [cm]	ϕ [deg]	z [cm]
$\mu 1$	0.0222 ± 0.0018	100.50 ± 0.000001	-73.007 ± 0.013	12.49 ± 2.42
$\mu 2$	0.0271 ± 0.0116	100.50 ± 0.000001	94.620 ± 0.041	201.66 ± 6.06
e	E [GeV]: 8.37 ± 0.44	117.39 ± 1.05	-172.022 ± 0.012	-27.98 ± 1.03
z_V [cm] = 14.96 ± 1.14				
P_T^{miss} [GeV] = 7.91292		$E - P_z$ [GeV] = 59.78446		
Other Event Variables				
Particle	P_T [GeV]	$(E)_{\mu 1,2}$ [GeV]	θ [deg]	
$\mu 1$	45.14	45.49	82.92 ± 1.52	
$\mu 2$	36.85	82.62	26.49 ± 0.79	
e	7.87	see above	109.96 ± 0.68	
Invariant Mass: M_{12}^{ini} [GeV] = 99.68 ± 21.72				
b) Output Fit Parameters				
Particle	P_T^{-1} [GeV $^{-1}$]	R [cm]	ϕ [deg]	z [cm]
$\mu 1$	0.0258 ± 0.0004	100.50 ± 0.000001	-73.007 ± 0.013	12.79 ± 2.27
$\mu 2$	0.0260 ± 0.0004	100.50 ± 0.000001	94.623 ± 0.041	201.88 ± 6.03
e	E [GeV]: 8.84 ± 0.13	117.42 ± 1.05	-172.022 ± 0.012	-25.94 ± 1.03
z_V [cm] = 14.87 ± 1.14				
Other Event Variables				
Particle	P_T [GeV]	$(E)_{\mu 1,2}$ [GeV]	θ [deg]	
$\mu 1$	38.75	39.06	82.75 ± 1.45	
$\mu 2$	38.34	86.03	26.47 ± 0.78	
e	8.32	see above	109.89 ± 0.68	
Invariant Mass: M_{12}^{fit} [GeV] = 94.15 ± 1.34				
P_T^{miss} [GeV] = 0.00001		$\chi^2 = 5.462$		
$E - P_z$ [GeV] = 55.00001		$\chi^2/n_{dof} = 1.821$		

Table 5.3: Kinematical fit of the first e - μ - μ MC event. The input can be seen in a) and the fitted values are given in b).

- $(dz_V)^{rel} = 7.62 \%$

From the input values the quantities $P_T^{miss} = 7.91$ GeV, $E - P_z = 59.78$ GeV and the invariant mass $M_{12}^{ini} = 99.68 \pm 21.72$ GeV are calculated.

The output result is shown in table 5.3 b). It can be seen that only the inverse P_T s and the electron energy are touched by the fit. The P_T of the two muons approach each other ($P_{T\mu_1}^{fin} = 38.75$ GeV, $P_{T\mu_2}^{fin} = 38.34$ GeV), the energy of the electron has slightly increased: $E_{ele}^{fin} = 8.84$ GeV. A good level of convergence has been reached: $P_T^{miss} \simeq 0$ GeV, $E - P_z \simeq 55$ GeV. The final errors on the transverse muon momenta and on the electron energy are now at the order of roughly 1.5%.

The small errors after the fit lead to a relative error on the invariant mass M_{12} of about 1.4%. The result of the χ^2 -test, which was performed to check the fit quality, is 1.821 for χ^2 divided by the number of degrees of freedom. This value indicates that the errors on the parameters were not estimated correctly.

Unfortunately, we cannot show that the invariant mass of the reconstructed event approach $M_{12}^{gen} = 100.46$ GeV. We present the quantities energy and P_T for reconstructed and generated particles:

Component	Rec. Value (ini)	Rec. Value (fin)	Gen. Value
E_{μ_1} [GeV]	45.49	39.06	42.10
$P_{T\mu_1}$ [GeV]	45.14	38.75	41.41
E_{μ_2} [GeV]	82.62	86.03	96.40
$P_{T\mu_2}$ [GeV]	36.85	38.34	40.78
E_{ele} [GeV]	8.37	8.84	8.54
$P_{T_{ele}}$ [GeV]	7.87	8.32	8.06

The reconstructed muon quantities are closer to the generated ones after the fit. In the table below the parameters used to determine M_{12} are shown:

Quantity	Rec. Value (ini)	Rec. Value (fin)	Gen. Value
$E_{\mu_1} + E_{\mu_2}$ [GeV]	128.11	125.09	138.50
$p_{x\mu_1} + p_{x\mu_2}$ [GeV]	10.22	8.24	8.81
$p_{y\mu_1} + p_{y\mu_2}$ [GeV]	-6.44	1.15	1.04
$p_{z\mu_1} + p_{z\mu_2}$ [GeV]	79.55	81.94	94.93

Although the individual values E_{μ_1} and E_{μ_2} were improved, the difference between reconstructed and generated values for the sum of the muon energies

$E_{\mu 1} + E_{\mu 2}$ is larger after the fit.

A bad reconstruction of the polar angle could be the reason for this problem. The reconstructed values of θ before ($\theta_{\mu 1}^{rec, ini} = 82.92^\circ$ and $\theta_{\mu 2}^{rec, ini} = 26.49^\circ$) and after the fit ($\theta_{\mu 1}^{rec, fin} = 82.75^\circ$ and $\theta_{\mu 2}^{rec, fin} = 26.47^\circ$) are rather far from the generated ones, $\theta_{\mu 1}^{gen} = 79.63^\circ$ and $\theta_{\mu 2}^{gen} = 25.02^\circ$.

The generated and reconstructed masses are summarised in the table below:

Reconstructed Mass	Generated Mass
$M_{12}^{rec, ini} = 99.68 \pm 21.72 \text{ GeV}$	$M_{12}^{gen} = 100.46 \text{ GeV}$
$M_{12}^{rec, fin} = 94.15 \pm 1.34 \text{ GeV}$	

In order to test the sensitivity of the fit as to the input, we varied the errors on the inverse transverse momenta of the muons and the error on the electron energy. For each value, the final invariant mass M_{12}^{fin} was checked, and a χ^2 -test was performed. Decreasing values of χ^2 results from increasing values of the errors. The χ^2 is most affected by a variation of $dP_{T\mu 1}^{-1}$. This is shown in figure 5.6.

It can be noted that the invariant masses only depend weakly on the errors.

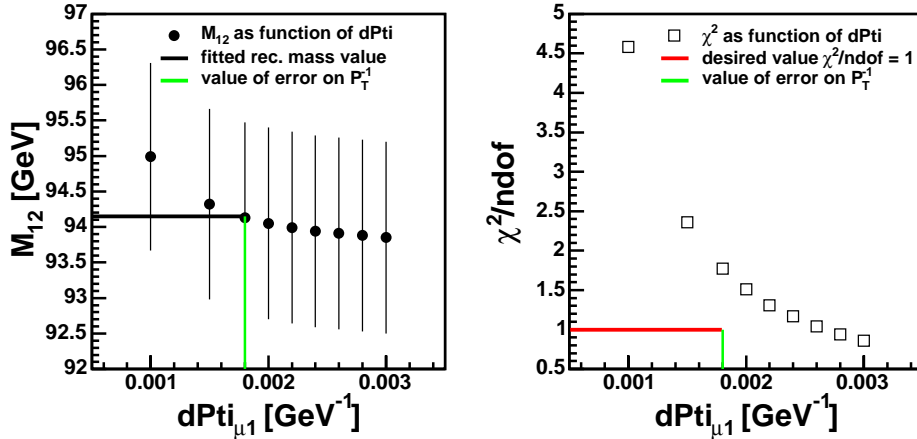


Figure 5.6: MC-Event 1: Distributions of M_{12}^{fin} and χ^2/ndof as functions of the error on $P_{T\mu 1}^{-1}$ from the reconstruction.

The fit is stable. We compared the differences between the reconstructed

and generated values $\Delta_{rec-gen}$ to the errors obtained from the reconstruction software d_{H1REC} . This is shown in the table below:

Quantity	$\Delta_{rec-gen}$	d_{H1REC}
$P_{T\mu_1}$ [GeV]	0.0020	0.0018
$P_{T\mu_2}$ [GeV]	0.0026	0.0116
E_{ele} [GeV]	0.17	0.44
z_{μ_1} [cm]	5.90	2.42
z_{μ_2} [cm]	13.63	6.06
z_{ele} [cm]	1.25	1.03

The errors on the polar angles of the muons from the event reconstruction were under-estimated with respect to the differences between the reconstructed and generated θ values. Consequently, the errors on z_{μ_1} and z_{μ_2} determined from θ were under-estimated.

Event 2

The display of the second event is presented in figure 5.7. All parameters can be found in table 5.4. As for the first event we look at the highest relative errors:

- $(dP_T^{-1})_{\mu_1}^{rel} = 33.13 \%$
- $(dP_T^{-1})_{\mu_2}^{rel} = 7.29 \%$
- $(dE)_{ele}^{rel} = 3.18 \%$

From the 4-vectors of μ_1 and μ_2 the invariant mass is determined to the value $M_{12}^{in} = 107.45 \pm 18.22$ GeV. Due to the big errors on the inverse transverse momenta, the relative error on the invariant mass is $dM_{12}^{rel} = 16.96\%$. The generated mass is $M_{12}^{gen} = 116.52$ GeV.

The quantity most affected by the fit is the transverse momentum of muon 1. This parameter has increased. The final value is $P_{T\mu_1}^{fin,rec} = 64.09$ GeV. The generated value was calculated to $P_{T\mu_1}^{gen} = 64.19$ GeV. The parameters of muon 2 and the electron have hardly changed.

a) Input Fit Parameters				
Particle	P_T^{-1} [GeV $^{-1}$]	R [cm]	ϕ [deg]	z [cm]
$\mu 1$	0.0183 ± 0.0061	100.50 ± 0.000001	-96.308 ± 0.022	249.54 ± 0.73
$\mu 2$	0.0217 ± 0.0016	100.50 ± 0.000001	61.979 ± 0.011	90.88 ± 0.21
e	E [GeV]: 28.60 ± 0.91	114.38 ± 1.34	121.072 ± 0.011	16.86 ± 1.34
z_V [cm] = -6.76 ± 0.01				
P_T^{miss} [GeV] = 10.51632		$E - P_z$ [GeV] = 53.87662		
Other Event Variables				
Particle	P_T [GeV]	$(E)_{\mu 1,2}$ [GeV]	θ [deg]	
$\mu 1$	54.59	146.14	21.94 ± 0.06	
$\mu 2$	46.12	62.19	47.88 ± 0.06	
e	28.01	see above	78.33 ± 0.66	
Invariant Mass: M_{12}^{ini} [GeV] = 107.45 ± 18.22				
b) Output Fit Parameters				
Particle	P_T^{-1} [GeV $^{-1}$]	R [cm]	ϕ [deg]	z [cm]
$\mu 1$	0.0156 ± 0.0001	100.50 ± 0.000001	-96.308 ± 0.022	249.54 ± 0.73
$\mu 2$	0.0221 ± 0.0001	100.50 ± 0.000001	61.979 ± 0.011	90.88 ± 0.21
e	E [GeV]: 28.21 ± 0.20	114.35 ± 1.34	121.072 ± 0.011	17.00 ± 1.30
z_V [cm] = -6.76 ± 0.01				
Other Event Variables				
Particle	P_T [GeV]	$(E)_{\mu 1,2}$ [GeV]	θ [deg]	
$\mu 1$	64.09	171.54	21.94 ± 0.06	
$\mu 2$	45.32	61.10	47.88 ± 0.06	
e	27.62	see above	78.26 ± 0.64	
Invariant Mass: M_{12}^{fit} [GeV] = 115.40 ± 0.54				
P_T^{miss} [GeV] = 0.03817		$\chi^2 = 0.461$		
$E - P_z$ [GeV] = 55.00740		$\chi^2/ndof = 0.154$		

Table 5.4: Kinematical fit of the second e - μ - μ MC event. The input can be seen in a) and the fitted values are given in b).

E= -27.5 x 920.0 GeV B=11.6 kG

DSN=/x03/usr/rothmai/mlep2607/scan/mc_events.dst
 RUN 253700 Event 102293 MC date 2003/11/18 21:56
 BTOF Global, BG, IA = 000 AST = 20000000 7808 20000 304C000
 RST = 20000000 7808 20000 304C000

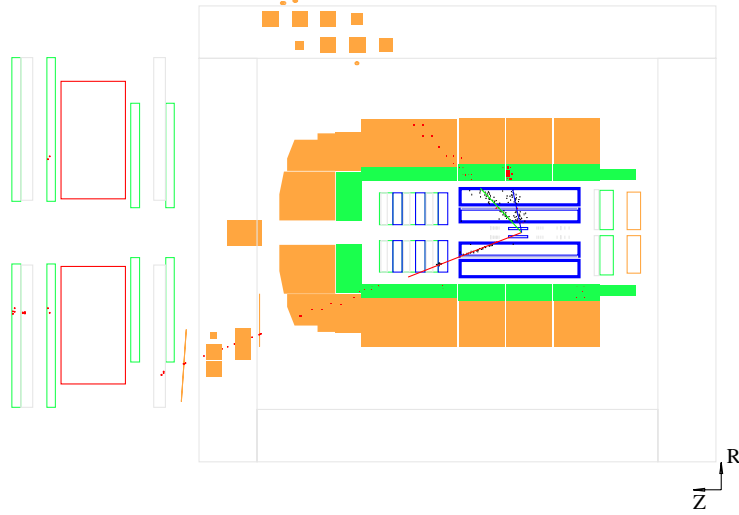


Figure 5.7: Event display of the second MC event.

Consequently, the final invariant mass approaches the generated mass. The comparison can be seen in the table below:

Reconstructed Mass	Generated Mass
$M_{12}^{rec,ini} = 107.45 \pm 18.22 \text{ GeV}$	$M_{12}^{gen} = 116.52 \text{ GeV}$
$M_{12}^{rec,fin} = 115.40 \pm 0.54 \text{ GeV}$	

The final errors on the P_T of the muons and the electron energy (all in the order of 0.4 - 0.7%) are supposed to be too small. Due to the small relative error $dM_{12}^{rel} = 0.45\%$, generated and reconstructed mass do not match within the error interval.

The level of convergence for the fit is not satisfying. As for the first event, the invariant mass and the χ^2 were plotted as functions of the errors dP_T^{-1}

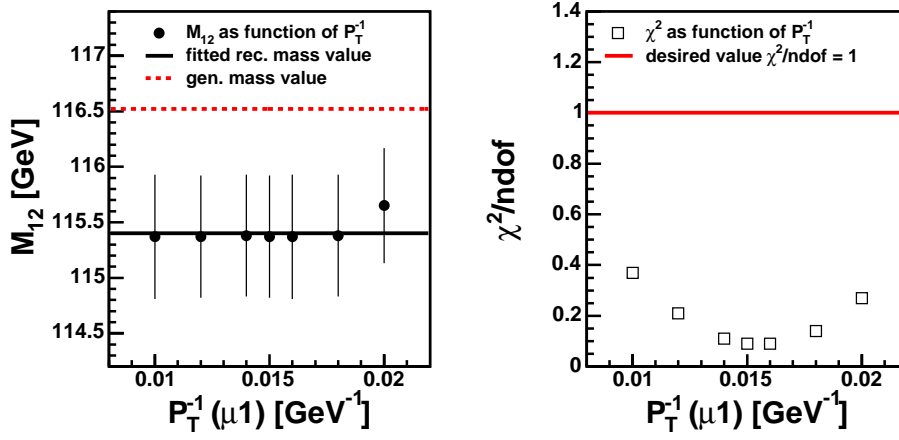


Figure 5.8: MC-Event 2: Distributions of M_{12}^{fin} and χ^2/ndof as functions of the inverse transverse momentum of μ_1 .

and dE , respectively. In addition, the transverse momentum of muon 1 was varied to check as to whether the level convergence could be improved. The distributions are shown in figure 5.9 and figure 5.8.

The three plots on the right in figure 5.9 indicate that the errors on the energy and the transverse momentum were over-estimated. This statement is verified by the comparison between $\Delta_{rec-gen}$ and d_{H1REC} provided in the table below:

Quantity	$\Delta_{rec-gen}$	d_{H1REC}
$P_{T\mu_1}$ [GeV]	0.0027	0.0061
$P_{T\mu_2}$ [GeV]	0.0001	0.0016
E_{ele} [GeV]	0.91	0.91
z_{μ_1} [cm]	0.11	0.73
z_{μ_2} [cm]	0.56	0.21
z_{ele} [cm]	0.01	1.33

Additionally, this conclusion is consistent with the value for $\chi^2/\text{ndof} < 1$. At a value of $P_{T\mu_1}^{-1} = 0.015 \text{ GeV}^{-1}$ a minimum for χ^2 is reached by the fit. This value corresponds to the generated value for muon 1.

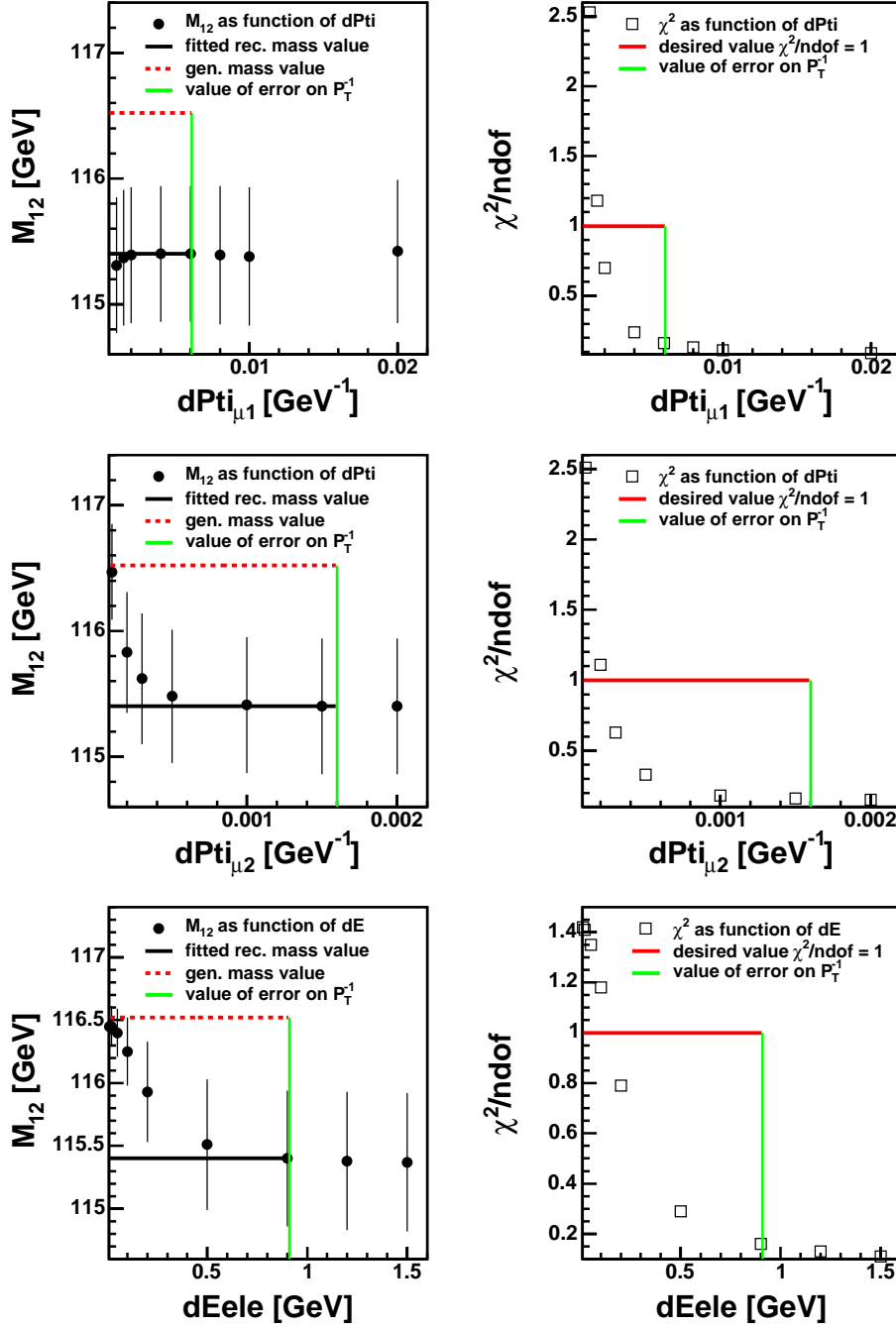


Figure 5.9: MC-Event 2: Distributions of M_{12}^{fin} and $\chi^2/ndof$ as functions of the errors on $P_{T\mu,1,2}^{-1}$ and on E_{ele} from the reconstruction.

E= -27.5 x 920.0 GeV B=11.6 kG

DSN=/x03/usr/rothmai/mlep2607/scan/mc_events.dst
 RUN 266762 Event 108147 MC date 2003/11/18 21:56
 BTOF Global, BG, IA = 000 AST = 20000000 0 0 40000000
 RST = 20000000 0 0 40000000

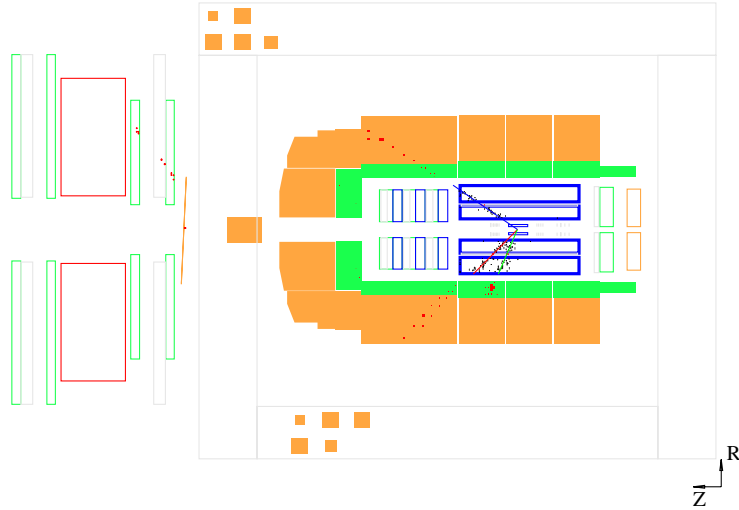


Figure 5.10: Event display of the MC event 3.

Event 3

The third event is visualised in figure 5.10.

The fit parameters are summarised in table 5.5. Since the dominating relative errors are smaller than in the two former cases – $(dP_T^{-1})_{\mu_1}^{rel} = 13.33\%$, $(dP_T^{-1})_{\mu_2}^{rel} = 8.97\%$ and $(dE)_{ele}^{rel} = 4.77\%$ – the relative error on the initial invariant mass is calculated to 8.12%.

a) Input Fit Parameters				
Particle	P_T^{-1} [GeV $^{-1}$]	R [cm]	ϕ [deg]	z [cm]
$\mu 1$	0.0127 ± 0.0017	100.50 ± 0.000001	52.606 ± 0.011	141.77 ± 2.86
$\mu 2$	0.0156 ± 0.0014	100.50 ± 0.000001	-136.968 ± 0.010	96.97 ± 3.00
e	E [GeV]: 11.54 ± 0.55	114.58 ± 0.76	-71.304 ± 0.012	48.34 ± 0.76
z_V [cm] = 1.35 ± 1.32				
P_T^{miss} [GeV] = 9.93774		$E - P_z$ [GeV] = 59.49870		
Other Event Variables				
Particle	P_T [GeV]	$(E)_{\mu 1,2}$ [GeV]	θ [deg]	
$\mu 1$	78.90	136.43	35.33 ± 0.61	
$\mu 2$	64.07	89.03	46.02 ± 0.98	
e	10.67	see above	67.70 ± 0.67	
Invariant Mass: M_{12}^{ini} [GeV] = 143.18 ± 11.62				
b) Output Fit Parameters				
Particle	P_T^{-1} [GeV $^{-1}$]	R [cm]	ϕ [deg]	z [cm]
$\mu 1$	0.0151 ± 0.0001	100.50 ± 0.000001	52.605 ± 0.011	141.70 ± 2.82
$\mu 2$	0.0166 ± 0.0001	100.50 ± 0.000001	-136.968 ± 0.010	96.55 ± 2.89
e	E [GeV]: 13.05 ± 0.11	114.64 ± 0.76	-71.304 ± 0.012	48.19 ± 0.76
z_V [cm] = 1.80 ± 1.31				
Other Event Variables				
Particle	P_T [GeV]	$(E)_{\mu 1,2}$ [GeV]	θ [deg]	
$\mu 1$	66.29	114.59	35.35 ± 0.60	
$\mu 2$	60.38	83.73	46.15 ± 0.95	
e	12.10	see above	67.97 ± 0.66	
Invariant Mass: M_{12}^{fit} [GeV] = 126.89 ± 1.38				
P_T^{miss} [GeV] = 0.00005		$\chi^2 = 10.202$		
$E - P_z$ [GeV] = 55.00001		$\chi^2/ndof = 3.401$		

Table 5.5: Kinematical fit of the third e - μ - μ MC event. The input can be seen in a) and the fitted values are given in b).

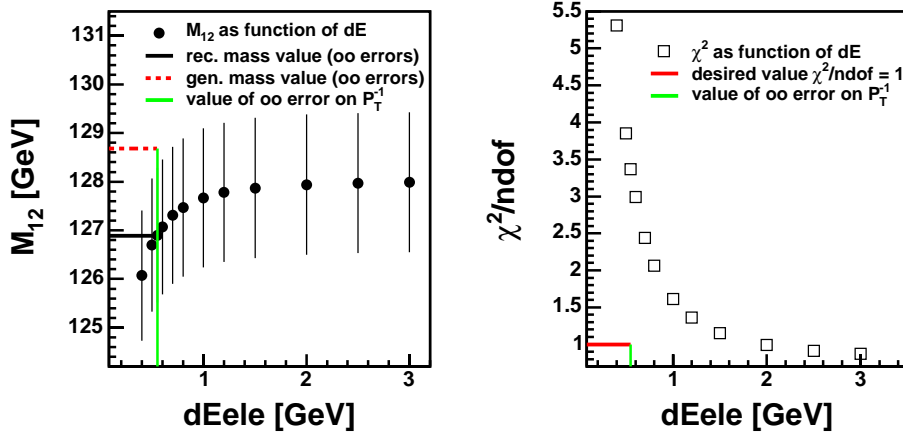


Figure 5.11: MC-Event 3: Distributions of M_{12}^{fin} and $\chi^2/ndof$ as functions of the error on E_{ele} from the reconstruction.

The final values for the constraint equations are satisfying and the reconstructed mass converges to the generated mass as can be seen in the table below:

Reconstructed Mass	Generated Mass
$M_{12}^{rec,ini} = 143.18 \pm 11.62$ GeV	$M_{12}^{gen} = 128.68$ GeV
$M_{12}^{rec,fin} = 126.89 \pm 1.38$ GeV	

However, the $\chi^2/ndof = 3.401$ indicates that the size of the errors were under-estimated. Despite the comparable values of M_{12}^{gen} and M_{12}^{rec} there is no matching within the error interval. Further checks on the size of the uncertainties were done, and the result is presented in figure 5.11.

It is found that the final invariant mass is influenced by a variation of dE_{ele} . At higher values, the final reconstructed mass increases, and shows a further approach to the generated mass. The χ^2 , divided by the number of degrees of freedom, converge to a value of 1. For $dE_{ele} = 0.88$ GeV, which is the value of $\Delta E_{rec-gen}$, the χ^2 is at around 1.5. The check above shows how sensitive the fit reacts to the input parameters.

5.4.2 Conclusion

Three $e\text{-}\mu\text{-}\mu$ Monte Carlo events were fitted by the method of constrained least squares. It has been shown that in two of the three cases the reconstructed invariant mass M_{12}^{ec} was improved and values of parameters approached the generated values. However, the χ^2 test indicated that the kinematics of the events were not completely understood within the measurement errors. Subsequent checks showed that errors on some variables could be slightly under- or overestimated. This results from the difficulties to estimate the errors on $P_{T\mu}$ and θ_μ correctly. In addition, we verified that the χ^2 is a good estimator for the quality of the fit.

In the next section the kinematical fit is applied to the two high- P_T events from the $e\text{-}\mu\text{-}\mu$ -channel.

5.5 Fit Results

5.5.1 Run 367354, Event 22364

The display of Run 367354, Event 22364 is provided in figure 5.12. In the event one high- P_T muon ($P_{T\mu_1}^{ini} = 73.12$ GeV, $\theta_{\mu_1} = 36.62^\circ$), and one low- P_T muon ($P_{T\mu_2}^{ini} = 2.75$ GeV, $\theta_{\mu_2} = 105.73^\circ$), were detected. The scattered electron was found to also have a large transverse momentum at a value of $P_{T_e}^{ini} = 64.00$ GeV. It was emitted under a polar angle $\theta_{ele} = 52.93^\circ$. In the forward direction between $-5^\circ < \theta < 5^\circ$) a small hadronic activity was observed. A transverse momentum of $P_T^{had} = 0.43$ GeV was determined by the reconstruction software.

In table 5.6 the input quantities of the fit are summarised. Due to the hadronic fraction, the set of parameters is extended to four hadronic parameters:

- $P_{had} = \sqrt{p_{had,x}^2 + p_{had,y}^2 + p_{had,z}^2}$
- θ_{had}
- ϕ_{had}
- $M_{had} = \sqrt{E_{had}^2 - P_{had}^2}$

a) Input Fit Parameters				
Particle	P_T^{-1} [GeV $^{-1}$]	R [cm]	ϕ [deg]	z [cm]
$\mu 1$	0.0137 ± 0.0020	100.50 ± 0.000001	-151.821 ± 0.017	135.22 ± 2.97
$\mu 2$	0.3632 ± 0.0049	100.50 ± 0.000001	153.592 ± 0.032	-28.33 ± 3.30
e	E [GeV]: 80.21 ± 2.09	113.73 ± 0.54	28.940 ± 0.018	73.58 ± 0.54
z_V [cm] = -12.34 ± 1.60				
Hadronic Part:				
P_{had} [GeV]: 38.80 ± 10.00		M_{had} [GeV]: 3.77 ± 1.00		
θ_{had} [deg]: 0.55 ± 5.73		ϕ_{had} [deg]: -74.71 ± 8.59		
P_T^{miss} [GeV] = 11.14367		$E - P_z$ [GeV] = 57.80988		
Other Event Variables:				
Particle	P_T [GeV]	$(E)_{\mu 1,2}$ [GeV]	θ [deg]	
$\mu 1$	73.12	122.58	36.62 ± 0.61	
$\mu 2$	2.75	2.85	105.73 ± 1.70	
e	64.00	see above	52.93 ± 1.09	
Invariant Mass: M_{12}^{in} [GeV] = 139.68 ± 10.17				
b) Output Fit Parameters				
Particle	P_T^{-1} [GeV $^{-1}$]	R [cm]	ϕ [deg]	z [cm]
$\mu 1$	0.0160 ± 0.0002	100.50 ± 0.000001	-151.821 ± 0.017	135.17 ± 2.92
$\mu 2$	0.3632 ± 0.0049	100.50 ± 0.000001	153.592 ± 0.032	-28.35 ± 3.30
e	E [GeV]: 80.91 ± 1.29	113.69 ± 0.53	28.940 ± 0.018	73.56 ± 0.53
z_V [cm] = -12.15 ± 1.34				
Hadronic Part:				
P_{had} [GeV]: 40.12 ± 9.80		M_{had} [GeV]: 3.78 ± 1.00		
θ_{had} [deg]: 4.53 ± 1.11		ϕ_{had} [deg]: -73.84 ± 8.55		
Other Event Variables:				
Particle	P_T [GeV]	$(E)_{\mu 1,2}$ [GeV]	θ [deg]	
$\mu 1$	62.36	105.04	36.42 ± 0.59	
$\mu 2$	2.75	2.85	105.29 ± 5.27	
e	64.32	see above	52.65 ± 1.06	
Invariant Mass: M_{12}^{fit} [GeV] = 129.63 ± 1.46				
P_T^{miss} [GeV] = 0.00002			$\chi^2 = 2.098$	
$E - P_z$ [GeV] = 54.99999			$\chi^2/ndof = 0.699$	

Table 5.6: Kinematical fit of the e - μ - μ event: Run 367354, Event 22364. The upper part a) shows the input, in the lower part b) the fit result is presented.

DSN=/x03/usr/rothmai/mlep2607/scan/EMuMuHera2.dst
 RUN 367354 Event 22364
 E= -27.6 x 920.0 GeV B=11.6 kG
 AST (DMIS) = 0 380D 10000400 34C8000
 RST (DMIS) = 80000000 10388D 52500405 34C8000

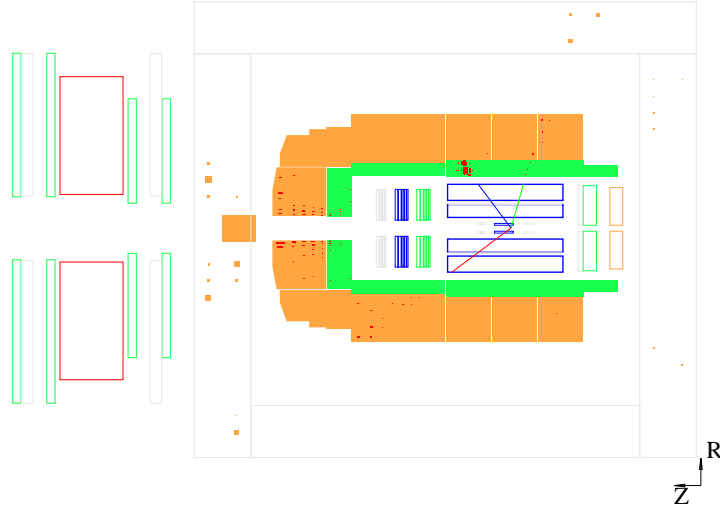


Figure 5.12: Event Display for Run 367354, Event 22364.

Because of the location of the hadronic noise around the beam pipe, large errors on the hadronic observables were expected. The error on θ was supposed at the order of 0.1 rad (5.73°). This value corresponds to the dimensions of the region where hadronic activity was found.

Large values of the relative error were determined on the following quantities:

- $dP_{T\mu_1} = 14.60 \%$
- $dz_{\mu_2} = 11.48 \%$ due to a large error on θ
- $dz_v = 12.97 \%$

The momentum of the low-energetic muon was determined with high accuracy. This shows that a good P_T -measurement is obtained if the curvature of the track is large. From the input quantities the invariant mass is calculated to $M_{12}^{ini} = 139.68 \pm 10.17$ GeV. The value of the relative error on the initial mass is 7.28%.

In figure 5.12 b) the fit output is presented. The level of convergence is satisfying. A value of $\chi^2/ndof$ around 0.7 shows that kinematics of this event are well understood. The quantities most affected by the fit are the transverse momentum of the high-energetic muon and the polar angle of the hadronic part. $P_{T\mu_1}$ has decreased to a value of 62.36 GeV. θ_{had} has also been used to balance the fit. Its final value has increased to 4.53° , and the error has been reduced to a value of 1.11° . Due to the smaller transverse momentum of muon 1, the final invariant mass is $M_{12}^{fin} = 129.63 \pm 1.46$ GeV. The relative error dM_{12}^{fin} is at the order of 1%.

The fitted invariant mass M_{12} is compared to the mass value obtained from the P_T -balance method in table 5.7.

Variable	P_T -Balance	Kinematical Fit
$P_{T\mu_1}^{ini}$ [GeV]		73.12
$P_{T\mu_2}^{ini}$ [GeV]		2.75
M_{12}^{ini} [GeV]		139.68
$P_{T\mu_1}^{cor}$ [GeV]	62.27	62.36
$P_{T\mu_2}^{cor}$ [GeV]	2.75	2.75
M_{12}^{cor} [GeV]	128.89	129.63

Table 5.7: Comparison between the “ P_T ”-balance method and the kinematical fit for Run 367354, Event 22364.

It is shown that the result of the kinematical fit corresponds to the result of the P_T -balance correction. Within the error interval the final masses match each other. In this event, there is only one high-energetic muon with a large error on P_T . The momentum of the second muon was determined precisely. By both methods, the transverse momentum of μ_1 has decreased to a final value at around 62 GeV.

5.5.2 Run 383168, Event 78379

The display of Run 383168, Event 78379 is in figure 5.13. Two high-energetic muons with transverse momenta in the range between 45 GeV and 50 GeV, and the scattered electron with $P_{T_{ele}} = 4.64$ GeV were observed in the event. For muon 1 a polar angle of $\theta_{\mu_1} = 50.44^\circ$ was determined, for muon 2 a value of $\theta_{\mu_2} = 24.01^\circ$ was measured. The electron was observed in the SpaCal

E= -27.6 x 920.0 GeV B=11.6 kG

DSN=/x03/usr/rothmai/mlep2607/scan/EMuMu_2003_04.dst

RUN 383168 Event 78379

AST (DMIS) =	0	20 20000302	68209
RST (DMIS) =	0	70 6150031E	68219

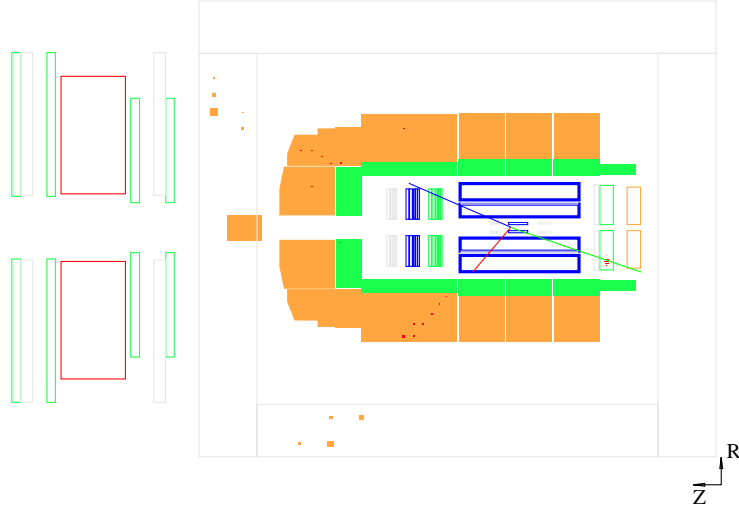


Figure 5.13: Event Display for Run 383168, Event 78379.

($\theta_{ele} = 159.94^\circ$). No hadronic activity was found in the event.

Table 5.8 summarises the input and output parameters of the fit. A very large error on the inverse P_T of μ_2 was determined. The relative error is 68.37%. Large uncertainties were also indicated on the inverse P_T of muon 1 (at about 10%), on the electron energy (at about 4%), and on z_v (at the order of 14%). The error on the energy of the SpaCal electron was calculated by the formula $\sigma_E/E = 0.071/\sqrt{E} \oplus 3\%$ considering the calibration for new data. By the value of $dz_{ele} = 3$ cm, the uncertainty was taken into account to determine the z -position of the electron in the SpaCal. Due to the large value of $(dP_T^{-1})_{\mu_2}$ the error on the invariant mass is evaluated to 35.40 GeV. This corresponds to a relative value of 34.45%. The initial mass M_{12}^{ini} is in the region around 100 GeV.

a) Input Fit Parameters				
Particle	P_T^{-1} [GeV $^{-1}$]	R [cm]	ϕ [deg]	z [cm]
$\mu 1$	0.0205 ± 0.0020	100.50 ± 0.000001	-143.115 ± 0.020	83.01 ± 3.60
$\mu 2$	0.0215 ± 0.0147	100.50 ± 0.000001	42.554 ± 0.055	225.65 ± 7.61
e	E [GeV]: 13.54 ± 0.86	63.19 ± 0.82	-12.900 ± 0.746	-158.02 ± 3.00
z_V [cm] = 15.08 ± 2.15				
P_T^{miss} [GeV] = 1.18866		$E - P_z$ [GeV] = 59.12221		
Other Event Variables				
Particle	P_T [GeV]	$(E)_{\mu 1,2}$ [GeV]	θ [deg]	
$\mu 1$	48.76	63.24	50.44 ± 1.123	
$\mu 2$	46.54	114.39	24.01 ± 0.70	
e	4.64	see above	159.94 ± 0.42	
Invariant Mass: M_{12}^{ini} [GeV] = 102.80 ± 35.40				
b) Output Fit Parameters				
Particle	P_T^{-1} [GeV $^{-1}$]	R [cm]	ϕ [deg]	z [cm]
$\mu 1$	0.0243 ± 0.0004	100.50 ± 0.000001	-143.114 ± 0.020	83.41 ± 3.53
$\mu 2$	0.0262 ± 0.0005	100.50 ± 0.000001	42.545 ± 0.054	226.05 ± 7.57
e	E [GeV]: 14.22 ± 0.22	63.37 ± 0.82	-13.024 ± 0.743	-157.14 ± 2.97
z_V [cm] = 14.62 ± 2.14				
Other Event Variables				
Particle	P_T [GeV]	$(E)_{\mu 1,2}$ [GeV]	θ [deg]	
$\mu 1$	41.17	53.40	50.31 ± 1.20	
$\mu 2$	38.20	94.00	23.97 ± 0.68	
e	4.89	see above	159.75 ± 0.41	
Invariant Mass: M_{12}^{fit} [GeV] = 85.55 ± 1.50				
P_T^{miss} [GeV] = 0.00023		$\chi^2 = 4.72$		
$E - P_z$ [GeV] = 55.00001		$\chi^2/ndof = 1.57$		

Table 5.8: Kinematical fit of the e - μ - μ event: Run 383168, Event 78379. The input can be seen in a), while the fitted values are given in b).

A good level of convergence is reached by the fit. The fit mainly changes the transverse momenta of the muons and the energy of the electron. Both muon momenta have decreased whereas the electronic energy has slightly increased. The final relative errors on these quantities are at values between 1.5% and 2%. Consequently, the invariant mass has decreased after the fit. It is re-calculated to $M_{12}^{fin} = 85.55 \pm 1.50$ GeV. The relative error on the final mass is 1.8%.

The result of the χ^2 -test indicates that the errors on the fit parameters were slightly under-estimated. Considering χ^2 a function of the errors it is observed that with larger errors on ($P_{T\mu_1}^{-1}$) and E_{ele} , the value of $\chi^2/ndof$ approaches 1.

In table 5.9 the kinematical fit is compared to the P_T -balance method.

Variable	P_T -Balance	Kinematical Fit
$P_{T\mu_1}^{ini}$ [GeV]		48.76
$P_{T\mu_2}^{ini}$ [GeV]		46.53
M_{12}^{ini} [GeV]		102.80
$P_{T\mu_1}^{cor}$ [GeV]	48.76	41.17
$P_{T\mu_2}^{cor}$ [GeV]	45.90	38.20
M_{12}^{cor} [GeV]	102.09	85.71

Table 5.9: Comparison between the “ P_T ”-balance method and the kinematical fit for Run 383168, Event 78379.

In this case a large error on the transverse momenta of both muons were determined. The transverse momenta of muon 1 and muon 2 were reduced by the kinematical fit. The balance method only changes the P_T of muon 2. Thus, the results are very different. The relative difference between initial mass and final mass is 0.7% for the balance method, and 16.6% for the kinematical fit.

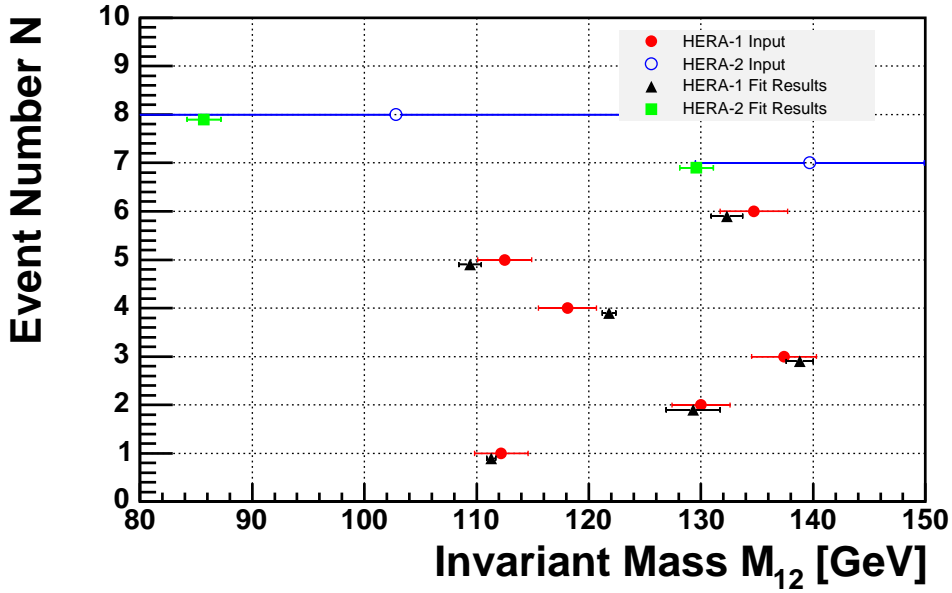


Figure 5.14: Kinematical fit: improvement of the resolution on invariant masses shown for eight high mass events. Six multi-electron events are from HERA-I (the filled points correspond to the initial masses, the triangles correspond to the fitted masses). Two $e\text{-}\mu\text{-}\mu$ events are from HERA-II (open points for the initial masses and rectangles for the fitted masses).

5.5.3 Summary

In figure 5.14 the results of the kinematical fit on the high- P_T events of the multi-lepton analysis is summarised. For each fitted event the initial and final invariant masses have been plotted. Due to large errors obtained from P_T -measurement at high P_T , the initial errors on the initial masses are much larger for $e\text{-}\mu\text{-}\mu$ events than for $e\text{-}e\text{-}e$ or $e\text{-}e$ events. Final errors are at the same order. The largest initial values of $E - P_z$ and P_T^{miss} for the fitted multi-electron events were 57.38 GeV and 3.54 GeV, respectively. For the $e\text{-}\mu\text{-}\mu$ events, the fit had to be accomplished with a $E - P_z$ value of 59.12 GeV (Run 383168, Event 78379) and a missing transverse momentum of 11.14 GeV (Run 367354, Event 22364). The χ^2 obtained from the HERA-II fit are 0.70 and 1.57. This result is consistent with the χ^2 values between 0.68 and 1.74 obtained from the HERA-I fit.

Unfortunately, no indication for the decay of a resonance at high invariant masses has been found.

Chapter 6

Conclusion and Outlook

High- P_T multi-lepton production was investigated in events taken by the H1 detector during 1994-2000 and 2003-2004. Di- and tri-lepton classes were studied in detail. Data were compared to Standard Model prediction in the two and three lepton classes and their derived sub-classes, $e-e$, $e-\mu$, $\mu-\mu$, $e-e-e$, and $e-\mu-\mu$. A good general agreement between experiment and theory was verified. However, in some channels a slight excess of data with respect to the Monte Carlo prediction was observed. In the range of $\sum E_T > 100$ GeV three events in the $l-l$ class and one event in the $l-l-l$ class were detected, compared to SM expectations of 0.42 ± 0.04 and 0.11 ± 0.02 , respectively. With invariant di-lepton masses larger than 100 GeV, eight events were found. To improve kinematics resolution, a kinematical fit was developed and applied to these events. Good results were obtained from the fit, indicated by a good convergence level and the χ^2 . The value of the latter between 0.7 and 1.7 shows that the kinematics of the high mass events are well understood within the error measurement. The M_{12} values obtained were found to be incompatible with the assumption that the lepton pairs were possibly produced by the decay of a single narrow resonance.

Outlook

In the analysis, the non-leptonic background due to photons and pions was suppressed by adequate criteria. Additional cuts were applied in the di-muon channel to reject cosmic muon events in the detector. However, purifying the di-lepton channels, particularly the $e-\mu$ class, should still be an objective for future research.

It would also be an attractive goal to extend the phase-space of the di-lepton class in the forward region down to 10° . This region is supposed to provide

a good source for high masses.

Since statistics are insufficient, the small deviation between data and theory in the high P_T range can not exclude a statistical fluctuation. More integrated luminosity would be required to allow further interpretations.

It should also be an objective to obtain a more profound knowledge of error measurement. The kinematical fit method could be extended to all events as was done in case of the P_T balance method. This would provide a better understanding of event kinematics.

Bibliography

- [Abe01] T. Abe, *GRAPE-Dilepton (Version 1.1): A generator for dilepton production in ep collisions*, Comput. Phys. Commun. **136**, 126 (2001) [arXiv:hep-ph/0012029].
- [Art91] N. Arteaga-Romero, C. Carimalo, P. Kessler, *High P_T lepton pair production at ep colliders: Comparison between various production mechanisms*, Z.Phys. C **52**, 289 (1991).
- [Bar91] S.P. Baranov, H. Shooshtari, J.A. Vermaseren, *LPAIR: A generator for lepton pair production*, Proceedings, Physics at HERA, vol.3, 1478-1482.
- [Ber98] C. Berger, P. Kandel *A new generator for wide angle Bremsstrahlung*, In workshop on Monte Carlo generators for HERA, (1998). Physics Plenary Starting Meeting, Hamburg, Germany, 27-30 Apr. 1998.
- [Blo97] V. Blobel, *Constrained Least Squares and Error Propagation*, Hamburg (1997).
- [Blo02] V. Blobel, *Statistical and Numerical Methods of Data Analysis*, Vorlesungsskript, Hamburg (2002).
- [Bru94] R. Brun et al., *GEANT Detector Description and Simulation Tool*, CERN Program Library, **W5013**, (1994).
- [Bru98] P. Bruel, *Recherche d'interaction au-delà du Modèle Standard à HERA*, PhD Thesis, Univ. de Paris-Sud (1998) 81-89.
- [CDF04] CDF Collaboration, *Search for Doubly-Charged Higgs Bosons Decaying to Dileptons in $p\bar{p}$ Collisions at $\sqrt{s}=1.96$ TeV*, Phys. Rev. Lett. **93**, 22180 (2004).
- [Gel79] M. Gell-Mann, M. P. Ramond and R. Slansky, in Supergravity (1979).

- [H197] H1 Collaboraton , *The tracking, calorimeter and muon detectors of the H1 experiment at HERA*, Nucl. Instr. Meth. A **386**, 348-396 (1997).
- [H103a] H1 Collaboration, *Multi-Electron Production at High Transverse Momenta in ep Collisions at HERA*, Eur.Phys.J. C **31**,17-29 (2003).
- [H103b] H1 Collaboration, *Measurement and QCD Analysis of Neutral and Charged Current Cross Sections at HERA*, Eur.Phys.J. C **30** (2003), 1-32.
- [H104a] H1 Collaboration, *Search for doubly charged Higgs production at HERA*, E. Sauvan, presented at ICHEP2004, H1prelim-04-161.
- [H104b] H1 Collaboration, *Muon Pair Production in ep Collisions at HERA*, Eur.Phys.J. B **583**, 28-40 (2004).
- [H104c] H1 Private Communication (2004).
- [H1oo] H1 Collaboration, *The H1 OO Physics Analysis Project*, Internal H1 Document (2004).
- [Hei99] B. Heinemann *Measurement of Charged Current and Neutral Current Cross Sections in Positron-Proton Collisions at $\sqrt{s} \simeq 300$ GeV*, PhD Thesis, Universität Hamburg (1999), 44-47
- [Jun92] H. Jung, *The Monte Carlo generator EPJPSI for J/Psi mesons in high-energy electron proton collisions*, Aachen Tech. Hochsch., PITHA-92-10 (92/04, rec.Apr.).
- [Jun95] H. Jung, *Hard diffractive scattering in high-energy ep collisions and the Monte Carlo generation RAPGAP*, Comp. Phys. Commun., **86**, 147-161 (1995).
- [Kae00] H.C. Kästli, *Muon Pair Production with High Invariant Mass in e^+p Collisions at HERA*, PhD Thesis, ETH Zürich (2000) 32-34, 42-44.
- [Lan98] U. Langenegger, *A Measurement of the Beauty and Charm Production Cross Sections at the ep Collider HERA*, PhD Thesis, ETH Zürich (1998), 23-30.
- [Lei02] B. Leissner, *Muon Pair Production*, PhD Thesis, RTWH Aachen (2002).

- [LEP03] DELPHI Collaboration, *Search for Doubly Charged Higgs Bosons at LEP2*, Phys. Lett. B **552**, 127 (2003); L3 Collaboration, *Search for Doubly-Charged Higgs Bosons at LEP*, Phys. Lett. B **576**, 18-28 (2003); OPAL Collaboration, *Search for Doubly Charged Higgs Bosons with the OPAL detector at LEP*, Phys. Lett. B **526**, 221-232 (2002).
- [Lis98] B. List, A. Mastroberardino, *DIFFVM: A Monte Carlo generator for diffractive processes in ep scattering*, Prepared for workshop on Monte Carlo generators for HERA physics (Plenary Starting Meeting), Hamburg, Germany, 27-30 Apr 1998.
- [Moh80a] R.N. Mohapatra, R.E. Marshak, *Local B-L Symmetry of Electroweak Interactions, Majorana Neutrinos, and Neutron Oscillations*, Phys. Rev. Lett. **44**, 1316-1319 (1980).
- [Moh80b] R.N. Mohapatra, G. Senjanovic, *Spontaneous Parity Violation and Neutrino Masses*, Phys. Rev. Lett. **44** 912 (1980).
- [OPAL03] OPAL Collaboration, *Search for the Single Production of Doubly-Charged Higgs Bosons and Constraints on their Couplings from Bhabha Scattering* Phys. Lett. B **577**, 93-108 (2003).
- [PDG04] Particle Data Group, *Review of Particle Physics*, Physics Letters B **592** (2004).
- [Pee03] M. Peez, *Recherche de déviations au Modèle Standard dans les processus de grande énergie transverse sur le collisionneur électron-proton HERA*, PhD Thesis, Univ. Claude Bernard Lyon (2003).
- [Sak69] J.J. Sakurai, *Vector-Meson Dominance and High-Energy Electron-Proton Inelastic Scattering*, Phys. Rev. Lett. **22**, 981-984 (1969).
- [Schm02] C. Schmitz, *Elektroproduktion von Myon-Paaren im Massenbereich der Υ -Resonanz*, Diploma Thesis, RTWH Aachen (2002) 22-30.
- [Schu91] G.A. Schuler, H. Spiesberger, *DJANGO: The interface for the event generators HERACLES and LEPTO*, In Hamburg, physics at HERA, vol.3, 1419-1432, (1991).

- [Sco00] P. Scott, *Chi-Square: Testing for Goodness of Fit*, Lab Manual, UC Santa Cruz (2000).
- [Sjo01] T. Sjöstrand, L. Lonnblad, S. Mrenna *PYTHIA 6.2: Physics and manual*, [arXiv:hep-ph/0108264].
- [Wes97] L. West, *How to use the Heavy Flavour Working Group Track, Muon and Electron Selection Code*, Internal H1 Note (1997).

Appendix

In the appendix we show event displays of each class. All events displayed here, were recorded in the HERA-II run.

```
E= -27.6 x 920.0 GeV B=11.6 kG
DSN=/x03/usr/rothmai/mlep2607/scan/2EHera2.dst
RUN 386346 Event 81626
AST (DMIS) = 0 1808 0 0
RST (DMIS) = 0 1858 4250000 0
```

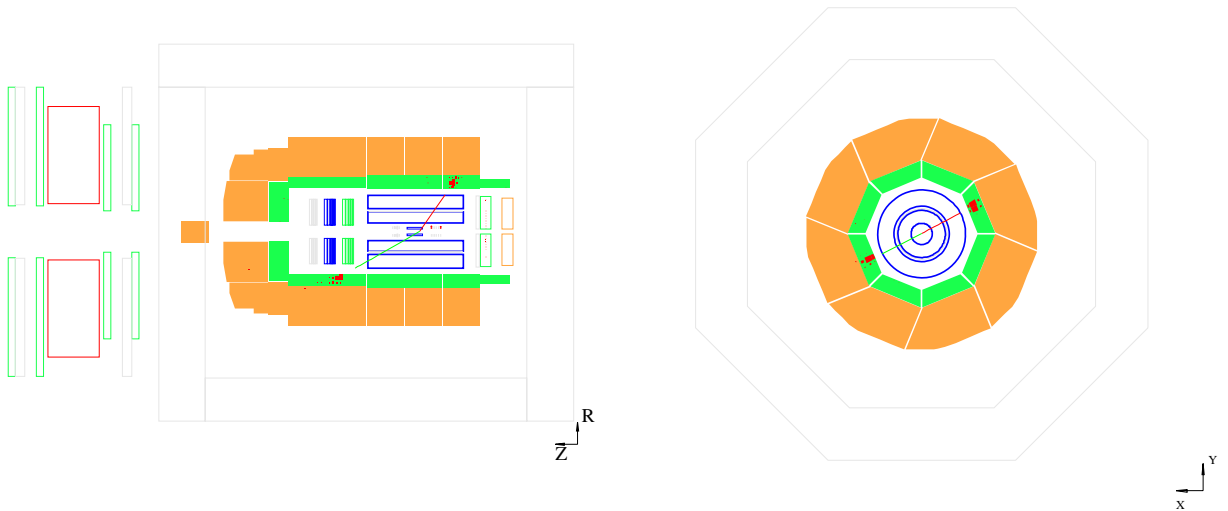


Figure 1: Longitudinal view of a di-electron event with invariant mass $M_{12} = 75.86$ GeV in the 2004 data.

E= -27.6 x 920.0 GeV B=11.6 kG
 DSN=/x03/usr/rothmai/mlep2607/scan/EMuHera2.dst
 RUN 384095 Event 110801
 AST (DMIS) = 0 7808 0 3048000
 RST (DMIS) = 0 78D8 42500000 304A000

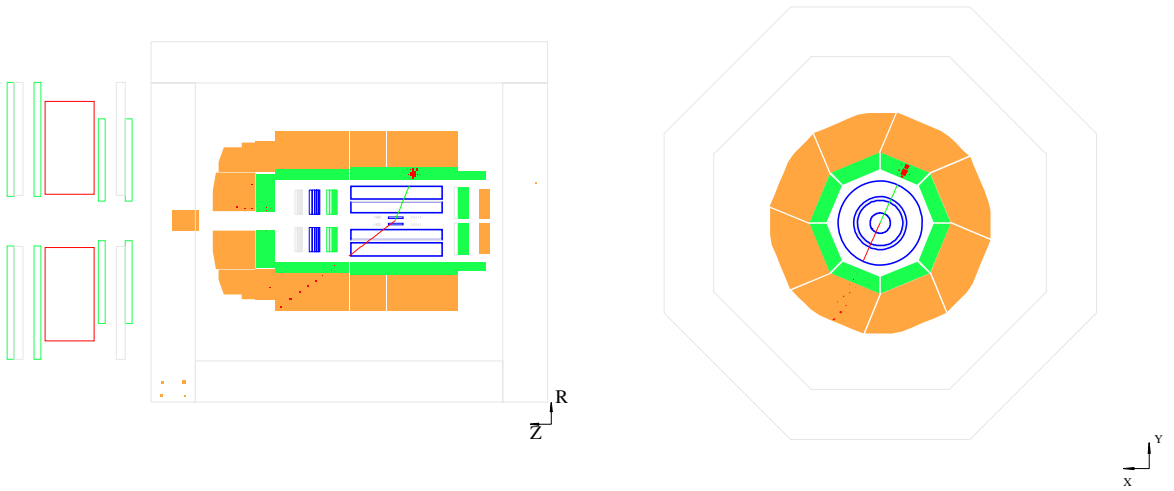


Figure 2: Longitudinal view of an event with one electron ($P_{T_{ele}} = 29.35$ GeV) and one muon ($P_{T_{\mu}} = 31.07$ GeV) in the detector. The invariant mass is $M_{12} = 77.34$ GeV.

E= -27.6 x 920.0 GeV B=11.6 kG
 DSN=/x03/usr/rothmai/mlep2607/scan/MuMuHera2.dst
 RUN 369195 Event 24677
 AST (DMIS) = 0 0 0 40000
 RST (DMIS) = 0 50 40500004 48000

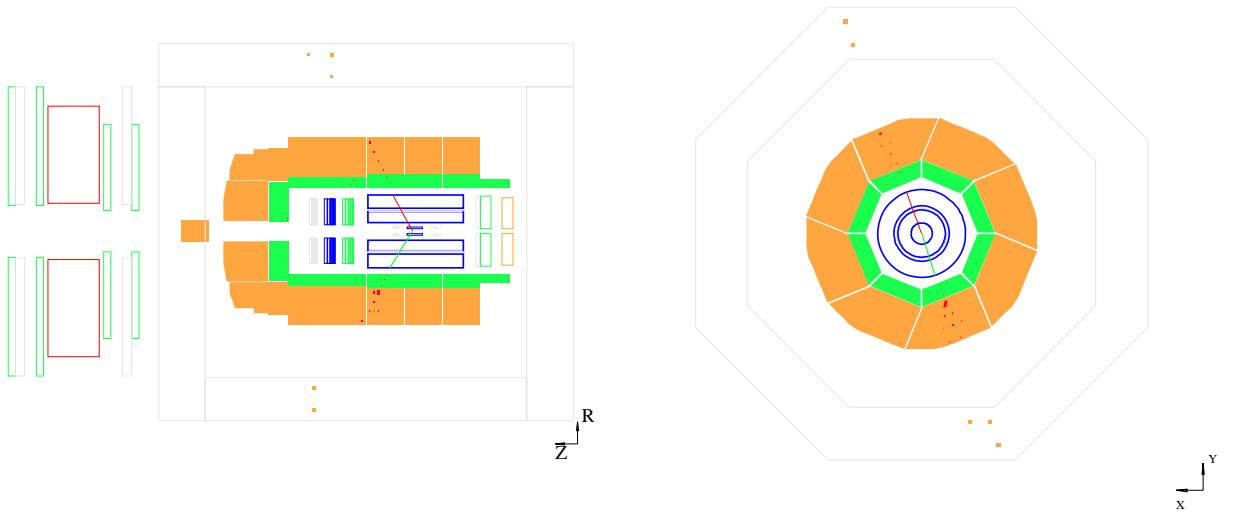


Figure 3: Event display of a di-muon event with an invariant mass $M_{12} = 87.35$ GeV. The transverse momenta of the muons were evaluated at $P_{T_{\mu 1}} = 46.54$ GeV and $P_{T_{\mu 2}} = 40.97$ GeV.

E= -27.6 x 920.0 GeV B=11.6 kG

DSN=/x03/usr/rothmai/mlep2607/scan/3EHera2.dst

RUN 384390 Event 32486

AST (DMIS) = 0 7888 0 0

RST (DMIS) = 0 1078C8 42500001 0

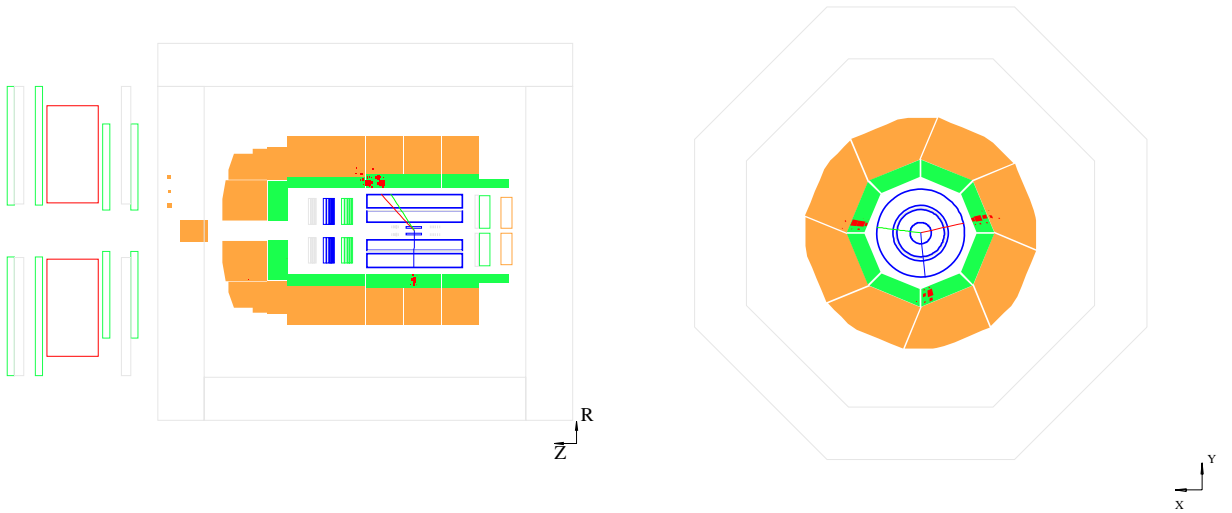


Figure 4: Display of a tri-electron event with an invariant mass ($M_{12} = 136.60$ GeV). Two high- P_T electrons were found in this event. The values were determined to $P_{T_{e1}} = 42.04$ GeV and $P_{T_{e2}} = 39.65$ GeV.

E= -27.6 x 920.0 GeV B=11.6 kG
 DSN=/x03/usr/rothmai/mlep2607/scan/EMuMuHera2.dst
 RUN 373470 Event 48834
 AST (DMIS) = 0 0 0 8C0000
 RST (DMIS) = 0 100000 50500005 8C8000

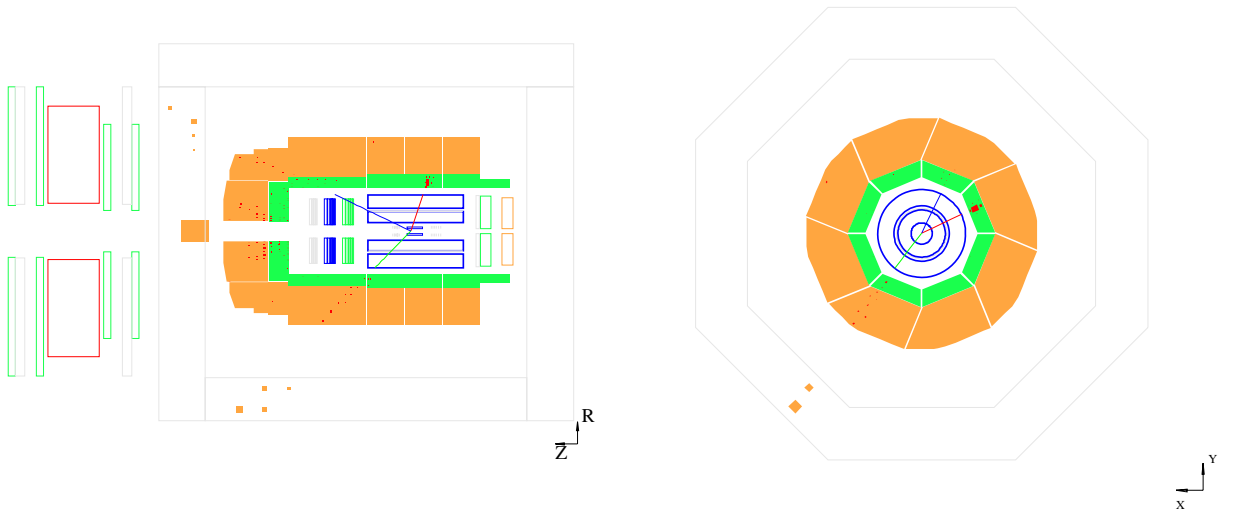


Figure 5: Display of an $e\text{-}\mu\text{-}\mu$ event with an invariant mass ($M_{12} = 83.69$ GeV). The transverse momentum of the muon pair was evaluated at $P_{T\mu_1} = 46.59$ GeV and $P_{T\mu_2} = 34.48$ GeV.

Danksagung – Remerciements

Ich möchte mich an dieser Stelle bei allen bedanken, die zum Zustandekommen dieser Arbeit beigetragen haben.

Zunächst gilt mein Dank Frau Prof. Dr. Beate Naroska, deren Engagement es mir ermöglicht hat, meine Diplomarbeit in der H1-Gruppe in Marseille zu schreiben. Danke auch für die Bereitschaft, die Betreuung von Hamburger Seite aus zu übernehmen.

Herrn Prof. Dr. Joachim Meyer danke ich, dass er sich dazu bereiterklärt hat, als zweiter Gutachter zu fungieren.

Je remercie Dr. Claude Vallée pour l'accueil gentil au sein du groupe H1 au Centre de Physique des Particules de Marseille. Merci pour m'avoir offert ce sujet intéressant de mon stage.

Je remercie également Dr. Franca Cassol-Brunner pour sa bonne humeur et ses diverses aides informatiques.

Je remercie tout particulièrement Dr. Emmanuel Sauvan pour sa constante disponibilité ainsi que pour ses nombreuses corrections et remarques très utiles pendant la préparation de mon rapport.

Je tiens à remercier les thésards du CPPM pour leurs conseils, leur bonne humeur et les rencontres sympathiques à part du travail. Grace à eux, je me suis senté très bien intégré à l'institut.

Je remercie tout particulièrement mon amie Cécile qui m'a aidé à m'installer à Marseille et qui m'a toujours soutenu et encouragé pendant le stage et la rédaction.

Ich danke meinen beiden Englisch-Korrektoren, Stuart Paterson und Heinz Meschede, für ihre große Hilfe.

Ganz besonders danke ich Saskia für ihre Freundschaft und die Unterstützung in den schwierigen Momenten.

Schließlich möchte ich an dieser Stelle meinen Eltern danken, die mein Studium ermöglicht und mich jederzeit in allen Belangen unterstützt haben.

Erklärung

Hiermit versichere ich, dass ich die vorliegende Arbeit selbständig angefertigt und nur die angegebenen Quellen und Hilfsmittel verwendet habe. Die Arbeit wurde noch keiner Prüfungsbehörde in gleicher oder ähnlicher Form vorgelegt.

Florian Rothmaier
Marseille, den 15. Mai 2005